On the Connection Between Particle Physics and Properties of Cosmic Magnetic Fields

Dissertation
zur Erlangung des Doktorgrades
an der Fakultät für Mathematik,
Informmatik und Naturwissenschaften
Fachbereich Physik
der Universität Hamburg

vorgelegt von

Natacha Violante Gomes Leite

Hamburg
2017

Gutachter der Dissertation:
Prof. Dr. Günter Sigl
Prof. Dr. Robi Banerjee

Gutachter der Disputation:
Prof. Dr. Günter Sigl
Prof. Dr. Robi Banerjee
Prof. Dr. Dieter Horns
Dr. Benjamin Bahr
Prof. Dr. Sven-Olaf Moch

Datum der Disputation: 22.05.2017

Vorsitzender des Prüfungsausschusses:
Prof. Dr. Dieter Horns

Vorsitzender des Promotionsausschusses:
Prof. Dr. Wolfgang Hansen

Dekan der Fakultät für Mathematik, Informatik und Naturwissenschaften:
Prof. Dr. Heinrich Graener

No interior das formas imperfeitas
Já nova luz murmura
De sonhos mortos, de ilusões desfeitas,
Há-de nascer uma Verdade pura.

Teixeira de Pascoaes, Gatão 1915

Zusammenfassung

Die vorliegende Dissertation spiegelt die Bedeutung wider, die die Teilchenphysik für das Verständnis der kosmischen Magnetfelder, und umgekehrt, hat, indem sie sich auf Systeme der Astroteilchenphysik konzentriert, bei denen das Zusammenspiel der beiden eine wesentliche Rolle spielt.

Der chirale magnetische Effekt im Kontext der Magnetohydrodynamik wurde sowohl im astrophysikalischen als auch im kosmologischen Zusammenhang untersucht. Dabei wurde gefunden, dass dieser Effekt zu maximal helischen Feldern und zur Verstärkung der Keimzellen des Magnetfelds im Kern von Proto-Neutronensternen führt, was, abhängig von der Temperatur und den Dichteschwankungen des Kerns, in einer Feldstärke von bis zu 10^{14} G auf kleinen Längen- und Zeitskalen resultiert. Es ist somit unwahrscheinlich, dass bei einem Proto-Neutronenstern, der sich zu einem Magnetar weiterentwickelt, die chirale magnetische Instabilität der Ursprung der auf dessen Oberfläche beobachteten Magnetfelder ist. Ferner stellte sich heraus, dass der chirale magnetische Effekt im frühen Universum, ungefähr zur Zeit der elektroschwachen Symmetriebrechung, magnetische Helizität bei anfänglich nicht-helischen Feldern erzeugt und zu einer Verlangsamung des resistiven Zerfalls des kosmologischen Magnetfelds führt.

Die aus den ersten Supernovae stammende kosmische Strahlung könnte eine entscheidende Rolle während der Epoche der Reionisation gespielt haben, indem sie im intergalaktischen Medium und dem entsprechenden Magnetfeld diffundiert ist. Die Analyse der Details dieser Epoche sowie der Ausbreitung und der Energieverluste kosmischer Strahlung ergab, dass kosmische Strahlung mit einer Energie von $\lesssim 10$ MeV die Temperatur des neutralen intergalaktischen Mediums bei einer Rotverschiebung von $z = 10$, je nach Injektionsspektrum der kosmischen Strahlung, um 10-200 K erhöht. Es ist zu erwarten, dass diese Aufheizung des Mediums durch Beobachtungen der 21-cm-Spektrallinie des neutralen Wasserstoffs detektiert wird, während dessen räumliche Verteilung Details der Struktur und Stärke der frühen intergalaktischen Magnetfelder aufdecken kann.

Die Emission von Synchrotronstrahlung ist eine der Methoden, durch welche Überreste der Dunklen Materie uns erreichen können. Die Emission von Radiostrahlung, die von der Annihilation Dunkler Materie zu $e^{\pm}$ aus einer subgalaktischen Hochgeschwindigkeitswolke, der Smith-Wolke, herrührt, wurde benutzt, um den Annihilationswirkungsquerschnitt der WIMP-Dunklen Materie einzugrenzen. Es ergab sich, dass der Fluss der Radiostrahlung weitgehend unabhängig von den Details der Ausbreitung ist und dass niedrige Frequenzen besser für Radiosuchen geeignet sind. Die so erhaltenen Grenzen, die sich sowohl aus vorhandenen als auch aus projizierten Daten unter Annahme der Kontrolle der astrophysikalschen Hintergrundsubtraktion ergeben, konkurrieren mit den Grenzen, die mithilfe von Methoden wie der Gamma-Strahlung aufgestellt wurden, und zeigen, dass durch die Verwendung von Daten von Radioteleskopen der nächsten Generation durchaus relevante Einschränkungen des Annihilationswirkungsquerschnitts Dunkler Materie gefunden werden können.

Abstract

This dissertation reflects the significance of particle physics to the problem of understanding magnetic fields in the cosmos, and vice versa, by focusing on astroparticle systems where the interrelatedness of both plays a major role.

The chiral magnetic effect in the context of magnetohydrodynamics was investigated both in an astrophysical and in a cosmological setting. This effect was found to lead to maximally helical fields and to seed magnetic field amplification in the core of protoneutron stars, contributing to reach up to 10^{14} G at small length and time scales, depending on the temperature and density fluctuations of the core. It is, therefore, unlikely that for a protoneutron star that evolves into a magnetar the chiral magnetic instability is at the root of the magnetic fields observed at its surface. In the early Universe, around the electroweak symmetry breaking, the chiral magnetic effect was found to generate magnetic helicity from initially non-helical fields and to lead to a slowing down of the cosmological magnetic field resistive decay.

Cosmic rays originated in the first supernovae might have played a crucial role at the epoch of reionization by diffusing in the intergalactic medium and in the corresponding magnetic field. Analysing the details of this epoch together with the propagation and energy losses of cosmic rays, it is concluded that cosmic rays of energy $\lesssim 10$ MeV increase the neutral intergalactic medium temperature by 10-200 K at redshift $z = 10$, depending on the cosmic ray injection spectrum. This heating up of the medium is expected to be detected by neutral hydrogen 21 cm observations and its spatial distribution can reveal details of the structure and strength of early intergalatic magnetic fields.

Synchrotron emission is one of the methods through which vestiges of dark matter could reach us. The radio emission associated with dark matter annihilations into $e^{\pm}$ from a sub-galactic high velocity cloud, the Smith Cloud, was used to constrain the annihilation cross-section of WIMP dark matter. It is concluded that the radio flux is quite independent from the propagation details and that low frequencies are better suited for radio searches. The constraints drawn, both with available and with projected data that assume the control over astrophysical background subtraction, compete with those posed using techniques such as gamma rays, and show that quite relevant limits to the dark matter annihilation cross-section can be inferred with data from the next generation of radiotelescopes.

List of Publications

This thesis is based on the following publications:

[1] Günter Sigl and Natacha Leite, *Chiral Magnetic Effect in Protoneutron Stars and Magnetic Field Spectral Evolution*, JCAP 1601 (2016) no.01, 025, `[arXiv:1507.04983]`

[2] Petar Pavlović, Natacha Leite, Günter Sigl, *Modified Magnetohydrodynamics Around the Electroweak Transition*, JCAP 1606 (2016) no.06, 044, `[arXiv:1602.08419]`

[3] Natacha Leite, Robin Reuben, Günter Sigl, Michel H. G. Tytgat, Martin Vollmann, *Synchrotron Emission from Dark Matter in Galactic Subhalos. A Look into the Smith Cloud*, JCAP 1611 (2016) no.11, 021, `[arXiv:1606.03515]`

[4] Natacha Leite, Carmelo Evoli, Marta D'Angelo, Benedetta Ciardi, Günter Sigl, Andrea Ferrara, *Do cosmic rays heat the early intergalactic medium?*, MNRAS (2017) 469 (1): 416-424, `[arXiv:1703.09337]`.

Contents

Chapter 1

Introduction

The Universality of physical laws has shown time and again that very different and apparently disconnected phenomena are connected through wondrous correspondences. That is the essence that underlies this work in Astroparticle Physics. This dissertation aspires to study the interdependence of cosmic magnetic fields and their properties with aspects from particle physics. The connection between both is a subject which is broad in realizations and challenging in concretizations. This allows for a rich exploration of topics in Astroparticle Physics, which is already in itself a field that bridges two other – astrophysics and particle physics [5, 6].

As one of Nature's interactions, electromagnetism manifests itself all around us, both in daily life and at the largest scales of the cosmos. When contemplating the history of our Universe, magnetic fields occupy a more important place than electric fields since the high conductivities characteristic of the early Universe would cause electric fields to decay fastly, while magnetic fields would survive much longer. A common feature to many topics in Astroparticle Physics is the need for a deeper understanding and more detailed information on magnetic fields in order to make further significant advancements. Magnetic fields appear to be present at almost all scales of the observable Universe [7, 8]. Their role is pivotal for the study of several cosmological and astrophysical aspects, such as Large Scale Structure formation and development, or the propagation of charged particles throughout our Galaxy [9]. Due to the interplay between magnetic fields and the matter content of the Universe, questions that have been proving difficult to be answered can be looked at from different perspectives. This may reveal new insights, for example to baryogenesis or to the physics of compact stars, which are highly magnetized objects.

At the galactic and larger scales, by means of optical and synchrotron polarization [10], Zeeman splitting [11] and Faraday rotation measures [12], magnetic fields are loosely constrained because of the difficulty of measuring them. These techniques do not simultaneously provide much information on the three dimensional structure and strength of fields. Our current knowledge points to galaxies and galactic cluster magnetic fields with strengths of the order of 10^{-6} Gauss [13, 14]. It is not even certain that extragalactic magnetic fields do exist, but some lower limits were placed at 10^{-16} G [15]. At the astrophysical scale, although having much better measurements – and of much higher orders, such as magnetars with 10^{15} G [16] – our understanding is far from being complete. The challenge is certainly not only observational, since the theoretical question of the origin of magnetic fields is as much central as it is unsettled [17]. Without a solid understanding of magnetogenesis our knowledge is limited on the evolution of magnetic fields and on the characteristics that we expect them to display in different contexts [18, 19].

The evidences that magnetic fields are present, from planetary and solar environments to galaxy clusters, make it straightforward to assume that they were already present in the early Universe. This line of thought perceives magnetic fields as having a cosmological origin. Such magnetogenesis mechanisms are usually placed early in the evolution of the Universe and at some disruptive time. This may happen when turbulent conditions for the production of magnetic fields are met [20]. For example, such as at inflation [21–23] or at a hypothetical first order phase transition before the electroweak one, especially after knowing that the electroweak symmetry breaking is likely to be a crossover transition in the Standard Model. They would produce strong magnetic fields whose strength would decay as the Universe expands and cools down. Another viewpoint is to consider that magnetic fields have an astrophysical origin. In this case magnetic fields are thought to have been created by charge separation during galaxy formation. The seed fields produced in this way would be rather weak and later amplified via flux conservation in gravitational collapse and by various types of dynamo effects [24].

By studying different settings where magnetic fields are present, this work aims at showing the potential that lies in comprehending the interconnection between them and the particle content of the Universe. The study of magnetic fields in a plasma, as is the case of several astrophysical and cosmological systems, is given more appropriately by a magnetohydrodynamical description. A particularly good example where the particle content significantly changes conventional magnetohydrodynamics is given by taking into account the effects of the chiral anomaly. This hypothesis will be presented and analysed in Chapter 2. The chiral magnetic effect, based on the non-vanishing current induced in a system that counts with an asymmetry between the number of particles with different chirality states, shows that particle physics is inextricable from magnetic helicity. An astrophysical setting where a chiral imbalance naturally arises occurs, for example, in supernovae core collapse. These are thought to be the origin of the highest magnetized objects in the Universe. Can this effect be responsible for the surface field strengths of magnetars? By simulating the conditions appropriate to the system, it becomes evident that the chiral asymmetry will result in a significant enhancement of the magnetic field right after core collapse for hot protoneutron stars, which is the focus of this study. An equally interesting system to investigate this effect is the early Universe, more specifically at the electroweak symmetry breaking. This marks the transition at which particles gain mass and electromagnetism decouples from the weak interaction. In which way do the changes brought by this transition affect the evolution of cosmological magnetic fields in the early Universe through the chiral anomaly? Obtaining the magnetic spectral evolution, along with the evolution of the chiral asymmetry in each context, allows these questions to be answered and their consequences to be discussed.

From the electroweak symmetry breaking, we turn our attention to another cosmological transition of high importance that takes place at a much later time, namely, reionization. It is well known that studying particle physics, for example by analysing the particles that reach us from the cosmos, i.e. cosmic rays, one can probe the environment they traversed, and therefore, the magnetic field they were subject to if charged. In the epoch of formation of first galaxies, when the Universe got reionized, our interest will be to study cosmological cosmic rays. Their role in reionization itself is minimal, as the major factor for it is stellar radiation. However, primordial cosmic rays might efficiently lose energy as they diffuse in the magnetic field of the intergalactic medium and could contribute to increase the temperature of the medium prior to reionization being complete. Chapter 3 is intended to evaluate the impact of the contribution of high-redshift cosmic rays to the heating of the medium. It is important to understand the implications of this heating mechanism, since it has been neglected so far. Specifically because the temperature of the intergalactic neutral regions will soon become experimentally available to us by measurements of the 21-cm line signal from neutral Hydrogen. The morphology of this signal, i.e., whether the temperature increment is found to be uniformly distributed or clustered around the haloes that originated and accelerated cosmic rays, highly depends on the structure and strength of the magnetic field in the regions through which cosmic rays propagated at those times.

In addition, the 21-cm line signal from neutral Hydrogen has detected sub-galactic structures, such as high velocity clouds, e.g. the Smith Cloud. A common way to explain the survival of the Smith Cloud through the galactic plane is by assuming that it is embedded in a dark matter halo. In this setting, magnetic fields can play the role of messengers of new physics through enabling synchrotron radiation to carry evidences of dark matter annihilation, or their lack of, whose signal upcoming radio experiments can detect. Chapter 4 is dedicated to draw relevant constraints on the dark matter annihilation cross-section using synchrotron radiation. This method, albeit having received less attention than gamma-ray searches, will be shown to be equally powerful and complementary in indirect dark matter detection.

After these topics have been analysed, the unifying role that magnetic fields have in Astroparticle physics will become even clearer. Chapter 5 summarizes the most important results that, in collaboration with different authors, lead to the published material of Refs. [1–4]. These results were reached as a consequence of studying the relationship between particles in astrophysics and cosmology with magnetic fields in different frameworks. In the same way that solid models of the origin and evolution of magnetic fields can greatly contribute to apparently distinct astroparticle physics topics, dedicated astroparticle measurements can serve to infer the strength and structure of fields. Such is the case in anomalous magnetohydrodynamics, dark matter indirect searches and the reionization of the Universe.

Chapter 2

The Chiral Magnetic Effect in Magnetohydrodynamics

When in the XX century quantum mechanics began replacing our understanding of the microscopic world leading to the flourishing of quantum field theory, several effects, which stemmed from the quantum nature of operators and observables that aimed at describing physical reality, became apparent. The quantum formulation of our theories oughted to be renormalizable (by absorbing the ultraviolet divergences found in perturbative quantum field theory in the redefinition of physical quantities) and 't Hooft and Veltman proved that any gauge theory with massless gauge bosons is renormalizable [25] and, therefore, renormalizable theories must conserve gauge currents, just as currents are classically conserved.

It was in 1969 that Adler [26] and, independently, Bell and Jackiw [27] emphasized that the presence of closed-loop triangle diagrams cause the axial-vector vertex in spinor electrodynamics to behave in a manner unexpected by field theory: in perturbation theory the divergence of the axial-vector current does not vanish even after renormalization (which is possible since contributions by fermions to triangle diagrams cancel out as a whole). This divergence contained a well-defined extra term that was absent in computations from the equations of motion, which was therefore called anomalous. Since the left- and right-handed chiral currents will also not be conserved, the axial-vector anomaly, or Adler-Bell-Jackiw anomaly, is also called chiral anomaly.

The study of the triangle anomaly led to the discovery of surprising effects that motivated research in several different fields, shortly overviewed here to provide a taste of its large range of possible applications and to motivate the interest in the chiral magnetic effect – i.e. in the anomaly in the presence of electromagnetic fields – in particular.

Quantum chromodynamics (QCD) is a theory that presents spontaneous breaking of chiral symmetry. Strongly interacting matter under intense electromagnetic fields has been a rich field of research [28], which can be divided in the study of equilibrium phenomena and anomaly-induced transport phenomena [29]. In a quark-gluon or relativistic electromagnetic plasma, an asymmetry between left- and right-handed fermions results in adding to the kinetic theory Berry curvature corrections [30], which leads to the arising of a plasma instability – the chiral plasma instability [31]. Even when there is no asymmetry present, the chiral anomaly results in the induction of an axial current in relativistic plasmas with nonzero magnetic field and nonzero electrical chemical potential, causing electric charge separation along the magnetic field – the chiral separation effect [32, 33]. While previously relying on lattice simulations, presently we have also access to the first experimental confirmations of these theoretically predicted phenomena by relativistic heavy ion collision (at nonzero impact parameter), which provides us with a QCD plasma in a very intense magnetic field ($B \sim 10^{18}$ G) [34]. These chiral effects are being probed by the STAR collaboration[1] and by ALICE at the Large Hadron Collider. [2]

In condensed matter physics, triangle anomalies can be realized in Weyl semi-metals [35–37].

The standard Glashow-Salam-Weinberg electroweak theory is chiral, therefore also including the anomaly, which has been vigorously studied mainly due to it providing baryonic charge violation, a valuable ingredient for electroweak baryogenesis theories [38, 39]. The interplay between magnetic fields and the chiral anomaly in the early Universe [40–42], where one can consider that an asymmetry between left- and right-handed particles can arise from out-of-equilibrium parity-violating decays of massive particles, allowed for hypotheses on the origin [43] and evolution of cosmological magnetic fields [44] related to the chiral magnetic and vortical effects. The anomaly was studied as possibly having a role in the amplification of seed magnetic fields strong enough to account for the present galactic magnetic field [45], as well as being linked to baryogenesis scenarios [46, 47].

In astrophysics, since the end of the seventies that it is known that a rotating black hole has an induced current along the axis of rotation due to the coupling between the fermion's spin and angular momentum when these fermions are left-handed [48], as in the case of standard model neutrinos. A more recently proposed environment suitable for the study of chiral effects is the core collapse of supernovae, which will be further elaborated in §2.2. This is mainly motivated by observational properties that do not find a straightforward theoretical explanation, such as neutron star kicks, precession and magnetic fields (see, e.g. Refs. [49, 50]).

This chapter is dedicated first to introduce the chiral anomaly and the chiral magnetic effect, which will be discussed in §2.1 (for a historical account, the reader is directed to Ref. [51]). This anomalous effect is of interest to magnetohydrodynamics (MHD) since the nonconserved axial-vector current is going to modify Maxwell's equations and, con-

---

[1] `http://www.star.bnl.gov`

[2] `http://aliceinfo.cern.ch`

sequently, the evolution of electromagnetic fields. This is one of the realizations that connect magnetic fields in the Universe to particle physics and this chapter specifically focuses on two relevant systems where the chiral magnetic effect might dictate the MHD evolution. First, in §2.2, the amplification of magnetic energy in the interior of a neutron star is analysed, following Ref. [1]. Subsequently, in §2.3, the consequences of the chiral magnetic effect on the electroweak transition is studied, based on Ref. [2]. This chapter uses Lorentz-Heaviside units.

2.1 Chiral Anomaly

Chiros is the Greek word for *hand*, thus, chirality derives its name from being etymologically linked to handedness, since it describes an asymmetry property shown by objects whose mirror image does not coincide with themselves, similar to the property that makes a right and a left hand distinguishable. In the context of particle physics, it represents a quantum property associated with the matrix γ_5, which can be defined as $\gamma_5 = i\gamma^0\gamma^1\gamma^2\gamma^3$ and the remaining arbitrary overall factor can be chosen in a way that $\gamma_5^\dagger = \gamma_5$ and $(\gamma_5)^2 = 1$ are satisfied. This guarantees that the matrices

$$L = \frac{1-\gamma_5}{2},\ R = \frac{1+\gamma_5}{2} \tag{2.1}$$

can be used as fermion fields and spinors projection matrices such that an object that satisfies the Dirac equation can be divided into a left- and right-handed part, respectively. One of the main properties of γ_5 is that it anticommutes with all Dirac matrices. Note that chiral projections are invariant under Lorentz transformations (i.e. $[\gamma_5, \sigma_{\mu\nu}] = 0$, with $\sigma_{\mu\nu} = i/2[\gamma_\mu, \gamma_\nu]$). Another important property that will have major consequences throughout this work is the fact that the chirality of a free particle is not conserved, because γ_5 and the mass term in the Dirac Hamiltonian, $H = \gamma^0(\gamma^i p^i + m)$, with p the momentum of the particle and m its mass, do not commute – they rather anticommute. This means that a left-chiral particle at one time may change its chirality when scattering on a massive particle: a chirality flip occurs.

A concept closely related to chirality is that of helicity, which for a fermion has to do with the relative orientation of its spin, $\mathbf{\Sigma}/2$, and momentum

$$h_{\mathbf{p}} = \frac{\mathbf{\Sigma}\cdot\mathbf{p}}{p}\,. \tag{2.2}$$

When the helicity eigenvalue is $+1$, the spin and angular momentum of the fermion are in the same direction and its helicity eigenstate is called right-handed. The same fermion viewed by an observer that travels along the same direction but faster than the particle with respect to the original frame will be perceived to move in the opposite direction. Since the particle's spin does not change, the result is that in the frame of this observer, the same fermion will be left-handed. Thus, for massive fermions, helicity is not a Lorentz invariant. Additionally, since $h_{\mathbf{p}}$ commutes with the Dirac Hamiltonian, momentum conservation implies that helicity has to be conserved with time for a free particle. From this one sees that, while helicity and chirality appear to have opposite characters, in the massless limit they unite. In the remainder of this work handedness is meant in the chiral framework, unless stated otherwise.

The chiral anomaly appears in gauge theories with chiral fermions and we shall now see why.[3] The Lagrangian density in quantum electrodynamics (QED) reads

$$\begin{aligned}\mathcal{L} &= \bar{\psi}(i\gamma^\mu\partial_\mu - e\gamma^\mu A_\mu - m)\psi & (2.3)\\ &= \bar{\psi}_L(i\gamma^\mu\partial_\mu - e\gamma^\mu A_\mu - m)\psi_L + \bar{\psi}_R(i\gamma^\mu\partial_\mu - e\gamma^\mu A_\mu - m)\psi_R \\ &\quad -m\bar{\psi}_L\psi_R - m\bar{\psi}_R\psi_L\,, & (2.4)\end{aligned}$$

with $\bar{\psi} = \psi^\dagger\gamma^0$, e the charge and A_μ the electromagnetic gauge potential. In the limit $m \to 0$, the Lagrangian presents the two following global symmetries: it remains invariant under vector transformations $\psi \to e^{i\lambda}\psi$, with constant λ (left- and right-handed fields transform in the same way) and under chiral transformations $\psi \to e^{i\lambda\gamma_5}\psi$, since $[\gamma_5, \gamma^0\gamma^\mu] = 0$ (fields transform with opposite charge). Let us recall that Noether's theorem guarantees that to a Lagragian invariance corresponds a current conservation [54]. The Noether currents associated to these symmetries are the vector current $j_\mu = \bar{\psi}\gamma^\mu\psi$ and the axial-vector current

$$j_5^\mu = \bar{\psi}\gamma^\mu\gamma_5\psi \equiv j_L^\mu - j_R^\mu\,. \tag{2.5}$$

In the presence of a background electromagnetic field, the classically conserved Noether currents, derived from the equations of motion, cannot be simultaneously conserved after quantization. The requirement that renormalized quantities respect local gauge invariance is expressed in the form of the Ward identities for Green's functions. For Abelian QED, this is realized in the Ward-Takahashi identities [55,56], while for non-Abelian theories, the Becchi-Rouet-Stora identities can be used [57]. The γ_5 couplings to gauge field imply axial-vector and vector Ward identities, but the issue is that there are Feynman diagrams in one-loop order of perturbation theory which violate axial Ward identities, namely triangle, box and pentagon diagrams with overall abnormal parity (i.e. with an odd number of γ_5 couplings to the gauge field). The AVV triangle diagram, with one axial-vector and two vector vertices, is of special interest since it is proven that if it cancels out, so do the other diagrams [58]. It was also proven that radiative corrections do not renormalize the anomaly [59]. One manages to eliminate closed fermion loop contributions through shifting the loop integration variable. While this represents no issue for convergent Feynman diagrams, such as the AAA loop, the AVV diagram diverges linearly. Although the linear divergence

---

[3] Explicit diagrams and computations are omitted for the sake of brevity, but the reader is directed to §3.3 of Ref. [52] or to Ref. [53] for more comprehensive details.

vanishes under symmetric integration, there is a remaining finite residue spoiling either the conservation of the vector current or the axial-vector current. The price of keeping a vanishing vector current divergence, $\partial_\mu j^\mu = 0$ – certainly desirable in order to mantain gauge invariance – is paid by an irreducible extra-term appearing in the axial current divergence, which to order e^2 results in [26, 27]

$$\partial_\mu j_5^\mu = 2imj_5 + \frac{e^2}{16\pi^2}\epsilon^{\mu\nu\rho\sigma}F_{\mu\nu}F_{\rho\sigma}\,, \tag{2.6}$$

where $F_{\mu\nu} = \partial_\mu A_\nu - \partial_\nu A_\mu$ is the field strength tensor corresponding to the gauge field A_μ. The second term in (2.6) is the Abelian axial-vector anomaly (or simply axial anomaly). The left- and right-handed chiral currents $j_\mu \pm j_\mu^5$ will also not be conserved due to the axial anomaly, being therefore also known as chiral anomaly. This shows us that the gauge invariance of QED theory inevitably causes the violation of the axial U(1) symmetry. The anomaly in triangle diagrams is known since the beginning of the fifties [60, 61], but what motivated it to receive some attention was the paradox of Sutherland: applying the current algebra and partial conservation of axial-vector current to the pion decay into photons gave a rate much smaller than what was found in experiment. Adler [26], and Bell and Jackiw [27], solved this paradox by taking the triangle anomaly into account, thus also known as Adler-Bell-Jackiw anomaly.

There is an alternative way to phrase the conservation law that was expected to involve j_μ^5. We can rearrange the anomalous term such that

$$\begin{aligned}\partial_\mu j_5^\mu &= \frac{e^2}{16\pi^2}\epsilon^{\mu\nu\rho\sigma}(\partial_\mu A_\nu - \partial_\nu A_\mu)(\partial_\rho A_\sigma - \partial_\sigma A_\rho) &(2.7)\\ &= \frac{4e^2}{16\pi^2}\epsilon^{\mu\nu\rho\sigma}\partial_\mu A_\nu \partial_\rho A_\sigma = \frac{e^2}{4\pi^2}\epsilon^{\mu\nu\rho\sigma}\partial_\mu(A_\nu\partial_\rho A_\sigma)\,, &(2.8)\end{aligned}$$

in the massless limit. Thus, by defining

$$K^\mu = \frac{e^2}{4\pi^2}\epsilon^{\mu\nu\rho\sigma}A_\nu\partial_\rho A_\sigma\,, \tag{2.9}$$

which corresponds in fact to the topological Chern-Simons current [62], the axial-vector current still takes part in a conservation law, viz.

$$\partial_\mu(j_5^\mu - K^\mu) = 0\,. \tag{2.10}$$

Defining the chiral fermion number as $N_5 \equiv \int d^3x\,\bar\psi\gamma_5\psi$ and the topological Chern-Simons number as $N_{CS} \equiv \int d^3x K^0$ [63], space integration renders this conservation law in the form

$$\frac{d}{dt}\left(N_5 - N_{CS}\right) = 0\,. \tag{2.11}$$

Therefore, one of the consequences derived from the presence of axial-vector triangle diagrams is that in massless electrodynamics the axial current associated with the transformation of γ_5 is not conserved, even though the Lagrangian is invariant with respect to it.

Magnetic Helicity

Magnetic helicity, using Gauss's linking formula, expresses the linkage of the flux of magnetic field. As a volume integral, it can be defined as [64, 65]

$$\mathcal{H} = \int d^3x \, (\mathbf{B} \cdot \mathbf{A}) \, , \tag{2.12}$$

where $\mathbf{A}$ is the vector potential of the magnetic field $\mathbf{B} = \nabla \times \mathbf{A}$. This definition implies that no magnetic field lines cross the boundary of the volume, a condition usually assumed in order for (2.12) to be gauge invariant.

The key to the chiral magnetic effect lies in the fact that the conservation law just derived in (2.11) connects the chiral asymmetry to the magnetic helicity through the Chern-Simons number of the electromagnetic field

$$\frac{d}{dt}\mathcal{H} = -2 \int d^3x \, (\mathbf{E} \cdot \mathbf{B}) = \frac{1}{2} \int d^3x \, F_{\mu\nu} \tilde{F}^{\mu\nu} \, , \tag{2.13}$$

with $\mathbf{E}$ the electric field and $\tilde{F}^{\mu\nu} = \epsilon^{\mu\nu\rho\sigma} F_{\rho\sigma}/2$. Eq. (2.11) can then be written as

$$\frac{d}{dt} \left(N_5 - \frac{e^2}{4\pi^2} \mathcal{H} \right) = 0 \, . \tag{2.14}$$

The chiral magnetic chemical potential is then introduced to treat systems with non-vanishing chirality [66]

$$\mu_5 \equiv \frac{\mu_L - \mu_R}{2} \, , \tag{2.15}$$

where $\mu_{L/R}$ represents the chemical potential of left/right-handed particles. When a magnetic field is introduced, the rotational invariance of a system is broken and spins gain a preferred orientation. This causes particles to align or anti-align with the magnetic field depending on their chirality state. That induces a current along the axis of the magnetic field, which can be computed from the expectation value of the vector current operator (see Refs. [28, 29]). Only the Landau zero-mode contributes to the current.

The equilibrium current density for non-interacting massless left-handed fermions of charge e, in an external magnetic field, was found by Vilenkin [67] to be $\mathbf{j} = -e^2 \mu \mathbf{B}/(2\pi^2)$, a result that depends only on the chemical potential and not on the temperature of the particles. Note that for a system of interacting massive particles it was found that the current is vanishing [67].

The anomalous current density introduced in (2.5), in vectorial form yields then

$$\mathbf{J_5} = -\frac{g^2}{2\pi^2} \mu_5 \mathbf{B} \, , \tag{2.16}$$

where g is the coupling constant of the system under study. This implies that, if there is a magnetic field, in the presence of a chiral asymmetry, an additional current proportional to this asymmetry is generated – the chiral magnetic effect (CME) [66] – at the same time that its evolution is linked to magnetic helicity.

Anomalous Magnetohydrodynamics

A non-vanishing anomalous current (2.16) implies that Maxwell's equations will have an additional contribution to the Ohmic electric current: $\mathbf{J}_{\rm tot} = \sigma(\mathbf{E} + \mathbf{v} \times \mathbf{B}) + \mathbf{J_5}$, where σ is the electrical conductivity and $\mathbf{v}$ is the fluid velocity. The magnetohydrodynamic equations will then be modified as follows:

Ampère's law, neglecting the displacement current, reads

$$\nabla \times \mathbf{B} = \sigma(\mathbf{E} + \mathbf{v} \times \mathbf{B}) - \frac{g^2}{2\pi^2}\mu_5 \mathbf{B}\,. \tag{2.17}$$

Faraday's law, given by the curl of $\mathbf{E}$, is

$$\partial_t \mathbf{B} = \nabla \times (\mathbf{v} \times \mathbf{B}) + \eta \nabla^2 \mathbf{B} - \eta \frac{g^2}{2\pi^2}\mu_5 (\nabla \times \mathbf{B})\,, \tag{2.18}$$

where $\eta = \sigma^{-1}$ is the resistivity.
The Navier-Stokes equation is

$$\rho\left[\partial_t \mathbf{v} + (\mathbf{v}\cdot\nabla)\mathbf{v} - \nu\nabla^2\mathbf{v}\right] = -\nabla p + \sigma[\mathbf{E}\times\mathbf{B} + (\mathbf{v}\times\mathbf{B})\times\mathbf{B}]\,, \tag{2.19}$$

where ρ the energy density, ν is the kinematic viscosity and p is the thermal pressure of the fluid.
The continuity equation is

$$\partial_t \rho + \nabla(\rho \cdot \mathbf{v}) = 0\,, \tag{2.20}$$

and the velocity field evolution is

$$\partial_t \mathbf{v} + \mathbf{v}\cdot\nabla\mathbf{v} + \nabla p - \nu\nabla^2\mathbf{v} = \mathbf{J}\times\mathbf{B}\,. \tag{2.21}$$

As in ideal MHD, this approximation of Maxwell's equations assumes high conductivity, $\nabla \cdot \mathbf{J} = 0$, and the global neutrality of the plasma, $\nabla \cdot \mathbf{E} = 0$.

Due to its simplifying power, we proceed by expressing our formalism in Fourier space. The magnetic field

$$\mathbf{B}(\mathbf{x}, t) = \int \frac{d^3\mathbf{k}}{(2\pi)^{3/2}} e^{i\mathbf{k}\cdot\mathbf{x}} \mathbf{B}(\mathbf{k}, t) \tag{2.22}$$

relates to the gauge potential, assuming the Coulomb gauge ($\nabla \cdot \mathbf{A} = 0$), via $\mathbf{B}(\mathbf{k}) = i\mathbf{k} \times \mathbf{A}(\mathbf{k})$. In Fourier space, (2.18) can then be written as [68]

$$\partial_t \mathbf{B_k} = -\eta k^2 \mathbf{B_k} - \eta\frac{g^2}{2\pi^2}\mu_5 (i\mathbf{k}\times\mathbf{B_k}) + \frac{i}{(2\pi)^{3/2}}\mathbf{k}\times\int d^3q\,\mathbf{v_{k-q}}\times\mathbf{B_q}\,, \tag{2.23}$$

where $\mathbf{B_k} \equiv \mathbf{B}(\mathbf{k}, t)$ and $\mathbf{v_{k-q}} \equiv \mathbf{v}(\mathbf{k}-\mathbf{q}, t)$. In the frame of rest of the plasma the last term vanishes, i.e. there is no contribution from the velocity field. This will be assumed throughout the remainder of this chapter and the validity of this assumption is discussed in §2.4. For a general treatment of anomalous magnetohydrodynamics in the presence of non-vanishing turbulence, the reader is directed to Ref. [68].

The two-point correlator of the magnetic field in Fourier space can be divided in a symmetric, $S(k,t)$, and antisymmetric part, $AS(k,t)$ [69]

$$\langle B_i(\mathbf{k},t)B_j(\mathbf{k}',t)\rangle = \frac{(2\pi)^3}{2}\delta(\mathbf{k}+\mathbf{k}')\left[(\delta_{ij}-\hat{k}_i\hat{k}_j)S(k,t)+i\epsilon_{ijk}\hat{k}AS(k,t)\right]. \tag{2.24}$$

These relate to the magnetic energy and helicity densities, averaged over the system's volume V, via

$$\begin{aligned}\rho_m &= \frac{1}{2V}\int d^3x\langle\mathbf{B}^2\rangle = \int dk\frac{k^2}{2}S(k,t)\\ h &= \frac{1}{V}\int d^3x\langle\mathbf{A}\cdot\mathbf{B}\rangle = \int dkkAS(k,t)\,,\end{aligned} \tag{2.25}$$

respectively. This evidences the relation of the magnetic helicity with the difference in the power spectra between left- and right-handed magnetic fields. To trace the evolution in time of the magnetic field, it is useful to define the spectral magnetic energy and helicity densities, from the last equality of (2.25), as $\rho_k \equiv k^2S(k,t)/2$ and $h_k \equiv kAS(k,t)$, respectively. The evolution of the magnetic energy density can be obtained in terms of the spectral magnetic energy density through

$$\partial_t\rho_k = \frac{1}{2}[\partial_t(\mathbf{B_k}\cdot\mathbf{B_k}^*)] = \frac{1}{2}(\partial_t\mathbf{B_k}\cdot\mathbf{B_k}^*+\partial_t\mathbf{B_k}^*\cdot\mathbf{B_k})\,. \tag{2.26}$$

Using (2.23), it yields

$$\begin{aligned}\partial_t\rho_k &= \frac{1}{2}\Big\{-2\eta k^2\mathbf{B_k}\cdot\mathbf{B_k}^*\\ &\quad -\eta\frac{g^2}{2\pi^2}\mu_5[i\mathbf{k}\times(i\mathbf{k}\times\mathbf{A_k})\cdot\mathbf{B_k}^*+(-i\mathbf{k}\times\mathbf{B_k}^*)\cdot(i\mathbf{k}\times\mathbf{A_k})]\Big\} \qquad (2.27)\\ &= \frac{1}{2}\left[-2\eta k^2|\mathbf{B_k}|^2-\eta\frac{g^2}{2\pi^2}\mu_5(2k^2\mathbf{A_k}\cdot\mathbf{B_k}^*)\right]. \qquad (2.28)\end{aligned}$$

In the same way, the magnetic helicity density evolution can be calculated from $\partial_t(\mathbf{A_k}\cdot\mathbf{B_k}^*) = \partial_t\mathbf{A_k}\cdot\mathbf{B_k}^*+\partial_t\mathbf{B_k}^*\cdot\mathbf{A_k}$, using (2.23), and the fact that

$$\partial_t\mathbf{A_k} = \partial_t\left(\frac{i\mathbf{k}}{k^2}\times\mathbf{B_k}\right) = -\eta k^2\mathbf{A_k}-\eta\frac{g^2}{2\pi^2}\mu_5\mathbf{B_k}\,, \tag{2.29}$$

which results in

$$\partial_t h_k = -2\eta k^2\mathbf{A_k}\cdot\mathbf{B_k}^*-\eta\frac{g^2}{2\pi^2}\mu_5\left[\mathbf{B_k}\cdot\mathbf{B_k}^*-(i\mathbf{k}\times\mathbf{B_k}^*)\left(\frac{i\mathbf{k}}{k^2}\times\mathbf{B_k}^*\right)\right]. \tag{2.30}$$

From (2.28) and (2.30), the time evolution of the spectral densities then follow

$$\begin{aligned}\partial_t\rho_k &= -2\eta k^2\rho_k-\eta\frac{g^2}{2\pi^2}\mu_5k^2h_k\,, \qquad (2.31)\\ \partial_t h_k &= -2\eta k^2h_k-\eta\frac{2g^2}{\pi^2}\mu_5\rho_k\,. \qquad (2.32)\end{aligned}$$

The evolution of the total magnetic helicity density yields

$$\partial_t h = -2\eta\int dk\left(k^2h_k+\frac{g^2}{\pi^2}\mu_5\rho_k\right), \tag{2.33}$$

and the magnetic energy density evolution can be cast in the form

$$\partial_t \rho_m = -2\eta \int dk k^2 \left(\rho_k + \frac{g^2}{4\pi^2} \mu_5 h_k \right) . \tag{2.34}$$

Such derivation of (2.33) and (2.34) can also be found, e.g., in Appendix D of Ref. [42].

To study an MHD system under the presence of a chiral asymmetry, apart from the MHD equations, it is pivotal to understand the evolution of the asymmetry itself, which will be coupled to the MHD equation's evolution, as is clear from (2.14).

Chiral Asymmetry Evolution

The development of a chiral imbalance will greatly depend on the system under analysis and we will particularize to the cases which will be treated in the next sections. Only cases where fields vary slowly will be considered, allowing for the assumption that chemical potentials can be treated as space-independent quantities. The effect of a μ_5 which is not homogeneous in space is given in Ref. [70] and does not change the results put forward in this work.

To express (2.14) in terms of chiral magnetic chemical potential, use

$$n_5 = \frac{\mu_5}{3\pi^2} \left(\mu_5^2 + 3\mu^2 + \pi^2 T^2 \right) , \tag{2.35}$$

where μ stands for the chemical potential of the fermionic species. Approximating to linear order in μ_5, $n_5 = c(T, \mu)\mu_5$, with

$$c(T, \mu) = \frac{\mu^2}{\pi^2} + \frac{T^2}{3} . \tag{2.36}$$

Apart from the helicity change, μ_5 changes can be induced by the mechanisms that source the chiral asymmetry or by the means by which it can be washed out. In the latter, reactions that flip the chirality of the interacting particles are to be taken into account by the rate, Γ_f, at which the reactions occur.

The evolution of the chiral chemical potential can then be written as

$$\partial_t \mu_5 \simeq \frac{g^2}{4\pi^2 c} \partial_t h_B - \Gamma_f \mu_5 + \Gamma_{\mathrm{sr}} \mu_{\mathrm{sr}} , \tag{2.37}$$

with Γ_{sr} the rate of the injection term and μ_{sr} the chemical potential of particles that source the instability.

2.2 The Chiral Magnetic Effect in Protoneutron Stars

This section presents an overview of a field that has recently blossomed, viz. the application of the CME to compact astrophysical objects with strong magnetic fields. A detailed look at the case of neutron stars will be taken.

Observations of magnetars, which are highly magnetized neutron stars [71,72], indicate surface magnetic fields of up to the order of 10^{15} G [16,73]. The origin of these strengths is still under debate [74]. The two most common hypotheses for the generation of the fields of neutron stars are adiabatically compressed fossil fields of the parent star [75] and dynamo generated fields [76, 77]. In general, fossil fields would not be sufficiently stable with time in order to account for the magnetic field over the star's lifetime [78]. Fields generated via dynamo mechanisms are typically not sufficiently strong and it is complicated to explain why rotation does not seem to be correlated with the field strength [79]. Several additional effects and mechanisms have been considered to improve these models [80].

It has been recently suggested that the magnetic field of magnetars can be related to the chiral asymmetry produced during the core collapse of supernovae [81]. The literature developed in this topic indicates that in a pure electron-positron plasma, the CME does not allow the growth of seed magnetic fields [82], but an electroweak plasma with neutrino-antineutrino asymmetries was found to be able to amplify magnetic fields to interesting scales for neutron stars [83]. A crucial point is the finite electron mass, which violates chirality, even though in this system electrons are relativistic. Spin flip interactions might tend to decrease the asymmetry between left- and right-handed electrons faster than it is created by electroweak processes [84]. It was also claimed that the chiral asymmetry in the forward scattering amplitude of electrons off nuclei due to electroweak interactions could create a field instability analogous to the chiral asymmetry, but which is not washed out by chirality flipping processes and acts on much longer time scales [85, 86]. This would, however, violate energy conservation and a mechanism to quench the magnetic field growth is required [87]. This hypothesis was criticised in Ref. [1] and later in Ref. [88]. The possibility of generating field strengths of the magnetar order through the CME is being studied in quark stars [89, 90], where electrons do not need to be approximated to chiral particles, but where further questions related to the treatment of chirality flips in quark dense matter arise.

Approaches under different assumptions find different results, awakening our interest to review them, model the conditions of the interior of the neutron star and follow the evolution of the asymmetry and magnetic energy. The basic approach that follows considers electrons interacting with a thermal bath of particles. The guiding line can be expressed through the question: can the chiral magnetic instability in neutron stars and magnetars transfer sufficient energy from chiral fermions into the magnetic field to significantly contribute to these object's magnetic fields?

2.2.1 Basic Thermodynamics in the Interior of a Neutron Star

When a massive star ($M > 8M_{\odot}$) at the end of its life becomes unstable and then collapses, it ejects its outer mantle in a SN explosion such that, within fractions of a second, the core forms a compact object at supranuclear densities – a protoneutron star (PNS) – which will, with time and after cooling down, become a neutron star (NS) [91].

The study of the density in a protoneutron star core is a field in itself and densities above the nuclear matter density $n_0 \simeq 1.7 \times 10^{38}$ cm^{-3} are easily reached. In our simplified model we assume a general and constant baryon number density $n_B = 2n_0$.

Immediately after collapse, the core reaches temperatures of the order of tens of MeV [92]. At the typical temperatures of the PNS core, neutrinos of energy $E_\nu \simeq 3T$ are trapped inside the core, which in other words means that neutrinos do not escape the NS until their mean free path becomes larger than the star radius (typically of 10 km). This is important to keep in mind since as a result (I) the lepton fraction Y_L is temporarily conserved and (II) neutrinos are available to react with neutrons and wash out the chiral asymmetry caused by electron capture.

The neutrino mean free path for absorption by a neutron is [93]

$$\ell_{\text{abs}} \simeq 4.5 \times 10^6 \left(\frac{n_0}{n_B}\right)^{2/3} \left(\frac{10\,\text{MeV}}{T}\right)^4 \left[\left(\frac{E_\nu}{T}\right)^4 + 10\pi^2 \left(\frac{E_\nu}{T}\right)^2 + 9\pi^4\right]^{-1} \text{cm}, \tag{2.38}$$

while the neutrino mean free path to scatter with a neutron is [93]

$$\ell_{\text{sca}} \simeq 10^4 \left(\frac{n_0}{n_B}\right)^{1/3} \left(\frac{10\,\text{MeV}}{E_\nu}\right)^2 \frac{10\,\text{MeV}}{T}\ \text{cm}. \tag{2.39}$$

To a given temperature corresponds a chemical potential difference $\Delta\mu = \mu_n - \mu_p = \mu_e - \mu_\nu$ [92], where μ_i is the chemical potential of the particle species i, that can be used together with (I). The number densities and chemical potentials of the particle species involved can then be estimated using the condition $Y_L n_B = n_e + n_\nu$, where $n_B = n_n + n_p$ and n_i denotes the number density of the particle species i, and using electric neutrality, $n_e = n_p$.

Another necessary parameter that figures in (2.33) and (2.34) is the star's conductivity. For a mature (cold) neutron star, it can be written in the form [94]

$$\sigma^{\text{cold}} = 1.6 \times 10^{28} \left(\frac{n_e}{10^{36}\text{cm}^{-3}}\right) \left(\frac{T}{10^8}\right)^{-2} \text{s}^{-1}\,, \tag{2.40}$$

while in the initial phase (hot), the charge carriers in the protoneutron star are most likely semi-degenerate. Since describing it with a simple expression is not an easy task, we consider both the conductivity in the degenerate limit [95],

$$\sigma^{\text{hot}}_{\text{deg}} \simeq 1.5 \times 10^{45} \left(\frac{\text{K}}{T}\right)^2 \left(\frac{\rho_p}{10^{13}\ \text{g}\,\text{cm}^{-3}}\right)^{3/2} \text{s}^{-1}\,, \tag{2.41}$$

with ρ_p the proton density, as well as in the non-degenerate (and high temperature) limit. In the latter we assume that $\sigma^{\text{hot}}_{\text{nd}} \simeq T$, since the conductivity in this regime is dominated by the pair plasma and expected to be comparable approximately to the early Universe temperature, where it follows $\sigma \simeq 0.76T$ [96].

Although $\sigma_{\mathrm{nd}}^{\mathrm{hot}} < \sigma_{\mathrm{deg}}^{\mathrm{hot}}$, our results are not sensitive to which limit we take for the conductivity and therefore we motivate *a posteriori* the use of (2.41) in our calculations. In the protoneutron star case, one deals with small timescales, therefore being reasonable to make the simplifying approximation that conductivity and temperature are constant.

URCA Rate

Neutron star is a well deserved name for these objects due to the extraordinary amount of neutrons composing them: in the collapse of the parent star, the chemical elements are first stripped of electrons and then divided into nucleons due to the pressure. Nuclear densities are expected in the core of the neutron star. What is of special interest for the study of the chiral anomaly is the conversion of protons into neutrons by capturing left-handed electrons $e_L + p \to n + \nu_{e_L}$, since this electroweak reaction produces an asymmetry between the number of left- and right-handed electrons. These inverse beta decays in NSs are known as URCA processes and their emissivity is given by [97]

$$\epsilon_{\mathrm{URCA}} = \frac{457\pi}{10080}(1 + 3g_A^2)\cos^2\theta_C G_F^2 m_n m_p \mu_e T^6 \,, \tag{2.42}$$

with $g_A \simeq 1.26$ being the axial-vector coupling of the nucleon, $\theta_C \approx 0.24$ the Cabbibo angle, $G_F = 1.166 \times 10^{-5}$ GeV^{-2}, m_n and m_p are the masses of the neutron and proton, respectively. The typical electron chemical potential is of the order of about 300 MeV [91], thus $\mu_e \gg T$ and the electron capture rate can be written as

$$\Gamma_w = \frac{\epsilon_{\mathrm{URCA}}}{\mu_e Y_L n_B} \,. \tag{2.43}$$

URCA processes can only effectively create an asymmetry n_5 if they are not in thermodynamic equilibrium with the inverse reactions. This can happen if neutrinos escape the neutron star, for example after the protoneutron star gets transparent to neutrinos or beyond the neutrino sphere, which is the last scattering surface where neutrinos are bound to the star.

On a neutron star (or in the crust of a PNS) the density of protons and electrons is low, such that momentum conservation highly suppresses electron capture. In the case for which $p_{F,n} > p_{F,e} + p_{F,p}$, the modified URCA process takes place, $N + p + e_L \to N + n + \nu_{e_L}$, which stands in need of an additional particle N from the background – another proton or neutron – to absorb momentum. It has a rate [98]

$$\Gamma_w^{\mathrm{mod}} \simeq \frac{11513\pi}{120960}\alpha_\pi^2 G_F^2 \cos\theta_C g_A^2 \frac{T^8}{Y_L n_B} \,, \tag{2.44}$$

where $\alpha_\pi \approx 15$ is the pion-nucleon fine structure constant.

Chirality Flipping Rate in a Protoneutron Star

In a neutron star, the reactions that change the chirality of electrons are a consequence of them being massive particles. The amplitude of a positive helicity component for a left-chiral state is approximately $(E+m_e-p)/(E+m_e) \simeq (m_e/E)$, where E is the energy, p the momentum and m_e is the mass of the electron. This implies an approximate probability $(m_e/E)^2$ that an electron of a certain chirality flips into the opposite chirality state via scattering – either Rutherford, electron-electron or Compton scattering. The dominating process in this case is Rutherford scattering, allowing us to write the chirality flipping rate as [84]

$$\Gamma_f \simeq \frac{e^4 m_e^2}{48\pi^3 \mu_e}\left[\log\left(\frac{12\pi^2 T}{e^2(3T+\mu_e)}\right) - 1\right] , \tag{2.45}$$

where e is the electron charge and $E \approx T$ is assumed.

Density Fluctuations

The interior of a young neutron star is bound to be a turbulent environment. However, in order to proceed in a simplified frame of work we see ourselves forced to make simplifying assumptions, such as considering that density fluctuations $\delta\rho$ relative to the average density ρ can model the turbulent nature of the PNS core. Studies have shown that such fluctuations seem to be at the level of 25% at least [99]. If the neutrino mean free path is larger than the scale of the perturbations, neutrinos free stream on that scale. This is equivalent to having the URCA and reverse processes locally not in thermal equilibrium. This means that the rate of production of the chiral asymmetry will be of the order of the direct URCA rate Γ_w. One can then define an effective chiral asymmetry creation rate $\Gamma_w^{\text{eff}} \equiv \Gamma_w \delta\rho/\rho$, which is meant to account for the difference in absorption and emission rates of left-handed electrons due to the electroweak URCA interactions.

2.2.2 Evolution Equations and Energy Balance

Amplification of Magnetic Field

Let us now investigate what is the effect expected for the chiral magnetic effect to have on the seed magnetic field of a neutron star. This seed field can for example result from adiabatic compression of the stellar field during collapse, supported by the conservation of magnetic flux, which is referred to as flux freezing [74]. A parent star with a strong magnetic field of $B_{\text{core}} = 10^3$ G in the core and with a typical core radius of $R_{\text{core}} = 10^5$ km, would generate a neutron star magnetic field of the order of $B_{\text{NS}}^0 \approx (R_{\text{core}}/R_{NS})^2 B_{\text{core}} \approx 10^{11}$ G.

The way in which the seed field is affected in the presence of a chiral instability depends on the scale, as the modes k in (2.34) which grow need to obey

$$k < \frac{2e^2}{\pi}|\mu_5| \equiv k_5(\mu_5)\,, \tag{2.46}$$

while magnetic field modes $k > k_5$ decay due to the finite conductivity with the resistive damping rate $\Gamma_r = \eta k^2$. On the other hand, when $k < k_5$ and when μ_5 has a sign opposite to helicity, the chiral asymmetry grows at a rate

$$\Gamma_\chi(k) = \frac{2e^2}{\pi}\eta k|\mu_5| = \frac{k_5}{k}\Gamma_r\,. \tag{2.47}$$

This way, we also obtain that the total growth rate $\Gamma_{\text{tot}} = \Gamma_\chi - \Gamma_r$ will be maximal when $\Gamma_{\max} = \eta k_5^2/4$, which corresponds to the wavenumber $k_5/2$.

To evaluate (2.37) we have yet to define the chemical potential of the particles that act as the asymmetry's source, a role delegated to the thermal bath of particles that our system is embedded in and with which electrons interact. In the absence of conductivity, this effective chemical potential, which we will call μ_b, would be the equilibrium value of μ_5. It can be tentatively estimated by looking at the interplay between the number density of background species, n_b, and the asymmetry, n_5. In the absence of the magnetic field term, the processes that induce a change of left- and right-handed electrons can be written as

$$\partial_t n_5 = \pm\frac{\delta\rho}{\rho}\Gamma_w n_b - 2\Gamma_f n_5\,. \tag{2.48}$$

Writing the number density of background species in terms of an effective chemical potential, one has

$$n_b = 2c(T,\mu_e)\frac{\rho}{\delta\rho}\frac{\Gamma_f}{\Gamma_w}|\mu_b|\,, \tag{2.49}$$

where μ_b is, as mentioned, the equilibrium value of μ_5 in the absence of resistivity, which will evolve in time. This is a way in which a contribution from different scattering amplitudes of left- and right-handed electrons with background nucleons can be accounted for: this contribution will be included in μ_b. For example in Refs. [85,86], that contribution is taken as an effective potential, the consequences of which will be discussed later.

The number of background particles in the non-degenerate relativistic limit can be related with the temperature using thermodynamics, with g_b degrees of freedom, such that $n_b = 3\zeta(3)g_bT^3/(2\pi)^2$. Together with (2.49), this yields

$$|\mu_5^{\text{eq}}(T)| = \frac{3\zeta(3)}{8\pi^2}g_b\frac{\delta\rho}{\rho}\frac{\Gamma_w}{\Gamma_f}\frac{T^3}{c(T,\mu_e)}\,. \tag{2.50}$$

It is also possible to derive a characteristic wavenumber for the instability. Inserting (2.50) in (2.46), that is obtained as

$$k_5^{-1} = \frac{4\pi^3 c(T,\mu_e)}{3e^2\zeta(3)g_b}\left(\frac{\delta\rho}{\rho}\frac{\Gamma_w}{\Gamma_f}T^3\right)^{-1}\,. \tag{2.51}$$

The dependence of the evolution of the asymmetry on (2.43) will be included in the chemical potential μ_b, as it represents the effective chemical potential that the interactions of electrons with the background species generate. Then, (2.37) can be rewritten in the form

$$\partial_t \mu_5 = \frac{e^2}{4\pi^2 c(T,\mu_e)} \partial_t h_B - 2\Gamma_f \left(\mu_5 - \mu_b\right) . \tag{2.52}$$

The change of energy density associated with the presence of the chiral asymmetry, ρ_5, by the chemical potential definition, will be $d\rho_5 = \mu_5 dn_5$. Setting $\rho_5 = 0$ for $\mu_5 = 0$, one obtains $\rho_5 = c\mu_5^2/2$.

In a similar way, the energy density ρ_b associated with the background species is given by $d\rho_b = \mu_b dn_b$. By using (2.49), one obtains

$$\rho_b = c(T,\mu_e) \frac{\rho}{\delta\rho} \frac{\Gamma_f}{\Gamma_w} \mu_b^2 . \tag{2.53}$$

Beginning from a finite initial chiral chemical potential μ_5^i, what is the maximal change in magnetic energy that the CME can induce? The chiral instability produces maximally helical fields and taking the wavenumber at which the growth peaks, $k_5/2$, it is estimated that $d\rho_m \simeq k_5 |dh_b|/(8\pi)$. The conservation law (2.11), relating the helicity change with the chiral number, allows us to obtain $d\rho_m \simeq c\mu_5 d\mu_5$. From here follows that the increase in magnetic energy density is given by

$$\Delta\rho_m \simeq \frac{c}{2} \left[(\mu_5^i)^2 - \mu_5^2 \right] . \tag{2.54}$$

And if all energy initially stored in background species is transferred into chiral energy, we obtain yet another way to express the maximal induced magnetic energy density

$$\Delta\rho_m \lesssim c \frac{\rho}{\delta\rho} \frac{\Gamma_f}{\Gamma_w} (\mu_b^i)^2 , \tag{2.55}$$

which, after inserting (2.50) into it, leads to

$$\rho_m^{\max} = \left(\frac{3\zeta(3)}{8\pi^2} g_b \right)^2 \frac{\delta\rho}{\rho} \frac{\Gamma_w}{\Gamma_f} \frac{T^6}{c} , \tag{2.56}$$

taking the degrees of freedom of the background to be $g_b = 2$. In terms of magnetic field strength, the maximal amplification $B_{\max} = \sqrt{2\rho_m^{\max}}$ then becomes

$$B_{\max} \simeq \frac{3\zeta(3) g_b}{[2\pi^2 c]^{1/2}} \left(\frac{\delta\rho}{\rho} \frac{\Gamma_w}{\Gamma_f} \right)^{1/2} T^3 . \tag{2.57}$$

This enables a prediction of the maximal field strength that can be generated at a given temperature, as shown in Fig. 2.1. In this plot, it is clear that the maximal magnetic field amplification strongly increases with temperature, which is a consequence of the stronger dependence of Γ_w with temperature when compared to Γ_f – as figures on the left panel. Note also that $B_{\max}$ is expected to be independent from the initial seed magnetic field (B_0). The temperature dependence of the ratio between the rates that act as source and sink, $\Gamma_w^{(\mathrm{mod})}/\Gamma_f$, is the important parameter in the establishment of the equilibrium value μ_5^{eq}.

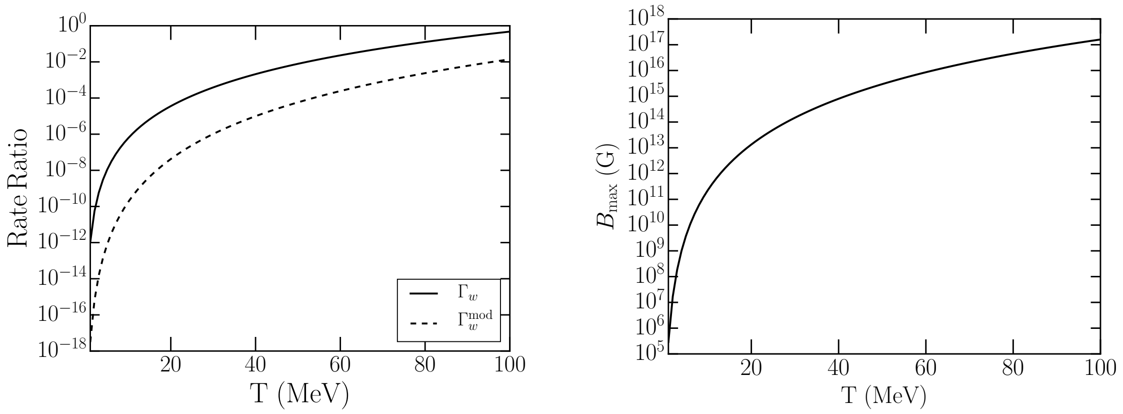

Figure 2.1: *Left:* Ratio between the URCA and chirality flipping rates Γ_w/Γ_f and $\Gamma_w^{\rm mod}/\Gamma_f$, obtained using (2.43), (2.44) and (2.45). *Right*: Estimate of the maximum magnetic field amplification due to the chiral magnetic instability as a function of temperature.

Energy Conservation

The total energy density of the system counts with the contribution from ρ_5, ρ_b and the change induced in the magnetic energy density by the anomaly, meaning that

$$\rho_{\rm tot} \simeq c(T,\mu_e)\left(\frac{\rho}{\delta\rho}\frac{\Gamma_f}{\Gamma_w}\mu_b^2\frac{(\mu_5^i)^2}{2}\right) , \tag{2.58}$$

which does not depend on μ_5 explicitly but only on its initial value. Let us note that the maximal increase in magnetic energy density obeys $\Delta\rho_m \leq \rho_{\rm tot}$, as would be expected.

Energy conservation requires that $\partial_t\rho_b = -\partial_t\rho_5$ for interactions in the absence of magnetic fields. It is by computing the time derivative of (2.53) that one obtains for the evolution equation of the background species

$$\partial_t\mu_b = -\frac{\delta\rho}{2\rho}\frac{\Gamma_w}{\Gamma_f}\frac{\mu_5}{\mu_b}\partial_t\mu_5 \, . \tag{2.59}$$

Using (2.52), in the absence of magnetic field it can be cast it in the form

$$\partial_t\mu_b = \frac{\delta\rho}{\rho}\Gamma_w\frac{\mu_5}{\mu_b}(\mu_5-\mu_b) \, . \tag{2.60}$$

From this evolution equation, one observes that when the magnetic field is concentrated around $k_5(\mu_b)$ and maximally helical, μ_b will be in equilibrium when $\mu_b = \mu_5$ and that it will depend on the rate $\Gamma_w^{\rm eff}$.

The question of energy conservation when studying the CME, as important as it is, is not straightforward. The maximal magnetic energy induced through the chiral asymmetry would continuously grow with temperature, which can be seen in Fig. 2.1. The energy transferred to the magnetic field from the chiral imbalance is in its turn transferred from the medium where the particles are embedded. It is not only the ratio between chirality flips and URCA that regulates the evolution of μ_5, but more importantly, the back-reaction on the background medium. This is encoded through μ_b, which ultimately limits the field growth. This will be clearly seen in the numerical treatment of the protoneutron star both in terms of the evolution of μ_b and of ρ_m. The evolution of the background species being consistently treated and coupled to the evolution of the chiral asymmetry – and, thus, to the field evolution – ensures the conservation of energy in the system. The importance of the requirements leading to (2.59) is to be stressed in the light of studies where magnetic field growth was either allowed infinitely [85, 86]; had to be halted by *ad hoc* means [87]; or was connected to the background bath in what seems an ill-defined way, since it does not self-consistently enter the evolution equations [100].

After deriving (2.52) and (2.60), they can now be solved together with the evolution equations that regulate the magnetic part for the neutron star system, and which we will in the next section.

2.2.3 Solutions to the Evolution Equations

A core collapse supernova as described by Ref. [91], with a progenitor of mass $\sim 8M_\odot$, has a lepton fraction $Y_L \simeq 0.3$ shortly after collapsing. As mentioned previously, let us take a core density of $2n_0$. The temperature at the core in these first moments is dictated by the chemical potential difference $\Delta\mu$. For comparison, we consider two realistic cases throughout this section: $\Delta\mu = 80$ MeV and 60 MeV, corresponding to a temperature $T \simeq 40$ MeV and 20 MeV, respectively [92].

With the ingredients put forward in §2.2.1, one computes the number density and chemical potential of each species, obtaining an electron chemical potential $\mu_e \simeq 260$ MeV and the proton densities $\rho_p \simeq 1.3 \times 10^{14}\,\mathrm{g\,cm^{-3}}$ for 40 MeV and $1.2 \times 10^{14}\,\mathrm{g\,cm^{-3}}$ for 20 MeV. Using (2.41), we obtain then the conductivity of the PNS.

The absorption mean free path (2.38) yields $\ell_{\rm abs}(20\,\mathrm{MeV}) \simeq 1.5$ m and $\ell_{\rm abs}(40\,\mathrm{MeV}) \simeq 10$ cm, while for the scattering mean free path (2.39), we have $\ell_{\rm sca}(20\,\mathrm{MeV}) \simeq 1$ m and $\ell_{\rm sca}(40\,\mathrm{MeV}) \simeq 14$ cm. Absorption dominates since $\ell_{\rm abs} > \ell_{\rm sca}$.

The timescale is normalized to the instability's resistive damping time

$$\begin{aligned} t_{\rm damp} &= \Gamma_\chi^{-1}(k_5) = \frac{2}{\eta k_5^2} \\ &= \frac{32\pi^6 c(T,\mu_e)}{9\zeta(3)^2 e^4 g_b^2 \eta} \left(\frac{\delta\rho}{\rho}\frac{\Gamma_w}{\Gamma_f} T^3\right)^{-2}, \end{aligned} \tag{2.61}$$

which yields the values $t_{\rm damp}(40\,\mathrm{MeV}) \simeq 6 \times 10^{-8}$ s and $t_{\rm damp}(20\,\mathrm{MeV}) \simeq 0.04$ s.

The scaling of the instability and of the critical wavenumber with time can also be estimated. According to (2.34), resistive damping occurs when $2\eta k_5^2 t \sim 1$. In this regime,

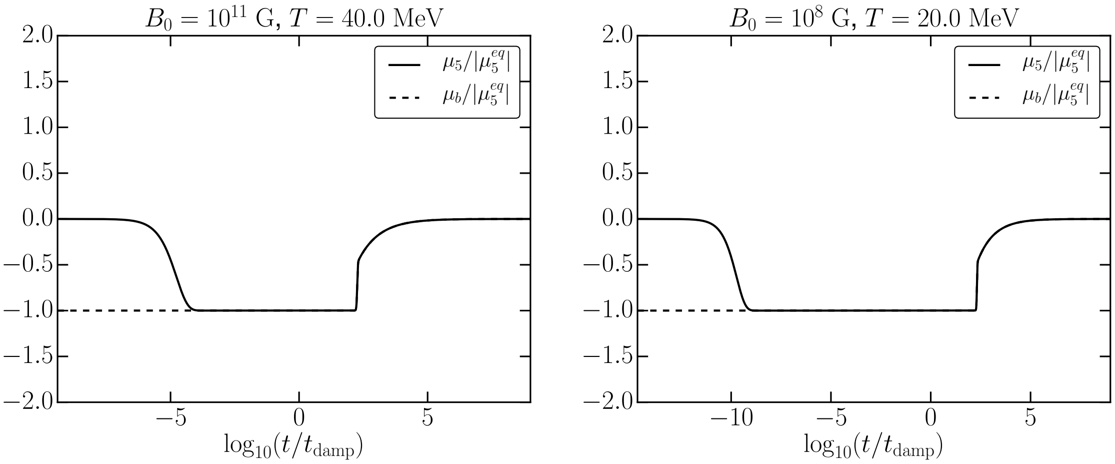

Figure 2.2: Evolution of the chiral and background species chemical potentials normalized to the equilibrium value, (2.50), $|\mu_5^{eq}|$, according to (2.52) and (2.60). Left and right panels representing different seed magnetic fields B_0 and temperatures.

we therefore expect

$$\mu_5(t) \sim \mu_5(t_{\rm damp}) \left(\frac{t_{\rm damp}}{t}\right)^{1/2} ; \quad k_5(t) \sim k_5(t_{\rm damp}) \left(\frac{t_{\rm damp}}{t}\right)^{1/2} . \tag{2.62}$$

The system of equations composed of (2.33), (2.34), (2.52) and (2.60) is solved for wavenumber modes that span from $k_{\rm max} = 2k_5$ to $k_{\rm min} = 10^{-4}k_5$.

In the Protoneutron Star Core

First let us consider what happens in the interior of the PNS when density fluctuations can be compared to the average density $\delta\rho \simeq \rho$. This is also the case after 10 s of the collapse, since then the neutron star becomes transparent to neutrinos and this is equivalent to $\delta\rho/\rho = 1$.

We assume that at collapse, the chiral magnetic chemical potential, from here onwards abreviated to chiral chemical potential, is vanishing and plot in Fig. 2.2 its time evolution. The capture of left-handed electrons through URCA processes is well reflected by the generation of an asymmetry. It reaches equilibrium at the point when $\mu_5 = \mu_b$ and the URCA rate is equilibrated by spin flips. This corresponds, using (2.50), to $|\mu_5^{\rm eq}(40\,{\rm MeV})| \simeq 2 \times 10^{-3}$ MeV and $|\mu_5^{\rm eq}(20\,{\rm MeV})| \simeq 4 \times 10^{-6}$ MeV. The chiral asymmetry begins then to decrease as chiral energy is transferred into magnetic one. This takes place when, in (2.52), the term that includes magnetic helicity becomes dominant. This confirms, as expected according to the damping timescale and the equilibrium value of the instability (see also left panel of Fig. 2.1), that the higher the temperature, the larger μ_5 and the sooner the development and following damping of the chiral magnetic instability.

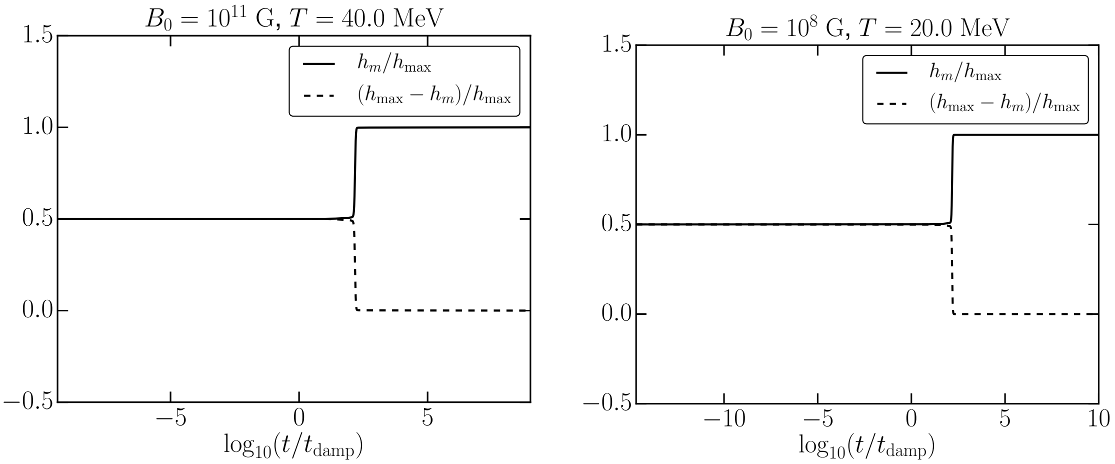

Figure 2.3: Evolution of the helicity density normalized to its maximal value, $h_{\max}$. Left and right panels representing different seed magnetic fields B_0 and temperatures.

The background species chemical potential and μ_5 have the same values after equilibrium is reached, as pointed out by Fig. 2.2. After the magnetic field term becomes preponderant, μ_5 and μ_b evolve closely. We can picture the interplay between different terms as follows: the chiral chemical potential grows due to electron capture, as the energy stored in background particles is transferred to chiral fermions until an equilibrium is reached; this energy is then transferred into magnetic energy and, as the chiral chemical potential cannot get replenished – due to the scattering of electrons – the chiral asymmetry is drained.

With respect to the behaviour of helicity density portrayed in Fig. 2.3, we see that it will keep its initial value – which was chosen to be $h^0 = h_{\max}/2$ – until it is amplified or decays when the magnetic term dominates the evolution of μ_5. If the sign between helicity and μ_5 is the opposite, the former grows, while when it is the same, helicity decreases. In the regime of amplification, fields turn maximally helical, $h_{\max}(k) = 2\rho_k/k$. The helicity evolution is rather independent on its initial value.

In both Figs. 2.2 and 2.3, there is no difference between the plots of higher and lower temperature, showing that when the chemical potentials are normalized to the asymmetry equilibrium value and the time to the damping timescale, different core temperatures robustly yield the same relative results and characteristic features.

For the seed magnetic field we chose $B_0 = 10^{11}$ G for $T = 40$ MeV and $B_0 = 10^8$ G for $T = 20$ MeV, as a way to illustrate that magnetic field amplification is limited by energy conservation when the magnetic energy approaches the predicted maximum values allowed by (2.57), $B_{\max}(40\,\text{MeV}) \simeq 8 \times 10^{14}$ G and $B(20\,\text{MeV}) \simeq 1 \times 10^{13}$ G. Indeed in Fig. 2.4 the magnetic energy density grows steeply and close to the total system's energy. This corresponds to an amplification of the seed field up to $B(40\,\text{MeV}) \simeq 1 \times 10^{14}$ G

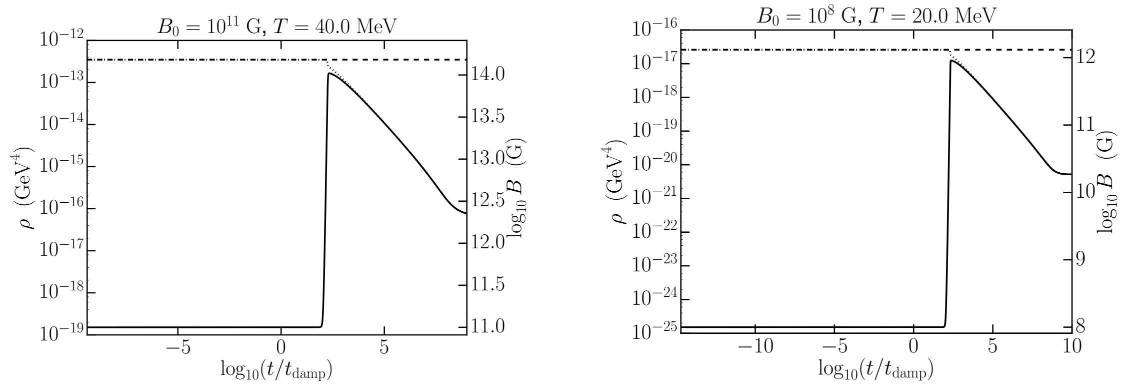

Figure 2.4: Initial total energy density $\rho^0_{\rm tot}$ (dashed curve), evolution of the magnetic energy density ρ_m (solid curve) and of the total energy density $\rho_{\rm tot}$ (dotted curve). Left and right panels representing different seed magnetic fields B_0 and temperatures.

within a few μs of the core collapse, followed by resistive damping within a few seconds. It corresponds to an analogous growth peaked at $B(20\,\text{MeV}) \simeq 1 \times 10^{12}$ G within about 4 seconds.

One confirms that the total energy of the system (2.58) does not exceed the initial value and it decays only thanks to resistive damping, when ρ_m is also dissipated. The magnetic energy has approximately a linear decay with time.

Another question that naturally arises is what is the magnetic field power spectrum evolution. This is shown in Fig. 2.5, where $M_k = k\rho_k$ and a flat spectrum is compared with a Kolmogorov initial distribution, for $T = 40$ MeV. The final spectra are not very sensitive to the initial power spectrum, which was to be expected since the magnetic energy generation and damping is regulated by the CME and resistivity. The maximum of the power spectrum is observed to occur close to $k_5/2$. It decays in time above it, for $k > k_5$. With time, this peak moves to smaller wavenumbers. From (2.46) we have that $k_5(t) \propto \mu_5(t)$, which justifies the evolution of the magnetic energy spectrum: in Fig. 2.2, for $\log(t/t_{\rm damp}) > 2$ the chiral chemical potential decreases steeply at first and smoothly at last, making the magnetic power spectrum also grow exponentially for $10^2\, t_{\rm damp} \lesssim t \lesssim 10^3\, t_{\rm damp}$, while for later times it then saturates and is damped.

We took the most relevant wavenumber modes for the system, knowing and confirming that the field power is peaked at around $k_5/2$. When considering also much smaller modes, namely up to the radius of the neutron star, $k^{-1} \sim 10$ km, the results did not present any significant change.

Through Fig. 2.5, it is possible to estimate at which length scale the power spectrum will peak after magnetic field growth ends. We obtain $k^{-1}(40\,\text{MeV}) \simeq 0.1$ mm and $k^{-1}(20\,\text{MeV}) \simeq 3$ cm. As these values are small compared to the neutrino mean free path introduced in §2.2.1, we expect that magnetic field amplification is possible in the presence

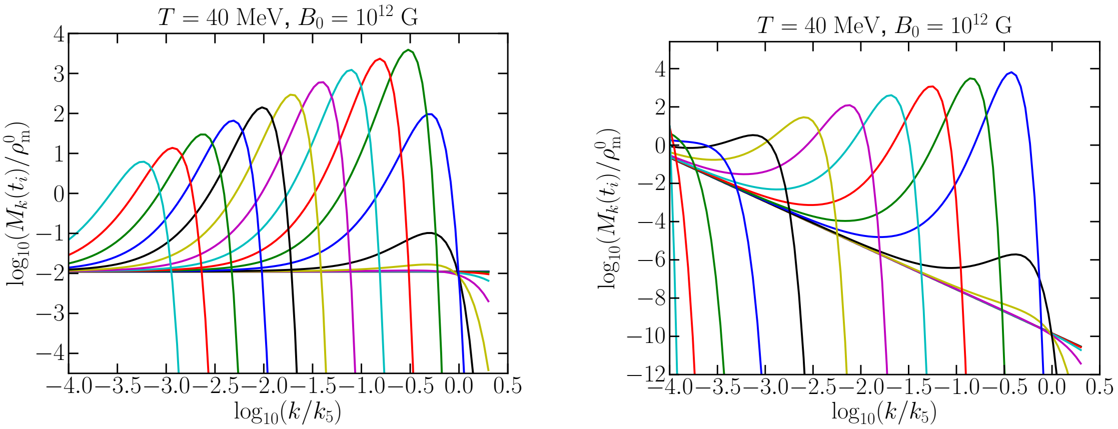

Figure 2.5: Evolution of the magnetic field spectrum normalized to the initial magnetic energy density, $M_k(t_i)/\rho^0_m$, with respect to the wavenumber k, normalized to k_5. Power spectra shown for equally spaced time intervals t_i between $t = t_{\rm damp}$ and $t = 10^8 t_{\rm damp}$ for $T = 40$ MeV. *Left:* Initially flat power spectrum. *Right:* Initial Kolmogorov power spectrum. From Ref. [1].

of significant density fluctuations on these scales.

Finally, let us briefly investigate what happens when we consider that the core density fluctuations are one order of magnitude smaller than the average core density of the NS, as presented in Fig. 2.6 and in Fig. 2.7. In this case, for a seed magnetic field of 10^{11} G, the maximal field growth obtained is $B(40\,{\rm MeV}) \simeq 10^{13}$ G. For a seed magnetic field of 10^8 G the peak of the magnetic field energy amplified by the chiral asymmetry would be $B(20\,{\rm MeV}) \simeq 2 \times 10^{11}$ G. This means that compared to the previous case, the field amplification decreases by about one order of magnitude as well. Since in Fig. 2.5 one concluded that the initial spectral shape will not be significant, the spectral evolution is now shown only for a Kolmogorov spectrum, but for two different temperatures and seed fields. It is verified that above $k = k_5/2$ the modes decay very rapidly. It is also noticeable that at 20 MeV the field enhancement effect is more concentrated in relative time than at 40 MeV.

Inside the Neutrino Sphere and in Cold Neutron Stars

At the neutrino sphere, the average neutrino energy can be at most 16 MeV [101], implying a temperature of $T \sim E_\nu/3 \sim 5$ MeV. The density at the neutrino sphere of a neutron star with 10 km of radius is about $10^{11}\,{\rm g\,cm^{-3}}$ and in this case the lepton fraction can be taken to be $Y_L \simeq 0.1$ [102]. Under these (and lower temperature) conditions, it is through the modified URCA process that a chiral asymmetry can build up, taking an additional nucleon for electron capture. Using the rate (2.44) in (2.50), the resulting chiral chemical potential would be of the order of $|\mu_5^{\rm eq}| \sim 10^{-12}$ MeV. The estimated maximal magnetic

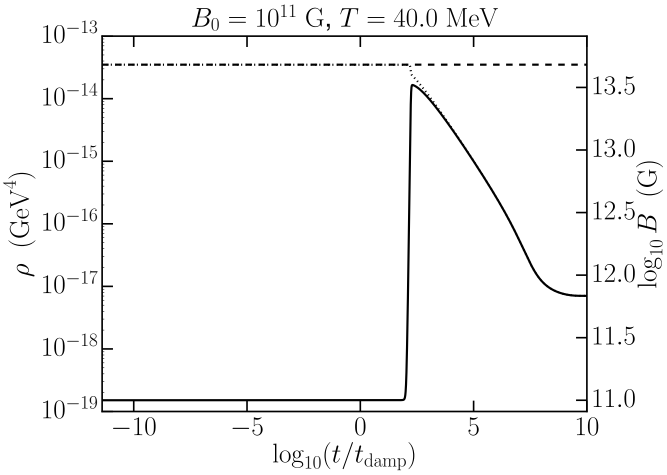

Figure 2.6: Energy density obtained for core density fluctuations $\delta\rho/\rho = 0.1$. Initial total energy density $\rho^0_{\rm tot}$ (dashed curve), evolution of the magnetic energy density ρ_m (solid curve) and of the total energy density $\rho_{\rm tot}$ (dotted curve).

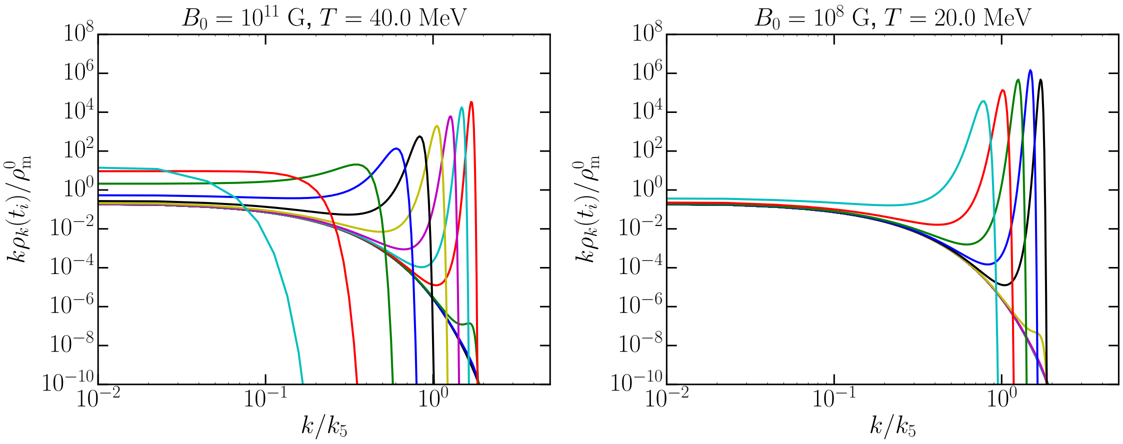

Figure 2.7: Evolution of the magnetic field spectrum normalized to the initial magnetic energy density, with respect to the wavenumber k normalized to k_5. Power spectra shown for equally spaced time intervals t_i between $t = t_{\rm damp}$ and $t = 10^8 t_{\rm damp}$ for an initial Kolmogorov spectrum and for core density fluctuations $\delta\rho/\rho = 0.1$. Left and right panels representing different seed magnetic fields B_0 and temperatures.

field (2.57) obtained is in this case negligible.

As one can notice, temperature is one of the key parameters in estimating whether a signifcant chiral asymmetry can be generated, which in its turn gives rise to magnetic field growth. A mature neutron star with a typical age of 10^5 years has cooled down to, typically, around 2×10^8 K. At this point the main cooling mechanism is surface photon emission [91]. Computing the modified URCA rate, the equilibrium chiral chemical potential is $|\mu_5^{\mathrm{eq}}| \sim 10^{-32}$ MeV, which – in a way analogous to the neutrino sphere of a PNS – transfers energy to the magnetic sector in extremely large time scales and to large length scales. Hence, generating magnetic fields stronger that the seed one via CME does not seem likely. In Refs. [85, 86], this hypothesis was considered plausible due to a constant term V_5 representing the difference in the forward scattering amplitudes for left- and right-chiral electrons. That term entered the magnetic field evolution and acted as a steady source of magnetic energy, but it was not introduced consistently in the evolution of the chiral asymmetry and therefore it lead to an infinite growth of magnetic energy. This was overcome by prescribing the saturation of magnetic field for $\mu_5 + V_5 \to (\mu_5+V_5)[1+(B/B_{eq})^2]^{-1}$ by hand, where B_{eq}^2 would be some maximal field value [87]. This was later refined and V_5 linked to thermal background particles [100]. However, that was realized in a different way than μ_b has been incorporated in the present approach. There, the background is allowed to feed energy to the magnetic sector, but that is assumed not to have implications on the evolution of μ_5. A term with such properties has been previously discussed and cast aside, since the energy associated to it would not vanish when there is parity conservation, while the chiral asymmetry does [84, 88, 103].

2.2.4 Summary and Discussion

Let us list the assumptions made throughout the application of the chiral magnetic effect to neutron stars. The MHD equation regulating the evolution of the magnetic field has been approximated by neglecting the velocity field. This is justified for velocities smooth enough on the instability length scale, as well as for spectral indexes large enough – simply having an inertial frame that moves together with the plasma. While this simplifies the solution of the MHD equations and is very helpful in isolating the effect of the chiral anomaly in the system to allow for an in-depth study, it is also a disadvantage of the analysis, since turbulence effects are easily at play in the unstable environment generated after core collapse. Including them can lead to results substantially different, as argued in §2.4.

The importance that the temperature of a protoneutron star has in our results was already pointed out. It was considered, along with the conductivity, to be constant during the stage that follows the supernova collapse. It is expected to be a good approximation, because, in this setting, temperature changes within a few seconds [92], as long as $T \gtrsim 20$

MeV. Therefore, the significant timescales in our case, such as the growth scale of μ_5, are sufficiently short in comparison. For later stages of the evolution of a neutron star, where longer timescales and lower temperatures are at play, the latter's dependence on time should be taken into account, as was done in Ref. [86]. Regarding the conductivity, as mentioned in §2.2.1, rather than considering that particles are semi-degenerate in the PNS core, we approximate them to degenerate. This impacts the resistive damping time, in its turn affecting the instability growth timescale. However, this does not influence our overall results since μ_5 grows in timescales shorter than t_{damp} and than the saturation of the magnetic energy. Therefore, the maximal magnetic field amplification is not determined by the conductivity.

Additionally, we considered only the time evolution of a spatially homogeneous chiral asymmetry. The spatial evolution of the chiral chemical potential, such as put forward in Refs. [70, 104] has been neglected since in our case $\mu_5(x,t) \equiv \mu_5(t)$ is justified as follows. Inhomogeneous growing modes of μ_5 are generated if the condition $k^2/4 > 3e^4B^2/(8\pi^4T^2)$ [104] is obeyed. Our fastest growing mode being $k_5/2$, that translates into having a stable solution if $\Gamma_w/\Gamma_f < 4/\pi$. Simply looking at Fig. 2.1, one can see that, for the temperatures in the range that we have considered, this condition is fulfilled.

A debatable and well-known question to consider is whether the chiral magnetic effect can be effective in systems where chirality is not strictly conserved. The fact that our approach is based on the chiral asymmetry between electrons, which are not massless particles, could in principle be problematic [105]. In a protoneutron star, as we saw, the temperatures reached in the core are more than high enough for electrons to be fully relativistic particles at all considered times. Other works have focused on the neutrino chiral asymmetry [83]. Ideally, this question does not play a role there due to the neutrino mass being so negligible that they were thought to be chiral particles for a long time. Regardless of how small, neutrinos have some mass as well and we can ask ourselves where the boundary of masslessness really lies. Assuming that it is more likely that there has not been an abrupt transition from a chirally symmetric phase to a chirality broken phase, it appears reasonable to consider that particles that can be safely considered relativistic, and their mass neglected for general purposes, can also be used in the CME. The role of the mass of the electron is considerably visible by accounting for spin flipping processes.

So far, we have in this chapter studied how a chiral asymmetry can be connected to the growth of helical magnetic fields in compact objects via the CME. This allows us to analyse the hypothesis that this mechanism could possibly explain the magnetic field strengths observationally inferred for neutron stars and magnetars [93] and compare it with works done in similar directions. We found that shortly after the supernova core collapse, the core imbalance between left- and right-handed electrons results in $\mu_5 \sim$ eV-keV. From the total energy of the system, which stays either constant or decreases, we could estimate the maximal possible magnetic field strength achieved in this way.

For the first moments after core collapse, while neutrinos are trapped in the core, thermodynamic disequilibrium between URCA processes and their corresponding inverse reactions is a necessary condition to secure that the chiral imbalance survives. Although the contribution of both reactions would cancel out, considering that neutrinos do not escape the protoneutron star, a disequilibrium between the rates of URCA and inverse processes is conceded if neutrinos free-stream in small enough length scales. This is verified due to the mean free path of neutrinos in the core being of the order of $\ell_\nu \sim$ cm.

We report the creation of maximally helical fields from the progenitor seed magnetic field in length scales $10^{-6}\,\mathrm{cm} \lesssim \pi/(2e^2|\mu_5|) \lesssim \ell_\nu \lesssim 15\,\mathrm{cm}$ and in short timescales, relevant for protoneutron stars. The chiral asymmetry fastly transfers its energy to magnetic energy, which saturates and subsequently decreases due to resistive damping. The maximal strength of 10^{14} G for a core temperature of 40 MeV was obtained within microseconds on tens of nanometer length scales. For lower temperatures the maximal fields are lower, on longer timescales and concentrated on larger length scales. Taking into consideration that surface fields of typical magnetars are of the order of 10^{15} G, the values we obtained indicate that the CME does not offer an ideal explanation for their generation, both regarding strength and scale of fields. The chiral chemical potential μ_5, and thus our results, depend strongly on temperature. This is the key as to why outside the neutrino sphere and in cold neutron stars – below 10 MeV – we find that the chiral lepton asymmetry leads to no significant field growth.

Let us summarize in brief the differences between the recent growing literature in this topic and our approach. On the one side, magnetar surface fields of 10^{18} G were suggested in Ref. [81] based on a (constant) $\mu_5 = 200$ MeV. This value is extremely high and served only as a first estimation of the potential that the CME could have to predict magnetar fields. On the other side, Ref. [84] obtains a chiral asymmetry of the order of 10^{-12} MeV (for $T = 30$ MeV); the discrepancy when compared to our result stems from a different electroweak electron capture rate, yielding much smaller asymmetry values. In Refs. [85–87], an effective potential energy V_5 is introduced to account for the asymmetry that is formed due to the forward scattering of electrons on the background. This term, albeit small when compared with the typical μ_5 present in a hot neutron star, is introduced in the equations in a way that allows for it to act steadily. That enhances magnetic energy in much longer timescales than in our case. However, this sources magnetic energy by assuming that the scattering of electrons off the background plasma can indefinitely draw energy from it. Therefore, such works find a significant magnetic field, of the magnetar order, to be produced when the neutron star has cooled down and when μ_5 has subsided due to chirality flips. In our approach, though, such a contribution is accounted for in the chemical potential of the background species, μ_b. Its interplay with μ_5 reflects the back-reaction on the thermodynamical background, which naturally limits the magnetic field growth and ensures energy conservation.

2.3 The Chiral Magnetic Effect in the Early Universe

It is plausible that in the early Universe decays of massive particles that violated parity originated a chiral asymmetry, especially locally. In order for this potential asymmetry to influence the early Universe evolution, it is necessary that the inverse of the processes that gave rise to it do not wash it out, i.e., only an asymmetry created in out-of-equilibrium conditions could have survived. This condition is better fulfilled in cosmological phase transitions. The electroweak symmetry breaking provides the breaking scheme $SU(2)_L \otimes U(1)_Y \to U(1)_{EM}$, when electromagnetic and weak interactions decouple from each other, which naturally motivates the potential expected for the study of the effects of the chiral anomaly in this setting. Additionally, if in §2.2.4 we mentioned that neutron star electrons are not massless, and therefore not strictly chiral particles, before the electroweak transition this question does not arise.

The origin of large scale magnetic fields has been analysed for several years in many works that suggested cosmological magnetogenesis scenarios [106] during inflation [21, 23, 107, 108], electroweak symmetry breaking [40, 109, 110] and QCD transition [111–113]. Likewise, hypotheses of their origin through first order phase transitions [114, 115] and cosmic strings [116, 117] were studied. The idea that the triangle anomaly in the early Universe induces the modification of the MHD equations was first proposed in Ref. [118]. Subsequently, the implications of the chiral magnetic effect for the evolution of cosmological magnetic fields were studied in Refs. [42, 44].

In the third part of this chapter, the formalism developed in the first part, §2.1, is going to be applied to the early Universe to draw conclusions on the evolution of a chiral asymmetry around the electroweak transition and its consequences for the evolution of cosmological magnetic fields.

To portray the evolution equations in a more suitable form for the study of the expanding Universe, conformal variables are used. The Friedmann-Lemaître-Robertson-Walker metric has the form

$$ds^2 = -dt^2 + a(t)^2 \left[dx^2 + dy^2 + dy^2\right] , \tag{2.63}$$

with $a(t)$ the scale factor. Defining conformal time as $d\tau \equiv dt/a(t)$, our variables are then changed to: $\mathbf{B} \to a(t)^2\, \mathbf{B}$, $\mathbf{E} \to a(t)^2\mathbf{E}$, $\sigma \to a(t)\sigma$, $\mu_5(t) \to a(t)\mu_5$, $k \to a(t)k$, $\Gamma \to a(t)\Gamma$ [119, 120]. The scale factor, which is a solution of the Friedmann equations, is chosen to be $a(t) = T^{-1}$. Since our interest will be focused on the radiation dominated era of the evolution of the Universe, we can write conformal time as $\tau = M_*/T$, where the reduced Planck mass is $M_* = (90/8\pi^3 g_*)^{1/2} M_{Pl}$, and assume that the number of degrees of freedom is constant around the electroweak transition, $g_* \approx 106.75$. Dimensionless conformal variables are used in the following.

2.3.1 Electroweak Phase Transition

Two different evolution regimes will be analysed in order to describe the asymmetry and field evolutions, namely before and after electroweak symmetry is broken. The description of magnetic and electrical fields changes with respect to (2.17)-(2.21) since electromagnetic and weak processes are unified at the electroweak scale. At this stage we have hypermagnetic and hyperelectric fields, $\mathbf{B}^Y$ and $\mathbf{E}^Y$, respectively.

In the hot plasma before electroweak symmetry breaking, if hyperfields would be absent, the lepton number for right electrons would be conserved. In the presence of large-scale hyperfields though, due to the discussed Abelian anomaly, there is an anomalous current analogous to (2.6), which takes the form [45] (see also Refs. [121, 122])

$$\partial_\mu j_R^\mu = -\frac{g'^2 y_R^2}{64\pi^2} Y_{\mu\nu} \tilde{Y}^{\mu\nu} \,, \tag{2.64}$$

with $y_R = -2$ being the hypercharge of right-handed electrons, $Y_{\mu\nu}$ the hypercharge field strength and $\tilde{Y}^{\mu\nu}$ its dual. The non-conservation of the number density of right-handed electrons associated to the anomaly reads [118]

$$\partial_\tau n_R = \frac{g'^2}{4\pi^2} \partial_\tau h^Y - \Gamma_s n_R \,, \tag{2.65}$$

where $h^Y = V^{-1} \int d^3x \mathbf{A}^Y \cdot \mathbf{B}^Y$ is the hyper-helicity and Γ_s represents the chirality flipping rate in the symmetric region, perturbatively added. The translation of the number density into the chemical potential of right-handed electrons depends on the elementary particle model assumed. In the minimal Standard Model, it can be shown that (2.65) yields [118]

$$\partial_\tau \mu_R = \frac{g'^2}{8\pi^2} \frac{783}{88} \partial_\tau h^Y - \Gamma_s \mu_R \,. \tag{2.66}$$

In the symmetric region, the anomaly couples separately to left- and right-handed leptons, instead of to their difference μ_5 as in the broken region and in the previous sections. Alternatively, for the sake of simplicity we will follow Ref. [118] and assume that the chiral anomaly is in the symmetric phase stored only in right-handed electrons. Scenarios that take leptogenesis as the source for the baryon asymmetry of the universe are in accord with this choice.

At zero temperature, baryon number is conserved. Classically there are no transitions between two vacua states, but tunneling would allow for it – through field configurations named instantons – as long as the rate of the transition would become significant when compared to the age of the Universe, which is not the case. At higher temperatures, however, with thermal energy becoming available, the transition amplitudes from one vacuum to another become possible by rising above the potential energy barrier instead of tunneling – through field configurations called sphalerons [38]. Higgs and W bosons become unstable on the barrier around a temperature of 100 GeV, which is not too distanced from the electroweak symmetry breaking. Sphaleron processes violate lepton and baryon number and couple only to left-handed particles. To write μ_L, one would then have to take these processes into account, as in Ref. [123]. The introduction of the left-handed electron chemical potential furthermore violates the equilibrium of the chemical potentials associated with the global charge conservation of the three fermionic generations and for the weak hypercharge chemical potential, which is fixed from demanding the neutrality of the electroweak plasma. All the fermionic degrees of freedom of the electroweak (EW) theory, and the respective Boltzmann equations, do not need to be accounted for if we restrict our study to plasma processes which are slow [118]. In that case, the plasma equilibrium is negligibly disturbed. This justifies setting the left-handed chemical potential $\mu_L = 0$ in the symmetric region without much loss of generality and, therefore, the chiral asymmetry can be identified with the μ_R in this region.

The MHD equations are analogous to (2.17)-(2.21), replacing the fields by their hyper counterparts and using the right-chiral chemical potential (2.66) [118,124]:

$$\nabla \times \mathbf{B}^Y = \sigma_s \mathbf{E}^Y - \frac{g'^2}{\pi^2}\mu_R \mathbf{B}^Y \,, \tag{2.67}$$

$$\partial_\tau \mathbf{B}^Y = -\nabla \times \mathbf{E}^Y \,, \tag{2.68}$$

$$\nabla \cdot \ \mathbf{B}^Y = 0 \,, \tag{2.69}$$

$$\nabla \cdot \mathbf{E}^Y = 0, \tag{2.70}$$

where σ_s is the conductivity before electroweak symmetry breaking.

After the symmetry is broken, the hypercharge group $U_Y(1)$ tranforms into the regular $U_{EM}(1)$, corresponding to the Maxwellian electromagnetic fields referred to in §2.1

$$\mathbf{B} = \mathbf{B}^Y \cos\theta_W \,, \tag{2.71}$$

$$\mathbf{E} = \mathbf{E}^Y \cos\theta_W \,. \tag{2.72}$$

Therefore, through electroweak mixing, hyperfields that survive until the symmetry breaking originate ordinary fields.

After the transition, the evolution of the chiral asymmetry is tracked by μ_5 and can be written as [42]

$$\partial_\tau \mu_5 = \frac{3e^2}{4\pi^2}\partial_\tau h - \Gamma_b \mu_5 \,, \tag{2.73}$$

where Γ_b is now the chirality flipping rate in the symmetrically broken region, added perturbatively. Compared to (2.37), no asymmetry source is assumed in the early Universe. Therefore, the only way we allow the asymmetry to grow, contrary to what happened in the neutron star case, is by the change of hyper-helicity, since chirality flips decrease the asymmetry.

Chirality Flipping Rate Around the Electroweak Transition

It is now necessary to determine the chirality flipping rates that will be at play and dominate in both regions in order to determine the evolution of μ_R and of μ_5.

The number of right-handed electrons can change before the EW symmetry breaking by decays into the Higgs doublet, $\varphi^{(+/0)}$ through $e_L\bar{e}_R \leftrightarrow \varphi^{(0)}$ and $\nu_{eL}\bar{e}_R \leftrightarrow \varphi^{(+)}$. The rate of inverse Higgs decay per electron is given by [125,126]

$$\Gamma_H = \frac{\pi}{192\zeta(3)} h_e^2 \left(\frac{m(T)}{T}\right)^2 , \tag{2.74}$$

where h_e is the electron Yukawa coupling. The effective Higgs mass $m(T)$ depends on the temperature and its evolution has to do with the order of the phase transition and, consequently, on the elementary particle model. The experimentally determined Higgs mass, as well as results of non-perturbative techniques, show that the electroweak symmetry breaking in the Standard Model is of higher order than second [127]. Lattice simulations provide us with the most reliable results regarding the Standard Model order and temperature of the transition, found to be a crossover at 159±1 GeV [128]. However, it is useful to have at hand an analytical estimate of the evolution of the thermal Higgs mass in order to compute (2.74), which can be obtained from the one-loop Higgs potential approximation. In the high temperature limit, the effective thermal Higgs potential reads [129,130]

$$V(\phi, T) = D(T^2 - T_0^2)\phi^2 - ET\phi^3 + \lambda\frac{\phi^4}{4} , \tag{2.75}$$

where D, λ and E are parameters determined by the details of the particle model. In the Standard Model, one has

$$D = \frac{1}{8v_0^2}\left(2m_W + m_Z^2 + 2m_t^2 + \frac{m_H^2}{2}\right) , \tag{2.76}$$

where $m_H \approx 125$ GeV and m_W, m_Z and m_t are the masses of the W boson, Z boson and top quark, respectively; $v_0 \approx 246$ GeV is the value of the scalar field at the minimum $(dV/d\phi)\,|_{\phi=v}= 0$,

$$\lambda = \left(\frac{m_H}{2v_0}\right)^2 , \tag{2.77}$$

$$E = \frac{1}{4\pi v_0^3}(2m_W^3 + m_Z^3) . \tag{2.78}$$

E is of special importance since it determines the order of the phase transition. Additionally,

$$T_0^2 = \frac{1}{4D} m_H^2 \,, \tag{2.79}$$

and $2D \approx 0.38$.

Apart from $\phi = 0$, the potential (2.75) has a minimum at a temperature T_1 given by

$$T_1 = \frac{8D\lambda T_0^2}{8D\lambda - 9E^2} \,. \tag{2.80}$$

The Higgs mass can be computed from

$$m(T)^2 = \frac{d^2 V(\phi, T)}{d\phi^2} \,|_{\phi = v} \,, \tag{2.81}$$

yielding $m(T)^2 = 2D\left(T^2 - T_0^2\right)$, which smoothly approaches zero at $T = T_0$. This is also the temperature evolution of the Higgs mass for $T > T_1$, but the Higgs mass at $T = T_1$ reaches

$$m_{T_1}^2 = 2D(T_1^2 - T_0^2) - \frac{9E^2 T_1^2}{4\lambda}. \tag{2.82}$$

For $T < T_1$, the Higgs mass follows

$$m(T)^2 = 2D(T^2 - T_0^2) - 6ETv + 3\lambda v^2, \tag{2.83}$$

with

$$v = \frac{3ET \pm \sqrt{9E^2T^2 - 8D\lambda\left(T^2 - T_0^2\right)}}{2\lambda}. \tag{2.84}$$

At the point when $T = T_0$, the Higgs mass is given by $m^2 = 9E^2T_0^2/\lambda$. This high temperature approximation is enough to estimate the Higgs thermal mass around the transition and compute (2.74), but to better determine the temperature and order of the transition, lattice simulations are used. This does not affect any of the subsequent analysis: at high temperatures, the one-loop procedure is a good approximation and at the transition, as will be shortly seen, Higgs inverse decays are already out of equilibrium. The aforementioned Standard Model parameters are going to be used in the remainder of this work.

The scattering between top quarks also intervenes in changing the number of right-handed electrons through $t_R\bar{t}_L \leftrightarrow e_R\bar{e}_L$. The rate of this process can be estimated from $\Gamma = n\sigma v$, with n the particle density, σ the cross-section of the process, which has been computed in Ref. [131], and v the velocity of the particles involved, which can be taken to be of order unity at high temperatures. This results in

$$\Gamma_{t\bar{t}} = \frac{(h_t h_e)^2 T^2}{8\pi s}\left[\frac{s^2}{(s - m_H^2)^2 + \left(\pi h_t^2 s/16\right)^2} + 2\right], \tag{2.85}$$

where s is the Mandelstam variable and h_t is the top Yukawa coupling.

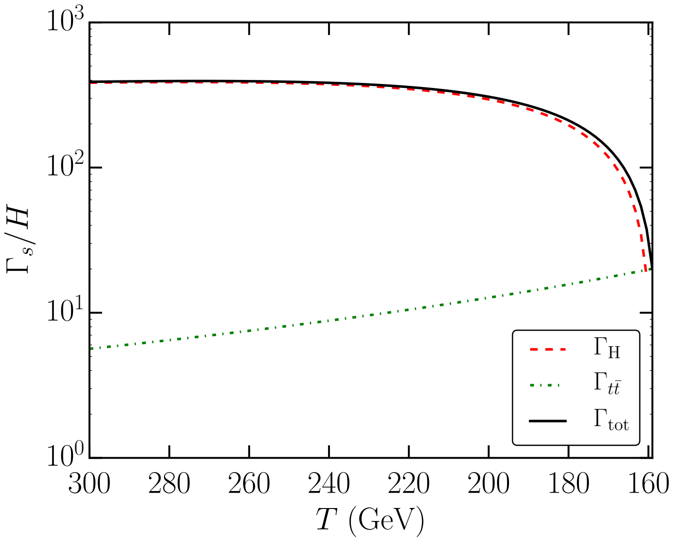

Figure 2.8: Chirality flipping rate in the symmetric phase (Γ_s) normalized to the Hubble rate due to Higgs inverse decays and $t\bar{t}$-scattering, computed from (2.74) and (2.85), respectively.

One now has the means to estimate the range of temperatures within which chirality flipping processes are important or negligible. They can be considered out of equilibrium when their rate is comparable to the Hubble parameter in the radiation dominated period, $H \simeq 1.08\sqrt{g_*/10.75}(T^2/M_{Pl})$. By requiring the critical temperature at which chirality flips get out of equilibrium in the symmetric region to be $\Gamma_{\rm tot}(T_c)/H(T_\Gamma) \approx 1$, where $\Gamma_{\rm tot} = \Gamma_H + \Gamma_{t\bar{t}}$, one finds two such critical temperatures, T_1 and T_2. For $T > T_1 \approx 2D80$ TeV, as well as for $T_0 < T < T_2 \approx 159.5$ GeV, chirality flipping processes are out of equilibrium. Thus, as the temperature diminishes and approaches $T_0 \approx 159\,$GeV, chirality-flipping processes become less significant.

The chirality flipping rates (2.74) and (2.85) are depicted in Fig. 2.8, as well as the total rate $\Gamma_{\rm tot}$. For higher temperatures, the rate of the inverse Higgs decay dominates, while the reaction rate of $t\bar{t}$ processes begins to dominate at lower temperatures, as pointed out in Ref. [131]. This occurs when the values of $m(T)/T$ are lower and only after the Higgs inverse decay rate is of the order of the Hubble rate. As a consequence, the scattering rate has a negligible contribution to the anomalous MHD equations.

The electroweak symmetry is broken around T_0, and with it come different chirality flipping processes, now associated to the weak and electromagnetic interactions separately. By scaling the interaction cross-sections with temperature, weak scatterings approximately yield a rate

$$\Gamma_{\rm w} \approx G_F^2 T^4 \left(\frac{m_e}{3T}\right)^2 , \tag{2.86}$$

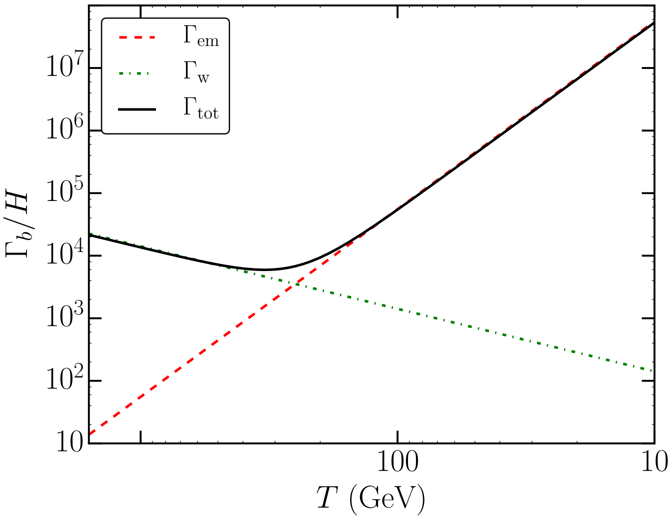

Figure 2.9: Chirality flipping rate in the symmetry broken phase (Γ_b) normalized to the Hubble rate, due to weak and electromagnetic interactions computed from (2.86) and (2.87), respectively, and their sum, $\Gamma_{\rm tot}$.

where G_F is the Fermi constant. Electromagnetic scatterings give [42]

$$\Gamma_{\rm em} \approx \alpha^2 \left(\frac{m_e}{3T}\right)^2 , \tag{2.87}$$

where α is the fine-structure constant.

The chirality flipping rates in the broken phase are presented in Fig. 2.9, according to (2.86) and (2.87) as well as the total rate $\Gamma_{\rm tot} = \Gamma_{\rm em} + \Gamma_{\rm w}$ – which from here on is denoted Γ_b. The previous discussion made clear that just before the electroweak transition, around $T_0 < T < T_2$, chirality flipping processes will not have a significant influence. After the transition though, electromagnetic and weak chirality flipping processes are important when compared to the Hubble rate. Hence, it is expected that the electroweak transition causes an impact in the evolution of the chiral asymmetry, not only due to the change in the coupling to the fields, but also because of the difference in magnitude that the chirality fliping rate undergoes during the transition. Weak scatterings, which have not been previously considered in the literature, are the dominating source of chirality flips shortly after the symmetry break. Including these rates in the evolution equation of the asymmetry and analysing it together with the modified MHD equations will be our next task.

2.3.2 Evolution Equations

For the magnetic field evolution valid in the symmetric region, 10 TeV$> T > T_0$, from (2.67) and (2.68), one finds

$$\partial_\tau \mathbf{B}^Y = \frac{1}{\sigma_s}\nabla^2\mathbf{B}^Y - \frac{g'^2}{\pi^2}\frac{\mu_R}{\sigma_B}\nabla\times\mathbf{B}^Y\,, \tag{2.88}$$

while the magnetic field evolution in the broken region, for $T < T_0$, is given by (2.18)

$$\partial_\tau \mathbf{B} = \frac{1}{\sigma_b}\nabla^2\mathbf{B} - \frac{e^2}{8\pi^2}\frac{\mu_5}{\sigma_b}\nabla\times\mathbf{B}\,, \tag{2.89}$$

where σ_b is the conductivity after the electroweak symmetry breaking. The conductivity before the electroweak transition is expected to be reduced due to interactions between leptons, $W^\pm$ and Z^0. The difference between the obtained values is however not so not significant and one can approximate $\sigma_s \approx \cos^4\theta_W\sigma_b$ [132].

Since (2.88) and (2.89), as well as (2.66) and (2.73), have the same structure, they can be studied together introducing the following coefficients

$$\begin{aligned} c_1 = \frac{g'^2}{\pi^2\sigma_s},\ c_2 = \frac{e^2}{2\pi^2\sigma_b}\,,\\ c_3 = \frac{g'^2}{8\pi^2}\frac{783}{88},\ c_4 = \frac{3e^2}{4\pi^2}\,. \end{aligned} \tag{2.90}$$

The anomaly equations then boil down to

$$\frac{d\mu_{R,5}}{dt} = \frac{c_{3,4}}{T^2}\frac{dh^{(Y)}}{dt} - \Gamma_{s,b}\mu_{R,5}\,. \tag{2.91}$$

The chiral chemical potential is continuous at the transition region since the fields crossing from the symmetric to the broken phase obey the boundary condition (2.71).

To investigate the desired anomalous MHD equations, we proceed in a manner analogous to the previous section, i.e. by Fourier transforming and decomposing the magnetic field evolution into magnetic helicity and energy spectra. That results in

$$\partial_t\rho_k^{(Y)} = -\frac{2k^2}{\sigma_{s,b}}\rho_k^{(Y)} - c_{1,2}\mu_{R,5}k^2h_k^{(Y)}\,, \tag{2.92}$$

$$\partial_t h_k^{(Y)} = -\frac{2k^2}{\sigma_{s,b}}h_k^{(Y)} - 4c_{1,2}\mu_{R,5}\rho_k^{(Y)}\,. \tag{2.93}$$

As in the last section, these equations can be solved only numerically, but useful predictions of the general behaviour of the system around the electroweak transition can be inferred from the analytical limits. For simplicity, consider the maximally helical case, i.e. $h_k^{(Y)} = 2\rho_k^{(Y)}/k$, which reduces the study of the magnetic spectral evolution (2.92) and (2.93) to only one equation. For the initial spectral distribution, take $h_k^{(Y)}(\tau) = h^{(Y)}(\tau)(k/k_{\max})^n$, for $k \le k_{\max}$, where $k_{\max}$ corresponds to the shortest length scale. Let us for now approximate this distribution to be not only the initial one but also valid in general, since for subsequent times its shape is not going to significantly change. Obviously, this is based on the assumption that magnetogenesis occurred at an epoch earlier than the studied here.

The simplest questions are related to the limits of very small (hyper-)fields and very small asymmetries. The first is realized by taking $\partial_\tau h \approx 0$, which results in an exponentially decaying anomaly

$$\mu_{R,5} \approx \mu_{R,5}^0 \exp\left(-\int \Gamma_{s,b}(\tau) d\tau\right) , \tag{2.94}$$

where $\mu_{R,5}^0$ is the initial chiral chemical potential. This is expected at temperatures lower than the electroweak transition, after spin flips dominate the evolution of μ_5 and eventually cause its exponential damping.

The latter implies the presence of strong fields in comparison with the chirality flips, i.e. $c_{3,4}\partial_\tau h^{(Y)} \gg \mu_{R,5}\Gamma_{s,b}$. This allows one to obtain $\mu_{R,5} \approx c_{3,4}h^{(Y)} + \mu_i$, where the constant μ_i depends on initial conditions. By solving (2.93) under the aforementioned approximations, the chiral chemical potential yields

$$\mu_{R,5} \approx \frac{1}{2b}\left[\tanh\left(\frac{d\tau}{2}\right) - f\right] \tag{2.95}$$

and the magnetic energy density

$$\rho_m \approx \frac{b}{2c_{1,2}c_{3,4}}\left[\mu_{R,5} - \mu_i\right] , \tag{2.96}$$

with the coefficients defined as follows

$$\begin{gathered} b = \frac{n+1}{n+2} c_{1,2} \frac{k_{\max}^{n+2} - k_{\min}^{n+2}}{k_{\max}^{n+1} - k_{\min}^{n+1}}, \quad e = \frac{2(n+1)}{(n+3)\sigma_{s,b}} \frac{k_{\max}^{n+3} - k_{\min}^{n+3}}{k_{\max}^{n+1} - k_{\min}^{n+1}}, \\ d = \sqrt{(b\mu_i - e)^2 + 4b\mu_i e}, \quad f = b\mu_i - e, \end{gathered} \tag{2.97}$$

where $k_{\min}$ corresponds to the largest length scale. This is the case when $\mu_{R,5}$ is growing by cause of being coupled to the (hyper-)magnetic field. This is expected to describe the evolution that $\mu_{R,5}$ is subject to in the vicinity of the electroweak transition. Likewise, for temperatures higher than T_1, μ_R should also be reasonably well described by this approximation, since the limit of strong fields is equivalent to negligibly small chirality flipping rates.

As exposed in §2.3.1 (and shown in Figs. 2.8 and 2.9), there is a change from negligible to relatively large chirality flipping rates when crossing the electroweak transition, which bases our expectation of observing a relatively sharp jump in μ_5 in this region due to the change from $\Gamma_s \to \Gamma_b$ in (2.91).

Before the limit (2.94) settles in for lower temperatures, it is foreseen that this regime is not instantly approached after the transition due to the spin flip rate in the broken region: as it holds a minimum (see Fig. 2.9), μ_5 is expected to present a maximum, and, therefore, to have increased in the broken region. It can be determined, from (2.86) and (2.87), that this maximum occurs at around $T(\mu_5^{\max}) \approx (\alpha/G_F)^{1/2} \sim$ GeV.

Another question worth asking is whether a certain asymmetry present for $T > T_0$ is completely damped or survives the transition. This can be estimated from knowing which initial magnetic energy is necessary to prevent a complete wash out of the chiral imbalance. Demanding $\partial_\tau \mu_R \simeq 0$ implies that $\mu_R \simeq c_3 \partial_\tau h^Y / \Gamma_s$. Integrating (2.93), that leads to

$$\begin{aligned} h^Y &\simeq \frac{\mu_R \Gamma_s}{c_3(n+1)} |k_{\text{max}}^{n+1} - k_{\text{min}}^{n+1}| \times \\ &\times \left[-\frac{2}{\sigma_s(n+3)}(k_{\text{max}}^{n+3} - k_{\text{min}}^{n+3}) - \frac{g'^2 \mu_R}{\pi^2 \sigma_s (n+2)}(k_{\text{max}}^{n+2} - k_{\text{min}}^{n+2}) \right]^{-1} , \end{aligned} \tag{2.98}$$

and, by integrating the initial distribution of ρ_k^Y, to

$$\rho_m^Y \simeq \frac{(n+1)}{2(n+2)} \frac{k_{\text{max}}^{n+2} - k_{\text{min}}^{n+2}}{k_{\text{max}}^{n+1} - k_{\text{min}}^{n+1}} h^Y . \tag{2.99}$$

Let us now consider an important point of introducing the chiral magnetic effect in MHD, namely, the generation of magnetic helicity. This can be understood by accompanying what happens if one takes an initially vanishing helicity. Despite the simple decay of the energy modes, $\rho_k = \rho_0 \exp(-2k^2\tau/\sigma_{s,b})$, the time change of helicity does not vanish by virtue of a finite μ_5. This causes the time derivative of h to grow, under the condition that μ_5 and h are of opposite sign. Therefore, helicity density is generated, and in the symmetric region it is going to be given by

$$|h_{\text{gen}}^Y| = 2c_1 \left| \int d\tau \int dk\, k^2 \mu_R(\tau) \rho_k^Y(0) e^{-\frac{2k^2\tau}{\sigma_s}} \right| . \tag{2.100}$$

Assuming no initial hyper-helicity, one expects it to fastly grow approximately in the form just derived, while the helicity term in (2.93) remains much smaller than the term containing the spectral energy density. When the first becomes comparable to the latter, this approximation breaks and it is necessary to solve the coupled energy and helicity density equations. Helicity is then likely to be closely evolving as the magnetic energy and not to portray an exponential growth as described by (2.100).

The question of whether cosmological magnetic fields are or not helical is an important one since this can shed some light in the magnetic field correlation length topic. Usually, magnetogenesis predicts primordial magnetic fields with a too small correlation length compared to what would be necessary to explain its presently observed values of up to Mpc scales [124]. For instance, unless magnetogenesis occurs during inflation, the field correlation length has to be smaller than the Hubble radius at the creation epoch. The correlation length can grow considerably after the generation of primordial magnetic fields due to an inverse cascade – in which energy is transported from smaller to larger scales – if turbulence develops in helical fields. If it naturally turns non-helical magnetic fields into helical ones, this shows how important the role of the chiral magnetic effect around the electroweak is, since it can have consequences for the correlation length.

It is also worth to mention that the production of gravitational waves strongly constraints the amplitude of primordial magnetic fields and a generated helical magnetic field yields a different gravitational wave spectrum [133]. Therefore, the helicity that seed magnetic fields might obtain due to the presence of a chiral asymmetry in the early Universe could leave an imprint that upcoming gravitational wave experiments might be able to resolve.

A complementary effect to the generation of magnetic helicity is the production of a chiral asymmetry. Similarly to the previous case, by the chiral magnetic effect, an asymmetry between left- and right- handed leptons from an initially vanishing $\mu_{R,5}$ arises, if there is a non-vanishing initial helicity. The decay of helicity leads to a non-zero change of the chiral chemical potential that can be written as

$$\mu_{R,5}^{\text{gen}} = -\frac{c_{3,4}}{\sigma_{s,b}} \int d\tau \int dk \, 2k^2 h_k^{(Y)}(\tau) \, . \tag{2.101}$$

The generation of a chiral asymmetry fueled by helical magnetic fields is important in terms of the current understanding of the particle distribution in the early Universe as it reveals the effect of different couplings between left- and right-handed particles. This can have implications for baryogenesis models, for example for scenarios that rely on helical hypermagnetic fields to produce the baryon asymmetry of the Universe [46, 47, 134].

2.3.3 Solutions of the Evolution Equations

The outlined behaviours expected for the chiral asymmetry and helicity are now going to be numerically confirmed. Let us first define the initial conditions adequate to our system. Equations (2.91), (2.92) and (2.93) are solved for a spectrum of $i = 1, 10$ modes $k_i = k_{\text{min}} 2^{i-1}$, where $k_{\text{min}}/T = 10^{-10}$. The condition $H \ll k_{min}$ is always fulfilled, guaranteeing that only length scales smaller than the Hubble length are considered. The initial temperature is chosen to be $T = 300$ GeV, which conviniently allows for the relevant features before the electroweak transition to be displayed.

As motivated in §2.3.1, in the symmetric phase the left-handed electron chemical potential is set to zero and the chiral asymmetry stored only in right-handed electrons. The initial asymmetry is arbitrarily chosen to be represented by a chemical potential of the same order of the asymmetry between baryons and antibaryons. It is set to $\mu_5^0 = 10^{-9}$ at 300 GeV, unless otherwise stated.

It is useful to define the ratio between magnetic energy density and total energy density $\Omega_{\text{mag}} = \rho_m/\rho_{\text{tot}}$, with $\rho_{\text{tot}} = \pi^2 g_* T^4/30$. Our assumption is that seed magnetic fields in the

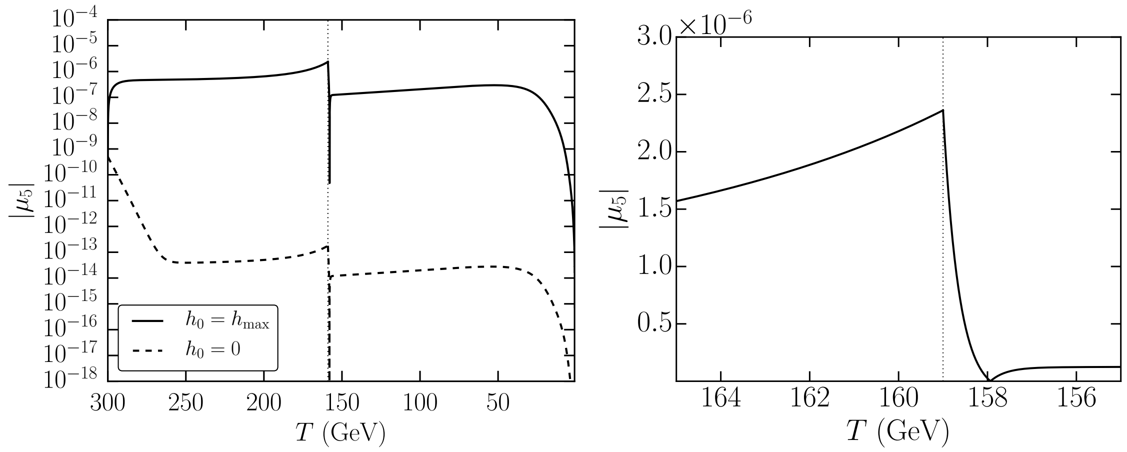

Figure 2.10: Evolution of the chiral chemical potential with temperature, before and after the electroweak transition, with $\Omega^0_{\rm mag} = 10^{-10}$, for the minimal initial helicity density $h^Y_0 = 0$ and maximal $h^Y_0 = h_{\max}$, on the left panel. Zoom around the transition region for initial maximal helicity on the right panel. Adapted from Ref. [2].

early Universe are small when compared to the total intial energy density when choosing the initial magnetic energy. The initial magnetic energy density power spectrum is taken to be $\rho^0_k/\rho_{\rm tot} = \Omega^0_{\rm mag} 5k^5/(k^5_{\max} - k^5_{\min})$, with $k_{\min} < k < k_{\max}$.

For the initial magnetic hyperhelicity, two possible limits will be considered: that of a vanishing and maximal helicity density, $h = 0$ and $h^{(Y)}_{\max}(k) = 2\rho^{(Y)}_k/k$, respectively.

Evolution of Chiral Chemical Potential

The electroweak transition in the Standard Model can indeed have a significant impact on the evolution of the electron chiral chemical potential μ_5, as can be seen from Fig. 2.10. The solution of (2.91) with temperature is there depicted, both for initially vanishing and maximal helicities. One can observe that from its initial value, $|\mu_5| = |-\mu_R/2|$ grows as the temperature approaches $T_0 \simeq 159$ GeV, caused by the falling off of the chirality flipping rate Γ_s, according to (2.74) and (2.85). The initial temperature of 300 GeV, chosen sufficiently distant from the transition, does not influence the evolution of the asymmetry.

The fast decrease in $|\mu_5|$ that takes place approximately at the transition temperature T_0 (represented by the vertical line), and which is better seen in the right-hand side of Fig. 2.10, is caused by the activation of the chirality flipping processes in the symmetry broken phase. The electron mass, gained after the transition, induces weak and electromagnetic spin flips according to (2.86) and (2.87). As predicted in the analytical analysis of the equations, $|\mu_5|$ is not immediately washed out by these interactions, but remains slowly growing until it reaches the maximum – that corresponds to the minimum of the flipping rates – in the broken region at around 40 GeV (compare with Fig. 2.9). After-

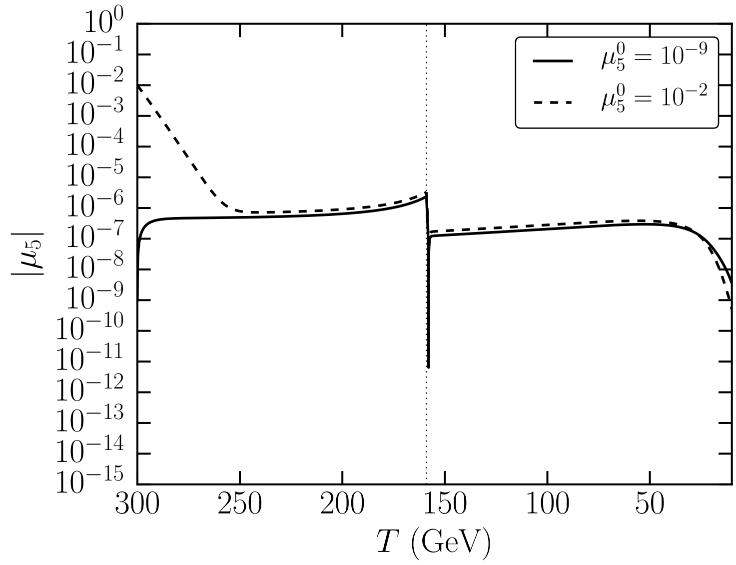

Figure 2.11: Evolution of the chiral chemical potential with temperature before and after the electroweak transition for different values of the initial asymmetry, for $\Omega^0_{\mathrm{mag}} = 10^{-10}$.

wards, as electromagnetic spin flips dominate the evolution of the chiral asymmetry, $|\mu_5|$ steeply diminishes. It enters then the regime of exponential decay described in (2.94).

The behaviours of $|\mu_5|$ and helicity were studied in the symmetry broken phase in Ref. [42] with the difference that only electromagnetic processes were accounted for in the chirality flipping rate, which did not allow for the features just discussed to occur.

The consequence of taking a specific initial helicity can be understood by comparing the solid and dashed curves of Fig. 2.10. There is a range of values of $|\mu_5|$ that spans across about 6 orders of magnitude between an initially vanishing and maximal helicity, exposing the importance that magnetic helicity has on the chiral asymmetry magnitude. The initial asymmetry value evolves more or less rapidly into a slow growing state, the magnitude of which will be dictated by the initial helicity, which can be negligible, fractional or maximal – the latter yielding the largest asymmetry values, as expected.

The impact that the initial value of the chiral asymmetry has on its subsequent evolution is shown in Fig. 2.11. It is visible that the initial μ_5 will not play a significant role in the overall dynamics of the system. The value of $|\mu_5^0|$ might be 10^{-9} or much smaller that, still, the asymmetry will fastly grow due to the term in its evolution that includes the magnetic energy. The remaining evolution is dependent on the equilibration of spin flip processes. In case $|\mu_5^0|$ is much larger than the studied values, it will take a dedicated period to decay until reaching equilibrium and then it will evolve similar to as if any other initial value would have been prescribed for the asymmetry. Therefore, the results that follow are quite independent from the initial asymmetry. This feature of the system points towards the validity of a general analysis of this kind, which does not assume any specific

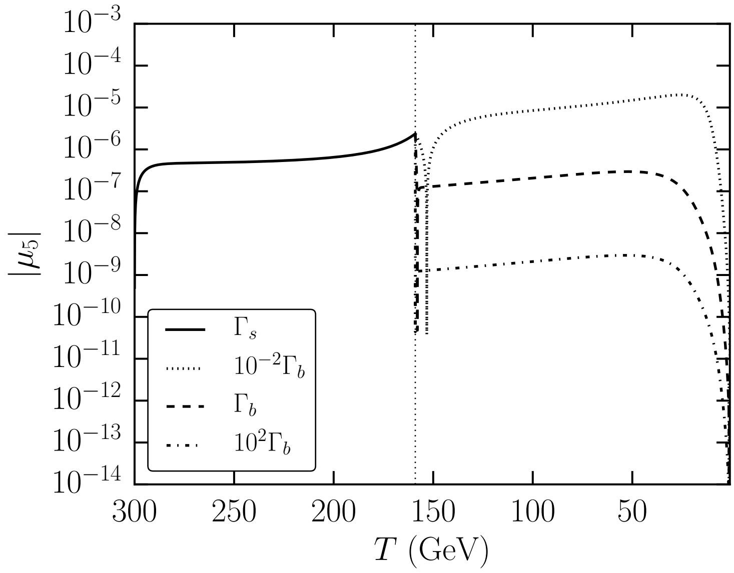

Figure 2.12: Evolution of the chiral chemical potential with temperature, for a maximal initial hyperhelicity density $h_0^Y = h_{\text{max}}$ and with $\Omega^0_{\text{mag}} = 10^{-10}$, for different modified values of chirality flipping rates in the symmetry broken phase.

particle interaction as the mechanism to create a chiral asymmetry in the early Universe.

A word now to stress that this treatment is obviously an approximation to the unavoidable non-equilibrium and complex conditions present in a symmetry breaking, even when it is of the crossover type. For instance, one can question the validity of the chirality flipping rates ((2.86) and (2.87)) shortly after the transition, because gauge bosons have just gained mass in the electroweak symmetry breaking and are still light. However, at the beginning of the broken phase, Yukawa interactions are already feeble, therefore not giving a measurable contribution to the flipping rates. To account for the uncertainty of the processes at play and to demonstrate that this analysis is qualitatively independent from the quantitative values of flipping rates right after the transition, Fig. 2.12 shows how the change of Γ_b by several orders of magnitude affects $|\mu_5|$. The general behaviour discussed for Fig. 2.10 remains, showing that it was robust under a modification of the chirality flipping rate, which justifies the previous rate as reasonable. As can be seen, in case Γ_b should be higher due to the contribution of additional flipping processes, that would reflect in a stronger damping of the asymmetry after the transition and vice-versa.

Evolution of Magnetic Energy

Along with the chirality flipping rates, a most important quantity for the evolution of $|\mu_5|$ is the initial magnetic energy, represented by the initial ratio between the magnetic and the total radiation energy densities, Ω^0_{mag}.

It is important to keep in mind that Ω^0_{mag} is significantly smaller than unity, in order

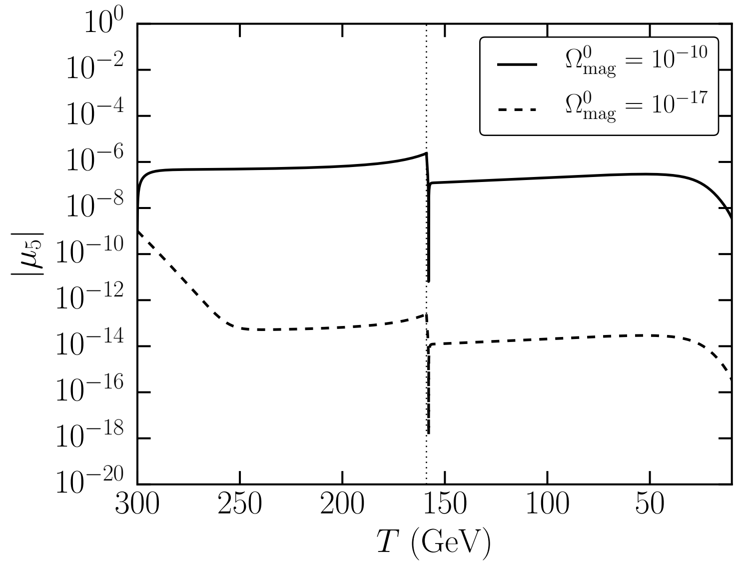

Figure 2.13: Evolution of the chiral chemical potential with temperature for maximally helical initial fields for different initial magnetic energies.

to ensure that the magnetic energy is much smaller than the radiation energy, which secures that it can also be neglected in the equations governing the expansion of the Universe. Yet, in this picture the relevant primordial magnetic fields before the transition are at least strong enough to maintain a non-vanishing μ_5. The initial energy density necessary in order to have a μ_5 that is not completely damped after symmetry breaking can be computed through (2.99). The minimal initial magnetic energy that allows the asymmetry to survive, for μ_5^0 and Γ_s at 300 GeV, is then $\Omega^0_{\rm mag} \gtrsim 10^{-15}$.

In Fig. 2.13, the chiral asymmetry evolution for two different values of the initial magnetic energy density is shown for comparison. When $\Omega^0_{\rm mag} = 10^{-10}$, the chiral asymmetry grows in the symmetric region, while when $\Omega^0_{\rm mag} = 10^{-17}$, it decays from the initial value, being quite in agreement with the analytical prediction.

The behaviour of the magnetic energy, both before and after the electroweak transition, according to the solution of (2.92), can be seen in Fig. 2.14, where the initial magnetic energy was chosen arbitrarily as $\Omega^0_{\rm mag} = 10^{-7}$. To better portray the influence of the chiral magnetic effect, in dashed the magnetic energy evolution is shown for a vanishing chiral asymmetry. This corresponds to the case of having fields whose evolution depends only on resistive damping. It is interesting to notice that a vanishing helicity produces exactly the same effect as a vanishing μ_5, once more confirming that the chiral magnetic effect is connected to the magnetic field through magnetic helicity.

First, one notes that there is no significant growth of magnetic energy around the electroweak transition in the studied scenario: even when chirality flips are negligible, this does not lead to magnetic field amplification sourced by the chiral anomaly. It is

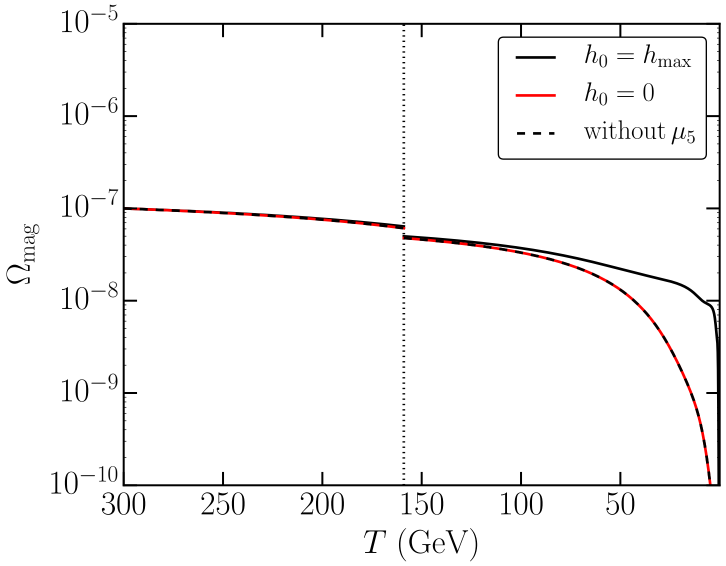

Figure 2.14: Evolution of the magnetic energy density normalized to the total energy density with respect to temperature in the presence and in the absence of a chiral asymmetry, for an initially maximal and vanishing helicity, with $\Omega^0_{\rm mag} = 10^{-7}$.

simple to see it by approximating the chirality flips to zero and considering maximally helical fields. This implies a change in hyperhelicity of $\delta h^Y = \delta\mu_R/c_3$. Inserting into it the result of the change of the asymmetry during the transition, presented in Fig. 2.10, namely $\delta|\mu_5| \sim 10^{-6}$, one obtains a negligible growth of helicity/magnetic energy.

Another way to come to the same realization is by comparing the typical magnetic field growth timescale with the electroweak transition timescale. In the maximally helical case, from the field evolution equations (2.92) or (2.93), magnetic field modes would grow at a rate $\Gamma_g \equiv g'^2 k\mu_R/(\pi^2\sigma_s)$, which corresponds to a growth timescale of $\tau_g = \Gamma_g^{-1}$. To determine it, consider that most of the energy is stored in the mode $k_5/2$, where the critical wavenumber is defined in a manner analogous to the previous section as

$$k_{R,5} = \frac{c_{1,2}\sigma_{s,b}}{2}|\mu_{R,5}|\,. \tag{2.102}$$

Estimating the transition to take place during $\delta T \approx 0.5$ GeV, the transition timescale is approximately $\tau_{\rm tr} = (\delta T)^{-1}$. For $\delta\mu_5 \sim 10^{-6}$, the relation between both timescales yields $\tau_{\rm tr}/\tau_g \simeq 10^{-3}$. This does not concede enough time for a significant magnetic field growth to be possible to occur. Hypothetically envisioning much higher initial values for the asymmetry, which are not likely to be realistic in the Standard Model framework, one would only obtain magnetic field amplification during the transition if the field would already be rather strong, as it needs to support the asymmetry in the symmetric phase. Therefore, favourable conditions for magnetic field enhancement would bring no new physical insight. In this way, we conclude that field enhancement at the electroweak symmetry breaking

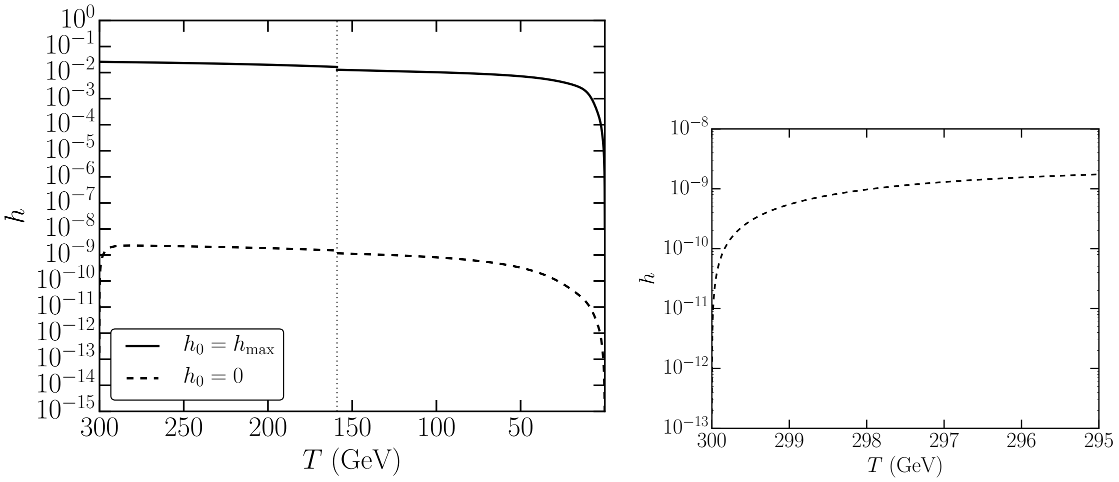

Figure 2.15: Evolution of helicity density with respect to temperature for a vanishing and maximal initial hyper-helicity, with $\Omega^0_{\mathrm{mag}} = 10^{-10}$ on the left panel. Zoom on the high temperature end of the considered region highlighting the initial growth of helicity growth for the case of $h^Y_0 = 0$ on the right panel. Adapted from Ref. [2].

stemming from the chiral magnetic effect is not probable to take place.

At last, Fig. 2.14 also serves to compare the difference between anomalous and ordinary MHD by showing the effect that the presence of the anomaly has on the energy density evolution. While there is no significant deviation from both MHD settings in the symmetric phase, one can observe that fields suffer a smaller degree of damping in the broken phase when μ_5 is added to the differential equations. Hence, while the anomaly is not negligible, it slows down the resistive damping of the magnetic energy. It steeply falls once chirality flips dominate and wash the chiral asymmetry out.

Evolution of Magnetic Helicity

The evolution of the magnetic helicity density, obtained from the solution of (2.93) before and after the electroweak symmetry breaking can be seen in Fig. 2.15. It is noteworthy that even if the seed magnetic field was non-helical, due to the chiral magnetic effect it turns helical. The production of helicity that can be better observed in the left panel of Fig. 2.15 was already predicted in the previous section and can be estimated from (2.100). An initially non-helical field turns into a fractionally helical one, showing the impact that the presence of a chiral asymmetry in the early Universe had in the cosmic magnetic field evolution. A maximally helical field will remain so during the electroweak transition and will yield a larger value for $|\mu_5|$ than the initially non-helical field. This is so due to the interplay that exists between the helicity and the chirality flipping term in the evolution of the chiral asymmetry: if helicity is higher, chirality flips will have less of an impact on its evolution.

2.3.4 Summary and Discussion

The impact of the chiral magnetic effect in the description of the early plasma that precedes and succeedes the electroweak transition has been the subject of this section. That implied modifying the MHD equations suitably, computing the rates of the processes that alter the number of chiral particles, predicting and confirming the evolution of the chiral asymmetry (through the chiral chemical potential) and of the magnetic energy and helicity densities.

One of the assumptions taken throughout this section was the presence of (hyper)magnetic fields since the earliest considered temperature (T_1). This implies that magnetogenesis is taken to have occurred previously and this approach is independent of the model preferred to describe primordial magnetic field creation. It was assumed that the velocity field is small when compared to the other terms regulating the evolution of the magnetic field in (2.88) and, therefore, turbulence effects were neglected. The reader is directed to Ref. [68] for a generalization of this condition and to the next section for an account of the possible implications it has for the results shown. It was also assumed that the chiral imbalance in the symmetric phase was stored in right-handed electrons, allowing for $\mu_L = 0$, following Ref. [118].

With the results from §2.3.3, several conclusions related to the importance of phase transitions for primordial magnetic fields can be derived. If the electroweak transition would be of the first order, which is ruled out in the Standard Model, but possible in some of its extensions such as the Minimal Supersymmetric Standard Model, bubble collisions would be likely to create MHD turbulence. This in turn is a good ingredient for the generation of primordial magnetic fields. In higher order transitions, one can analyse which conditions could lead to magnetic field amplification. This case was studied by taking into account the effects of a chiral asymmetry that through the chiral magnetic effect is linked to the evolution of magnetic fields. For typical early Universe conditions, our results expect that magnetic fields will incur no amplification in the Standard Model electroweak symmetry breaking as a result of the chiral magnetic effect.

Nonetheless, MHD gets modified by the inclusion of a non-vanishing $\mu_{R,5}$, which has consequences for the field's evolution. The most important one being the production of helical magnetic fields, even from an initially non-helical field. The magnetic field correlation length in the helical case can be larger than predicted in its absence. Helicity generation is thus important to consider. A finite chiral asymmetry has also implications for the magnetic energy, since the resistive damping after the transition will be slowed down by the presence of a μ_5.

As an additional result of the convertion of a chiral asymmetry into magnetic helicity and vice versa, a finite μ_5 will build up from a primordially helical magnetic field, even if there was no initial chiral asymmetry. The chiral asymmetry evolution is relevant not only for the MHD description but also in itself. Several baryogenesis models rely on the knowledge of the number of right- and left-handed particles in the symmetric region and at the transition.

Let us discuss this consequence of the chiral magnetic effect in more detail. If the baryon asymmetry of the Universe would have been generated by primordial maximally helical magnetic fields, studies show that fields with coherence length $10^{-2} \sim 10^{-3}$ pc and strength $10^{-16} \sim 10^{-17}$ G could have been obtained [46, 47]. What role can the analysed chiral asymmetry have here? With the asymmetry's aid, the conversion of the hypermagnetic field to electromagnetic field can affect the relic baryon asymmetry. Electroweak sphalerons violate baryon number in the left-chiral fermions, while spin flips bring this violation to right-chiral fermions. If electroweak sphalerons freeze out after the fields have completely converted into Maxwellian fields, the previous baryon asymmetry is probably erased. This would be avoided if the electroweak transition is a first orde phase transition. As it has been recently shown in Ref. [134], even as a crossover with no (B-L) violation, this conversion is not complete. Even with electroweak sphalerons in thermal equilibrium (their freeze out temperature is around 130 GeV), electromagnetic fields source chirality in a way that prevents baryon-number violation to be brought from left- to right-chiral fermions.

In quantitative terms, considering that the magnetic field at 300 GeV is 10^{-10} times smaller than the total energy density and that the chiral asymmetry at this temperature is of the order of 10^{-9}, the typical μ_5 values around the transition are about 10^{-6} for a maximally helical primordial field and are of the order of 10^{-14} for a vanishing initial helicity. These results are not very sensitive to the initial value of the asymmetry nor to the initial temperature. However, they do depend on the initial helicity and on whether the initial magnetic energy is larger than 10^{-15} times the total energy. Otherwise, the asymmetry decays before the symmetry breaking takes place.

Qualitatively, the processes that induce chirality flips determine, together with the field evolution, the features present in the chiral asymmetry: the characteristic growth right before the transition as Higgs inverse decays get out of equilibrium; the accentuated decrease due to the change of chirality flipping processes at the symmetry breaking; the maximum of μ_5 characterized by the weak processes beginning to dominate the spin flip rate; and, finally, the exponential decay of μ_5.

By the impact they have on μ_5, they also affect the field evolution. This occurs at the epoch of helicity growth and energy decay, when chirality flips dominate the evolution of the asymmetry. That causes, in the first case, a growth and, in the second case, a more accentuated exponential decay when compared to ordinary MHD decay. Resistive damping has been delayed until chirality flipping processes wash out the chiral imbalance.

This has shown the importance of taking into account the anomaly effect in the MHD equations in the early Universe and that the chiral magnetic effect is likely not causing any primordial field amplification at the electroweak transition.

2.4 On the Role of Turbulence in Anomalous Magnetohydrodynamics

Working on the frame of rest of plasma, which was assumed in the results presented in this chapter from (2.23) on, is valid as long as the velocity field is smooth when compared to the instability length scale. Let us assess the limits up to which this approximation holds for the explored systems. That can be estimated in a rough way by comparing the importance of the chiral magnetic effect, included in the MHD equation through the anomalous current, with turbulence effects, included through the velocity field. If the velocity field is described by a spectrum

$$\langle \mathbf{v}^2(T,k) \rangle = \mathbf{v}_i^2(T) \left[\frac{k}{k_i(T)} \right]^n , \tag{2.103}$$

where k_i is the inertial wavenumber and n the power index, the velocity flow can be written as a function of the length scale $\ell = 2\pi/k$

$$\mathbf{v}_\ell = \mathbf{v}_{\mathrm{rms}} \left(\frac{\ell}{L} \right)^{n/2} , \tag{2.104}$$

where L the integral length scale and $\mathbf{v}_{\mathrm{rms}} = \sqrt{\langle \boldsymbol{v}^2(T,k) \rangle}$ is the root-mean-square velocity. The velocity and anomalous terms of (2.18) scale with ℓ as

$$\begin{aligned} \boldsymbol{\nabla} \times (\mathbf{v} \times \mathbf{B}) &\sim \frac{vB}{\ell} , \\ \eta \frac{g^2}{2\pi^2} \mu_5 \nabla \times \mathbf{B} &\sim \frac{\eta g^2 \mu_5 B}{\ell} , \end{aligned} \tag{2.105}$$

which allows one to estimate the importance relative to each other through

$$\frac{\nabla \times (\mathbf{v} \times \mathbf{B})}{g^2/(2\pi^2\sigma)\mu_5 \nabla \times \mathbf{B}} \sim 2\sigma L v_{\mathrm{rms}} \left[\left(\frac{g}{\pi} \right)^2 L \mu_5 \right]^{-(n/2+1)} , \tag{2.106}$$

where the relevant scale for the CME was taken to be $\ell = 2\pi/k_5 = (\pi/g)^2 |\mu_5|^{-1}$. Whether neglecting velocity was a good approximation or not depends therefore on the spectral index and v_{rms}.

For the interior of a protoneutron star, a quantitative estimation of (2.106) can be obtained, for example, considering a temperature of $T = 40$ MeV, which, from (2.41), corresponds to a conductivity of $\sigma \simeq 0.21$ GeV and whose equilibrium chiral chemical potential is 2×10^{-3} MeV. After the initial hot phase, the scale that will concentrate most energy is of the order of $L \sim$ km. In this way, for a Kolmogorov velocity spectrum, i.e. $n = 2/3$, one concludes that in order for the CME to dominate with respect to turbulence effects, the condition $v_{\mathrm{rms}} \gtrsim 3 \times 10^{-3}$ must be met. For an upper limit on the fluid velocity, one can take 4×10^8 cm/s [99], which yields $v_{\rm rms} \simeq 10^{-2}$ and shows that for Kolmogorov turbulence, one should not neglect the role of the velocity field. A lower limit on the fluid velocity can be given by considering 10^5 cm/s [135], which translates to $v_{\rm rms} \simeq 3\times10^{-6}$ and where one is safely in the range dominated by the CME in case of Kolmogorov turbulence.

Around the electroweak transition, the conductivity is $\sigma \approx 70T$ and the Hubble parameter $H \simeq 10^{-17}T$. A measure of the integral scale is going to be given by $L = v_{\rm rms}/H$ and, therefore, (2.106) assuming a Kolmogorov turbulence spectrum the chiral anomaly term dominates for $\mu_5/T \gtrsim v_{\rm rms}^{1/2}$. As an upper limit, one can consider the velocity fluctuations that could have been caused by primordial density perturbations, obtaining $v_{\rm rms} \sim 5 \times 10^{-5}$ [136]. This implies that this study applies safely for $\mu_5 \gtrsim 10^{-2}T$ in the case of turbulence originated by such density perturbations.

A detailed analysis of the general interplay between turbulence and the chiral anomaly is found in Ref. [68]. Other recent works have as well begun considering this hypothesis, both in the context of magnetars [137] and of the early Universe [90].

Let us qualitatively predict the extent to which the inclusion of turbulence could change the discussion of results presented in §2.2.4 and §2.3.4. The potential that turbulence brings to the evolution of the field lies on the fact that it can lead to an inverse cascade in freely decaying turbulent MHD [138], as mentioned before. The prominence of the chiral anomaly with respect to the velocity field in the evolution of the magnetic field, as estimated through (2.106), will depend on the processes regulating the chiral asymmetry and on the velocity field evolution. The comparison between the chirality flipping rate and the rate at which the asymmetry is generated is a reasonably good measure to determine whether the CME will play a role in the presence of turbulence or not. A system where both effects are taken into account will tend to evolve in the direction of either (I) being dominated by the CME or (II) being dominated by the turbulent spectrum. This is expected to be so because the connection between the chiral asymmetry and the magnetic field is based on the change of helicity in the system, while, on the other hand, the most interesting case of MHD turbulence, i.e. when it leads to an inverse cascade, relies on the conservation of helicity. To counter this antagonism, the system will preferentially evolve into being dominated by one of the regimes.

From the scaling of the chiral asymmetry with time, as put forward in (2.62), it is simple to obtain the magnetic energy evolution in the regime (I)

$$\rho_m \sim \left(\frac{t}{t_{\rm damp}}\right)^{-1/2}, \tag{2.107}$$

where (2.89) was used. In freely decaying MHD turbulence in presence of helicity, which is expected to be approximate to what one finds on regime (II), the initial spectral shape in principle would not be significantly affected by the CME. From the energy transfer rate, the magnetic field is found in Ref. [120] to follow

$$\rho_m \simeq \rho_m^0 \left(\frac{t}{t_0}\right)^{-2/3} , \tag{2.108}$$

where $t_0 = L_0 E_0^{-1/2}$ denotes the relaxation time at the L_0 length scale. The topic of MHD simulations is however one where different numerical approaches might yield different results while studying the similar systems. There are in fact other simulations that found a scaling $\rho_m \sim t^{-1/2}$ in turbulent MHD in the presence of conserved helicity [139]. If this would be the case, then although the phenomena at the core of (I) and (II) have very different natures, they might yield a similar scaling of the magnetic energy with time. It becomes therefore clear that an understanding of the interplay between the CME and turbulent MHD should come from solving the magnetohydrodynamical equations including both effects. What is foremost expected to change by the addition of the CME to the typical turbulent MHD picture? That it is not necessarily the case that non-helical fields evolve and decay remaining non-helical. As concluded through (2.100), a finite helicity is produced when a chiral asymmetry is present. In its turn, the evolution of helical and non-helical magnetic fields is typically going to be different.

Chapter 3

Cosmological Imprint of Cosmic Rays

In Astroparticle Physics, cosmic rays are one of the messenger particles that have been more extensively studied. Observed for the first time unambiguously more than a century ago, through atmospheric balloons carrying electroscopes devised by Victor Hess [140], it was later realized that the extraterrestrial radiation was composed of different particles [141]. The observation techniques have greatly evolved since then, to even dedicated observatories of thousands of square kilometers [142]. Also varied is the energy range in which these particles have been detected, up to extremely high values (of the order of 10^{20} eV) [143]. These properties can be linked to the richness of processes involved in the origin and propagation of cosmic rays [144]. Their study can inform us of the particle physics interactions that take place in the cosmos. Such processes obviously depend on the nature of structures and objects present in the galaxy and much beyond. In this way, we can probe astrophysical and cosmological features – and their evolution – by studying cosmic rays.

These particles, when charged, have a clear relation to magnetic fields, since their propagation will be dictated by details of the fields that they are embedded in or traverse in their trajectory. However, it is usual for the magnetic field structure to be quite uncertain and, therefore, to limit our knowlege about the transport phenomena to which cosmic rays are subject. In this chapter, cosmic rays will be under analysis. The interesting question to address will be of a cosmological nature, having a phenomenological consequence: have cosmic rays heated up the intergalactic medium before reionization?

This question arises when contemplating the dynamics of the reionization of the Universe. The interest in this phenomenon is now renewed at the verge of obtaining unprecedent observations of that epoch through the redshifted neutral Hydrogen 21-cm line signal. The reionization of the Universe remains unknown in detail despite its high importance for the understanding of the evolution of the cosmos and, therefore, this is presently one of the primary goals of cosmology [145–148]. The 21-cm line signal will hopefully enlighten the Dark Ages by probing the efficiency of gas heating and ionization mechanisms that contributed from recombination until the first sources of light appeared. The presently consensual view is that the first galaxies and stars are the main sources of the ionizing ultra-violet (UV) radiation [149].

Note, however, that it is likely for sources of higher energy, such as X-ray photons, to also have been present. Since the mean free path of X-rays is significantly larger than the one of lower energy UV photons, the first photons can travel into the neutral intergalactic medium (IGM) far larger distances than the latter – and possibly release there their energy, inducing an increase of the temperature of the intergalactic gas. This hypothesis has been explored, but the shortcoming of having a poor knowledge about the X-ray sources at that time make it difficult to draw solid, model independent predictions for this phenomenon.

Not only X-ray photons, but also cosmic rays (CRs) could have travelled through the medium, accelerated via shocks originated by supernovae explosions, and deposited energy in the gas, contributing to its heating [150,151]. It is well established that low-energy CRs regulate the ionization and thermal state of the interstellar gas in the galactic environment, but the possibility that they have played a role in heating the IGM before reionization has but received little attention. This possible contribution to the IGM temperature was not taken into account so far when computing 21-cm signal predictions, e.g. in Ref. [152].

The proposal to be explored in the next pages can be phrased as how the propagation of CRs generated through supernovae explosions of the earliest stars might have impacted the thermal history of the IGM. By analysing the interaction between CRs and the IGM – mainly photoionization of H and He and Coulomb collisions with free electrons – one can obtain the expected deposition of thermal energy in the gas and identify whether this had a significant role on the Epoch of Reionization.

Previous studies related to the impact of CRs on the high-redshift IGM have been mainly focused on cosmological CRs originated by Pop III stars [153]. The present work, on the other hand, focuses on the role played by CRs from high-redshift Pop II stars, as motivated below. More recently, it was found in Ref. [151] that before the standard heating sources are active, such as galaxies and quasars, low-energy CRs ($E \lesssim 30$ MeV) could have increased the temperature of the IGM by 10-100 K. Following a different approach, this claim is here confirmed and expanded.

To that end, a simple reionization model that reproduces the main observed features is derived for the sake of self-consistency of the analysis. Alongside, other ingredients necessary to compute the temperature increment of the IGM due to CRs before reionization are studied, such as energy losses and propagation details. Additionally, the first limits on the spatial dependence of the obtained temperature increment are considered. In this hapter cgs and comoving units are used, unless explicitly stated otherwise.

3.1 The Epoch of Reionization

In the standard cosmological picture, the earliest stars were crucial in determining the evolution of the structures of the cosmos and are responsible for many of the details of its present form. They were essential to produce the heavier elements that, after being dispersed, enabled the birth of solar systems. After their collapse, it is generally admitted that some formed supermassive black holes and became the center of galaxies. Another essential feature, which will be our focus in this section, was that their light ionized the surrounding gas and, eventually, the whole Universe, giving rise to an important phase transition in which the atomic matter content, composed at that time by Hydrogen and Helium, passed from the neutral to the ionized state. The name reionization points to the fact that the Universe has been in an ionized state in the past. This occurred when the background temperature was too high for nuclei to be able to capture electrons and form stable neutral atoms. With the expansion and cooling down of the Universe, the density of free electrons decreased too much for thermal equilibrium between electrons and photons (and neutrinos) to continue being maintained. It was given the name of recombination to the decoupling between radiation and matter that followed this epoch of first ionization. The relatively cold and neutral times between recombination and reionization are appropriately called Dark Ages. They ended when the formation of large structures allowed stars to form and their radiation, particularly UV, warmed up and ionized the Universe again, to the state we now measure.

3.1.1 The Importance of the 21-cm Line Signal

Reionization is thought to have been completed by a redshift $z \sim 5.7$, according to measurements of high redshift quasar absorption lines [154]. It is not straightforward to use the most recent data of CMB polarization from PLANCK [155] on the free electron scattering optical depth to obtain a reliable reionization redshift (z_r) or range of redshifts between which reionization occurred, since it depends on details of the reionization history. Models of instantaneous reionization point to an extremely fast transition $7.8 < z_r < 8.8$, during at most $\Delta z < 2.8$, or less than 400 Myr [156].

It is clear that further measurements are necessary to unveil the dynamics of the Dark Ages and of the reionization history. Such is partially the aim of upcoming observations of the redshifted neutral Hydrogen (HI) 21-cm line [157–160] from a number of experiments counting on low-frequency radio interferometers, among which the *Giant Meterwave Radio Telescope* (GMRT),[1] the *LOw Frequency ARray* (LOFAR),[2] the *Murchison Widefield*

---

[1] `http://gmrt.ncra.tifr.res.in`

[2] `http://www.lofar.org`

Array (MWA),[3] the *Precision Array to Probe the Epoch of Reionization* (PAPER),[4] the *Hydrogen Epoch of Reionization Array* (HERA)[5] and, in the future, the *Square Kilometre Array* (SKA).[6]

The reason why the redshifted 21-cm signal is useful is because the spin temperature of HI depends on it such that any changes in it affect the signal. The differential brightness temperature, obtained from the signal, is directly proportional to the number density of HI when the spin temperature of HI is much larger than the CMB temperature. The spin temperature, in turn, depends on the kinetic temperature of the (nearly neutral) IGM.[7] This way, among others, access to the kinetic temperature of the IGM in a pre-reionized Universe will be possible, which is ideal to determine whether CRs contributed to it. Modelling this effect will be the subject of the next sections.

Observations of high-redshift galaxies indicate them as the primary reionization sources, capable of having completely reionized the Universe at $z = 6$, if a substantial fraction of the galaxy's ionizing emission escapes into the IGM [161]. This is, therefore, also the assumption that will be taken here. The task now is thus to describe the evolution of the IGM temperature and ionization from galaxies, taking into account that this description should be able to reproduce features that constraint the reionization history and have already been measured. The simplified treatment that follows allows for the IGM temperature to be traced with sufficient detail for our purposes, but more complete studies should model it more thoroughly and by means of numerical simulations, examples of which are Refs. [162–164].

3.1.2 Star Formation Rate

Having a model for how stars formed is essential to describe reionization, as stars are the main sources of ionizing radiation. Since measurements of the star formation rate are restricted to low-redshifts, these models are bound to rely on a number of hypothetical assumptions. The ones adopted in this work will be exposed in the following.

First, star formation is admitted to occur within the dark matter haloes surrounding galaxies, where most of their mass lies. The star formation rate (SFR) per unit of stellar mass and comoving volume inside a dark matter halo is assumed to be proportional to its mass, $\dot{\rho}_*(M_h) \propto M_h$ and its timescale to be simply given by free-fall, such that

$$t_{\rm ff} = \sqrt{\frac{3\pi}{32 G \rho_m}}\,, \tag{3.1}$$

---

[3] `http://www.mwatelescope.org`

[4] `http://eor.berkeley.edu`

[5] `http://reionization.org`

[6] `http://www.skatelescope.org`

[7] The reader is directed to Ref. [160] for a review on 21-cm cosmology.

where G is the gravitational constant and ρ_m is the average mass density inside the virial radius of the halo [165]. The virial radius is defined from the virial theorem, which relates the gravitational potential energy and the thermal or kinetic energy of a system. In this way, in astrophysical extended systems that are difficult to precisely atribute a size and density, such as galaxies and haloes, the virial radius and mass provide a useful quantification of these parameters.

The minimal mass above which haloes are able to form stars can be estimated making different considerations. Assuming that only Lyα cooling haloes form stars [166], it implies that stars form in haloes with a minimal mass of

$$M_{\mathrm{Ly}\alpha}(z) \sim 10^8 M_\odot \left(\frac{10}{1+z}\right)^{3/2} . \tag{3.2}$$

On the other hand, in haloes where the circular velocity at the virial radius, V_c, is smaller than a critical value, $\bar{V}_c$, star formation is expected to be quenched due to radiative feedback. This yields a condition for the minimal halo mass as a function of the critical velocity [167]

$$\bar{V}_c = 24\,\mathrm{km/s} \left(\frac{M_{\mathrm{rf}}}{10^8\,\mathrm{M}_\odot}\right)^{1/3} \left(\frac{1+z}{10}\right)^{1/2} . \tag{3.3}$$

The maximum between $M_{\mathrm{Ly}\alpha}$ and M_{rf} will then be taken as the minimal halo mass, M_{min}.

Based on these considerations, the cosmological SFR, per unit of *comoving* volume at redshift z, can be written as

$$\dot{\rho}_*(z) = f_* \frac{\Omega_b}{\Omega_m} \int_{M_{\mathrm{min}}(z)}^{\infty} dM_h \, \frac{M_h}{t_{\mathrm{ff}}(M_h)} \frac{dN}{dM_h\, dV} , \tag{3.4}$$

where f_* is the efficiency of stellar formation, Ω_m and Ω_b are the density parameters of baryonic and total matter, respectively, obtained from Ref. [155], and where $dN/(dM_h dV)$ gives the number density of haloes within the mass range $(M_h, M_h + dM_h)$.

A word on the assumption with respect to the star population considered is now called for. The first generation of stars – Pop III stars – are typically more massive than the later generated – Pop II – stars and have no metal content, since there were still no metals available in the gas at the time of formation of this population [168, 169]. The star formation history of Pop III is still very uncertain and object of much debate. Detailed cosmological hydrodynamical simulations implementing chemical feedback effects show that the cosmological SFR is dominated by Pop II/I stars at any redshift [170, 171], even despite considering that Pop III star formation could persist to low-redshifts $z \sim$ 3-4 [172]. By the end of their short lives, Pop III stars polluted the circumgalactic gas with metals and the cosmological SFR rapidly became dominated by Pop II/I stars [173, 174]. Following a burst of Pop III stars, in fact, the metallicity of the host halo raises so much that chemical feedback suppresses Pop III formation in self-enriched progenitors. Survey searches for Pop III stars in the Milky Way have yet to be successful in finding metal-free

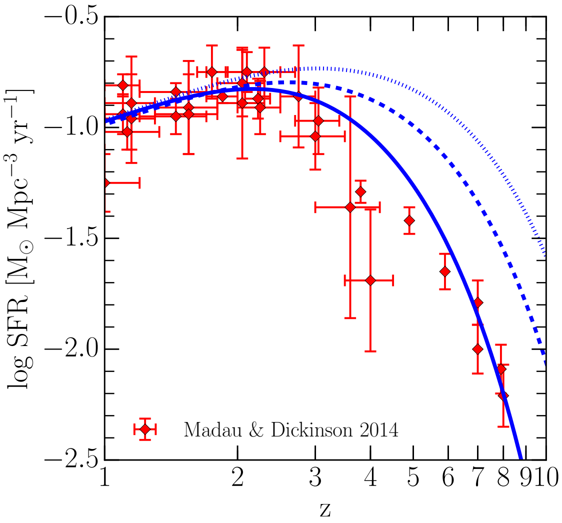

Figure 3.1: Comoving SFR according to (3.4) and comparison with the SFR measurements of Ref. [177] using different parameters $f_* = 0.02$ and $\bar{V}_c = 100$ km/s (solid curve), $f_* = 0.012$ and $\bar{V}_c = 50$ km/s (dashed curve), $f_* = 0.01$ and $\bar{V}_c = 30$ km/s (dotted curve). From Ref. [4].

stars, therefore corroborating the hypothesis that, if existing, they are quite rare [175]. On the other hand, there are observations of Pop II stars in the local Universe, which enable their properties to be constrained in a more robust manner. Since the SFR due to the Pop III is highly uncertain and, at the same time, subdominant when compared to Pop II justifies the neglection of the contribution from Pop III stars in the remainder of this analysis.

It is then necessary to find an estimate of the dark matter halo mass function to compute the expected number density of haloes. This can be done using the Press-Schechter formalism, in specific its version augmented by the Sheth-Tormen correction for ellipsoidal collapse [176].

Taking the above into consideration, one can model the SFR, in special using the help of the low-redshift measurements available to fit the free parameters of the model, namely the critical velocity and the star-forming efficiency. Figure 3.1 shows the obtained SFR for different normalizations. Values of $f_* = 0.02$ and of $\bar{V}_c = 100$ km/s reproduce the best the SFR reported in observational measurements by Ref. [177], being hence adopted from here on.

One can also obtain the SFR as a function of the halo mass. Doing so, it is noticeable that most of the contribution to the SFR is given by haloes with masses between $M_{\rm min}$ and $10^{10}M_\odot$. This will therefore be the interesting mass range.

3.1.3 Reionization History

The gas density is a crucial parameter in the understanding of the history of the reionization and its evolution is tied together to the rate at which ionization takes place. The following assumptions are meant to estimate averaged quantities in order to obtain a broad-brush picture and therefore do not take into account any spatial dependence on the distribution of matter in the Universe during this transition, but intend only at tracing general total number densities. The fraction of neutral Hydrogen with respect to the total Hydrogen will be denoted as $x_{\mathrm{HI}} = n_{\mathrm{HI}}/n_{\mathrm{H}}$ and the fraction of ionized Hydrogen (HII) as $x_{\mathrm{HII}} = n_{\mathrm{HII}}/n_{\mathrm{H}}$ with $x_{\mathrm{HI}} + x_{\mathrm{HII}} = 1$, with n_x the number density of the species x. One useful simplification is assuming equal ionization fractions for H and for singly ionized He, x_{HeII},

$$x_{\mathrm{HeII}} = x_{\mathrm{HII}} \ . \tag{3.5}$$

The evolution of the ionization fraction can be written in the form

$$\frac{dx_{\mathrm{HII}}}{dz} = \frac{dt}{dz}\left[x_{\mathrm{HI}}\Gamma_{\mathrm{HI}} - R\right] \ , \tag{3.6}$$

where Γ_{HI} is the photoionization rate and R is the recombination rate, i.e. the rate at which HII captures back an electron, turning back into HI.

To compute the photoionization rate as a function of the redshift, one recalls that only photons with an energy higher than the ionization threshold $I_H = h\nu_0 = 13.6$ eV contribute, obtaining [178]

$$\Gamma_{\mathrm{HI}}(z) = \int_{\nu_0}^{\infty} d\nu \, \lambda_{\mathrm{HI}}(z,\nu)\sigma_{\mathrm{HI}}(\nu)\dot{n}_\gamma(z,\nu) \ , \tag{3.7}$$

where $\sigma_{\mathrm{HI}}(\nu)$ is the ionization cross-section, $\lambda_{\mathrm{HI}}(z,\nu)$ is the mean free path of hydrogen ionizing photons and $\dot{n}_\gamma(z,\nu)$ is the density rate of ionizing photons. The first depends on the photon frequency according to $\sigma_{\mathrm{HI}}(\nu) = \sigma_0(\nu/\nu_0)^{-3}$, with $\sigma_0 = 6.3 \times 10^{-18}$ cm^2 [179].

The mean free path of photons that are capable to ionize HI depends on the distribution of Lyman limit absorbers (which are structures that absorb radiation that ionizes HI). Such distribution can be estimated through the column density distribution of those absorbers, N_{HI} [180]. Similarly to what is costumary in the literature (see e.g. Refs. [181, 182]), here it is assumed that the absorbers are distributed along the line of sight according to a power law given by [183]

$$\frac{\partial^2 N}{\partial N_{\mathrm{HI}} \partial z} = N_0 N_{\mathrm{HI}}^{-\delta}(1+z)^{\gamma} \ , \tag{3.8}$$

where N_0 is the normalization value. The attenuation by photoionization is represented by an effective optical depth

$$\bar{\tau}(\nu_0, z_0, z) = \int_{z_0}^{z} dz' \int_0^{\infty} dN_{\mathrm{HI}} \frac{\partial^2 N}{\partial N_{\mathrm{HI}} \partial z}(1 - e^{-\tau_\nu}) \ , \tag{3.9}$$

for Poisson-distributed absorbers, where $\tau_\nu = N_{\rm HI}\sigma_{\rm HI}(\nu)$ [184] is the Lyman continuum optical depth. Inserting (3.8) in (3.9), the integral can be solved, while in terms of the mean free path, this implies a frequency-dependency of the kind

$$\lambda_{\rm HI}(z,\nu) = \lambda_{\nu_0}(z)\left(\frac{\nu}{\nu_0}\right)^{3(\delta-1)}\,, \tag{3.10}$$

where $\lambda_{\nu_0}(z)$ depends on the size and topology of the ionized regions. Taking $\delta = 3/2$ and $\gamma = 2$, reported as fitting best the observations, it is possible to obtain an approximated analytical estimate for the mean free path. Its redshift-dependence, following the results presented in Ref. [181] for the column density distribution of Lyman-limit systems, is

$$\lambda_{\nu_0}(z) \approx 39\left(\frac{1+z}{4}\right)^{-5}\,{\rm Mpc}\,. \tag{3.11}$$

Lastly, the *proper* specific density rate of production of ionizing photons is given by

$$\dot{n}_\gamma(z,\nu) = f_{\rm esc}\frac{dN_\gamma}{dMd\nu}\,\dot{\rho}_*(z)(1+z)^3\,, \tag{3.12}$$

where $f_{\rm esc}$ is the fraction of ionizing photons that escape from galaxies and where one needs to know the specific number of photons produced per unit mass of formed stars, $dN_\gamma/(dMd\nu)$. This can be done recalling the assumption that only Pop II stars are responsible for reionization and considering that it is reasonable to assume that the stellar UV spectrum is a power law in frequency ($\propto \nu^{-\beta}$). Integrated, it yields $dN_\gamma/dM = 8.05\times10^{60}M_\odot^{-1}$ [178].

It is now possible to rewrite (3.7) in a more explicit way, namely

$$\begin{aligned}\Gamma_{\rm HI}(z) &= \left(\frac{\beta-1}{\beta+1/2}\right)\sigma_0 f_{\rm esc}\frac{dN_\gamma}{dM}\lambda_{\nu_0}(z)\dot{\rho}_*(z)(1+z)^3 \\ &\approx 5\times10^{-8}\,{\rm s}^{-1}\left(\frac{f_{\rm esc}}{10^{-2}}\right)\left(\frac{\dot{\rho}_*(z)}{M_\odot\,{\rm Mpc}^{-3}\,{\rm yr}^{-1}}\right)(1+z)^{-2}\,,\end{aligned} \tag{3.13}$$

with the spectral index $\beta = 5$ being typical for Pop II stars.

Turning now to the recombination rate, it can be written as [185]

$$\begin{aligned}R(z) &= \alpha_A(T_k^{\rm i})Cn_e(z)x_{\rm HII}(z) \\ &= \alpha_A(T_k^{\rm i})C(1+\chi_{\rm He})n_{\rm H}x_{\rm HII}^2\,,\end{aligned} \tag{3.14}$$

where α_A is the case-A recombination coefficient, C is the clumping factor, $\chi_{\rm He}$ is the cosmic helium fraction in density and the total electron number density is given by

$$n_e(z) = x_{\rm HII}(z)(1+\chi_{\rm He})n_{\rm H}(z)\ . \tag{3.15}$$

The clumping factor, which gives us a measure of the degree to which the gas of the medium is clumped, has been analysed in Ref. [186] for an extended range of redshifts and will be here approximated to a fiducial average value $C \equiv \langle n_{\rm HII}^2\rangle/\langle n_{\rm HII}\rangle^2 \approx 2$.

The kinetic temperature of the gas in the ionized regions of the IGM depends both on the processes which act in the direction of cooling it down and of heating it up. It can be expressed as [187]

$$\frac{dT_k^{\rm i}}{dz} = \left.\frac{dT_k^{\rm i}}{dz}\right|_{\rm ex} + \left.\frac{dT_k^{\rm i}}{dz}\right|_{\rm ion} + \left.\frac{dT_k^{\rm i}}{dz}\right|_{\rm ph} , \tag{3.16}$$

where the different terms denote, first, the cooling due to the expansion of the Universe

$$\left.\frac{dT_k^{\rm i}}{dz}\right|_{\rm ex} = \frac{2T_k^{\rm i}}{1+z} , \tag{3.17}$$

second, the heating due to the change in the internal energy

$$\left.\frac{dT_k^{\rm i}}{dz}\right|_{\rm ion} = -\frac{T_k^{\rm i}}{1+x_e}\frac{dx_e}{dz} , \tag{3.18}$$

with $x_e = n_e/n_H$ and which corresponds to the change in the total number of particles of the gas affected by ionizations, and, finally, the heat that gas particles gain from the surrounding radiation field

$$\left.\frac{dT_k^{\rm i}}{dz}\right|_{\rm ph} = \frac{2}{3k_B(1+x_e)}\frac{dt}{dz}\mathcal{H}_* , \tag{3.19}$$

with k_B the Boltzmann constant and $\mathcal{H}_*$ the photoheating rate per baryon. The latter can be cast in a form similar to the ionization rate (3.7), yielding

$$\mathcal{H}_*(z) = x_{\rm HI}(z)\int_{\nu_0}^{\infty} d\nu\,\lambda_{\rm HI}(z,\nu)\sigma_{\rm HI}(\nu)\dot{n}_\gamma(z,\nu)h\left(\nu-\nu_0\right) . \tag{3.20}$$

Through integrating with respect to the frequency, it can be written as

$$\begin{aligned} \mathcal{H}_*(z) &= \left(\frac{\beta-1}{\beta^2-1/4}\right) x_{\rm HI}(z)\lambda_{\nu_0}(z)\sigma_0 f_{\rm esc} h\nu_0 \frac{dN_\gamma}{dM}\dot{\rho}_*(z)(1+z)^3 \\ &\approx 3\times10^{-19}\,{\rm erg\,s^{-1}}x_{\rm HI}(z)\left(\frac{f_{\rm esc}}{10^{-2}}\right)\left(\frac{\dot{\rho}_*(z)}{M_\odot\,{\rm Mpc^{-3}\,yr^{-1}}}\right)(1+z)^{-2} . \end{aligned} \tag{3.21}$$

The escape fraction, which is left as an adjustable free parameter, can be attended to now. Analogously to the fit of f_* in §3.1.2, $f_{\rm esc}$ can be fitted such that this model is in accordance with any cosmological observations that can constraint the gas temperature. In this case, this can be realized by considering the measurements of the optical depth. And thus one requires the optical depth along the proper line element

$$\tau_e(z) = \int_0^z n_e(z')\sigma_T\frac{d\ell}{dz'}dz' , \tag{3.22}$$

where σ_T is the Thomson cross-section and $d\ell/dz = cH_0^{-1}(1+z)^{-1}[\Omega_m(1+z)^3 + \Omega_k(1+z)^2 + \Omega_\Lambda]^{-1/2}$ in a Friedmann-Lemaître-Robertson-Walker metric, to be consistent with the latest measurements.

Figure 3.2 presents the total optical depth corresponding to $f_{\rm esc} = 10^{-2}$ and its comparison to the measured value $\tau_e = 0.066 \pm 0.016$ [155] by PLANCK. By requiring that

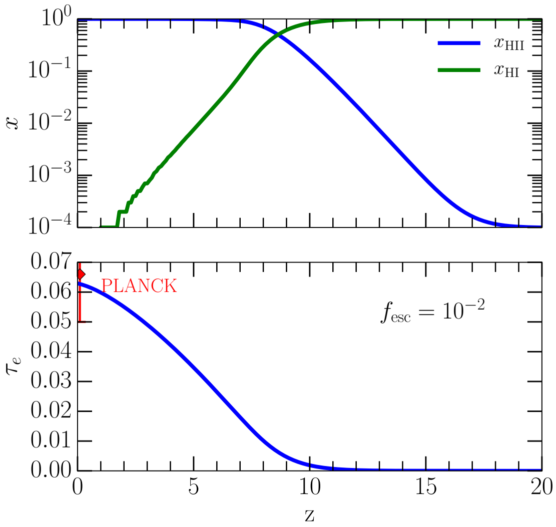

Figure 3.2: *Upper panel:* Evolution of the ionization fraction of the IGM as a function of redshift using $f_{\rm esc} = 10^{-2}$. *Bottom panel:* Total optical depth computed from (3.22) and comparison with the value measured by PLANCK [155]. From Ref. [4].

the predicted optical depth does not exceed in 3σ the observed value, one can have a more realistic reionization model. Note that actually a value of the same order was found for $f_{\rm esc}$ using a more sophisticated approach and tested against more observables in Ref. [178].

In the upper panel, the evolution of $x_{\rm HI}$ and $x_{\rm HII}$ can be seen, showing the ionization fraction decreasing for redshifts $z < 8$, and down to values of about 10^{-4} as expected for nowadays, at the same that the fraction of HII increases.

Radiation travels freely after decoupling from matter, but a Universe filled with neutral Hydrogen is not transparent to radiation of higher frequency that the ionization threshold of HI nor to its strongest transition, i.e. Lyα. Therefore, it is expected that radiation bluer than the Lyα gets absorbed by the IGM. By looking at the emission spectra of the oldest astrophysical objects, viz. quasars, one then expects to find a suppression of emission for frequencies higher than the redshifted Lyα line. However, for redshifts of about $z \lesssim 6$, radiation of frequency above the Lyα-limit begins to be detected again, which is associated to the fact that the HI content of the IGM diminished significantly and reionization took place. This effect is called Gunn-Peterson absorption trough [188]. According to Fig. 3.2, the IGM is basically fully reionized by $z \sim 6$, which is consistent with predictions drawn from Gunn-Peterson trough detections [154, 189].

In Fig. 3.3 the evolution of the temperature with redshift according to (3.16) is shown and compared with low-redshift measurements of $T \sim 10^4$ K [190], from Refs. [191–193]. One concludes that the predicted temperature of the ionized regions of the IGM after reionization, of about 10^4 K, is in good agreement with observations.

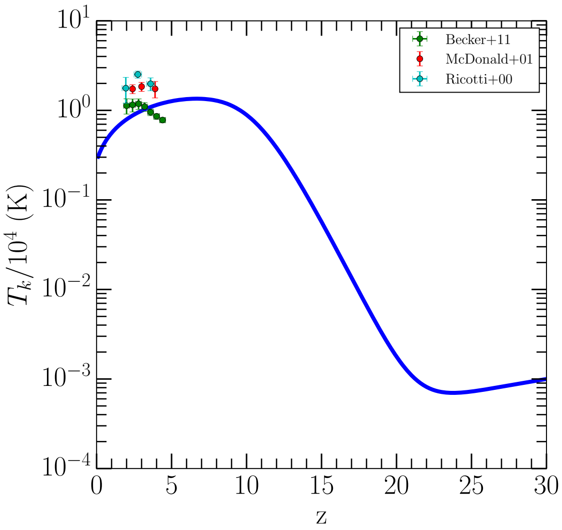

Figure 3.3: Kinetic temperature of the ionized regions of the IGM obtained from (3.16) and comparison to low-redshift measurements [190].

Therefore, this simple model catches the essence of the reionization process, at the same time matching its key observables with essentially only one free parameter. One is now ready to use the derived results in the investigation of the temperature increment to the IGM that CRs could impart.

3.2 Cosmic Rays in the Intergalactic Medium

Let us now consider the properties of CRs upon which the treatment of our problem lies. Similarly to the last section, several assumptions have to be made first in order to unfurl the processes involved, beginning, for example, by making a basic assumption on the nature of cosmological cosmic rays. Since most of the energy of CRs in the Milky Way is in protons, let us restrict to this species when considering cosmic rays henceforward. In principle, Helium nuclei should also be taken into account. It will be assumed that α-particles can for simplicity be treated as four protons, making it easy to absorb the Helium contribution in the proton spectrum.

For CRs to even begin being considered as an additional source of heat in the pre-reionized IGM, it is necessary to assess whether they get to the IGM or if they remain and lose all their energy in the interstellar medium (ISM). Taking again the analogous case of the Milky Way, one can directly infer from secondary-over-primary ratios of elements that CRs diffuse or advect out of it on timescales of about 30 Myr [194], having lost only a small percentage of energy in pion production and ionization [195]. The earlier the structures, the less confining they are expected to be when compared to present-day galaxies due to their smaller size and weaker magnetic fields. The hypothesis that CRs escape the galaxies they were produced in seems thus reasonable to admit. In fact, Refs. [196] and [153] argue that primary CRs escape from their parent galaxies on timescales short enough such that no significant energy losses occur.

Let us consider thus that CRs are accelerated by star-forming galaxies with an universal energy spectrum and that this energy will be released mostly in the IGM.

The framework used will be that of a homogeneous CR population, originated in a continuous source, that propagates in an expanding Universe subject to several energy loss mechanisms. In order to adequately but simply describe it, the classical work of Ref. [197] is generalized.

3.2.1 Production of Cosmic Rays in Early Galaxies

It is first necessary to determine the details of the CRs expected to have been sent into the circumgalactic gas.

The rate of energy injected into CR protons from early star forming galaxies is given by

$$\dot{E}_{\rm p}(z) = \epsilon E_{\rm SN} {\rm SNR}(z)(1+z)^3, \tag{3.23}$$

where $E_{\rm SN}$ is the explosion energy of the SN at the origin of CRs, ϵ is the fraction of the kinetic energy that a SN transfers into CRs and SNR is the comoving supernova rate. Considering only Type II supernovae, the average energy of an explosion that does not go into neutrinos is $E_{\rm SN} \sim 10^{51}$ erg. For the fraction of its explosion energy going into CRs, $\epsilon \sim 0.1$ is taken.

The supernova rate can be estimated allying the amount of SNe explosions to the star formation rate, which was obtained in (3.4). The number of SNe explosions that occur per solar mass of forming stars is given by

$$f_{\rm SN} = \frac{\int_8^{50} \phi(m) dm}{\int_{0.1}^{100} m\phi(m) dm} \sim 10^{-2}\, M_\odot^{-1}, \tag{3.24}$$

where $\phi(m)$ is the Initial Mass Function (IMF) of the stars. As argued in §3.1.2, the contribution from Pop III stars will be ignored and the focus will be on Pop II stars.

The IMF of the considered Pop II/I stars will be modelled as a Salpeter Mass Function [198]

$$\phi(m) \propto m^{-1+x} \exp\left(-\frac{m_c}{m}\right), \tag{3.25}$$

with the parameters $x = -1.35$ and $m_c = 0.35\ M_\odot$, and where the star mass m is allowed to be in the range $[0.1, 100]\ M_\odot$ [199].

Altogether, this allows (3.23) to be written as

$$\dot{E}_{\rm p}(z) \sim 10^{-33}\,{\rm erg\,cm^{-3}\,s^{-1}}\left(\frac{\epsilon}{0.1}\right)\left(\frac{E_{\rm SN}}{10^{51}\,{\rm erg}}\right)\times \\ \times\left(\frac{f_{\rm SN}}{10^{-2}\,M_{\odot}^{-1}}\right)\left(\frac{\dot{\rho}_{*}(z)}{M_{\odot}{\rm yr^{-1}Mpc^{-3}}}\right)(1+z)^3. \quad (3.26)$$

The CR proton spectrum from the SNe explosions is usually modelled as a power-law in momentum, since this is the spectral shape expected for particles suffering diffusive shock acceleration. The CR proton source function will then be assumed to be, averaged over volume,

$$q_p(E,z) = \frac{C(z)}{\beta(E)}\left(\frac{E^2+2Em_pc^2}{E_0^2+2E_0m_pc^2}\right)^{-\frac{\alpha}{2}}, \quad (3.27)$$

where E is the proton kinetic energy, normalized to $E_0 = 1$ GeV, m_p is the proton mass, $\beta = v/c$, α is the slope of the differential spectrum of accelerated particles and $C(z)$ is a redshift-dependent normalization. The latter is obtained by identifying the total kinetic energy rate with the SNe explosion injected energy rate (3.23), which yields

$$\dot{E}_{\rm p}(z) = \int_{E_{\rm min}}^{E_{\rm max}} Eq_p(E,z)\,dE\,. \quad (3.28)$$

The integration boundaries in (3.28) are set to $E_{\rm max} = 10^6$ GeV [200] and to $E_{\rm min} = 10$ keV, which is verified *a posteriori* to have no significant impact in the conclusions that follow. The spectral index α, known to be around 2.2, is the parameter that determines the fraction of total kinetic energy that goes into protons in the regime where $E \ll 1$ GeV in (3.27). This will be kept as the only free parameter of the model.

The source function is shown in Figure 3.4 for different values of α. Protons that have a kinetic energy below 10 MeV represent 0.5%, 2.7% and 13% of the total kinetic energy released for $\alpha = 2$, 2.2, 2.5, respectively. It is clear that α is an important parameter in determining the shape of the source function at high kinetic energies. For $\alpha > 2$, protons with kinetic energies around 1 GeV will give the largest contribution to the source function.

Once the spectral shape of $q_p(E,z)$ is fixed, the subsequent propagation of CRs in the ISM should in principle be performed. As argued at the beginning of §3.2, this study considers that primary CRs escape from parent galaxies on a timescale short enough to be considered as immediately injected in the IGM without energy losses. The confinement of CRs depends on the diffusion coefficient, which has been suggested to vary as the inverse of the square root of the density [201]. Since the efficiency of diffusion decreases with density, the earlier structures – being less dense and smaller – are expected to be less confining than the present-day galaxies. Additionally, when considering CR escape from the Galactic environment surrounding their SNe sources, the most important process is

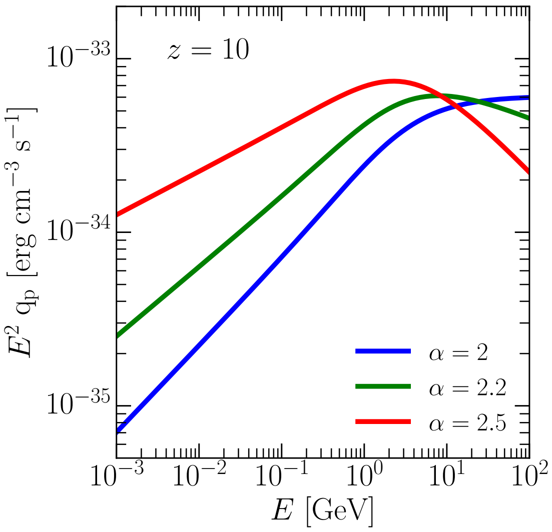

Figure 3.4: Source function of CR protons injected from SNe explosions, according to (3.27) as a function of the kinetic energy for $z = 10$ and different spectral slopes α. From Ref. [4].

advection [202], which enables even low energy cosmic rays to be carried outside of the source halo.

One last comment is directed towards the question of CR reacceleration. The assumption that cosmic rays have been ejected from SNe and into the IGM without significant diffusion nor energy losses in the galactic halo implies that whatever other phenomena present in the galactic environment did not affect them. This means that the conditions in which they were originated are directly extrapolated to the beginning of their propagation in the IGM. This implicitly means that any Fermi acceleration that might have been induced during the CR propagation in the early galactic magnetic field is neglected. One can ask for which magnetic field strengths would this effect become important. The characteristics of galactic magnetic fields in the high-redshift eras are even less known than the already uncertain knowledge possessed about them presently, but it seems inevitable that magnetic fields are not exactly static but present a random motion, which happens typically at a velocity of the order of the Alfvén speed [203]. A rough estimate can be done using

$$\frac{v_A}{\mathrm{km/s}} = \frac{B}{\mu\mathrm{G}} \left(\frac{n_{\mathrm{HII}}}{\mathrm{cm}^{-3}}\right)^{-1/2} . \tag{3.29}$$

If one assumes that reacceleration becomes non-negligible for Alfvénic velocities $v_A \gtrsim 10$ km/s, for a fiducial value of the ionized number density $n_{\mathrm{HII}} = 10^{-1}\mathrm{cm}^{-3}$, the magnetic field strength would be $B \gtrsim 3.2\,\mu$G. Since this is a significantly high value for a halo at redshifts $10 < z < 20$, it is justified to ignore this effect and assume that the energy of the CR particles was given by the SNe explosion.

This way, one can move next to treat the losses that CRs suffer once outside the ISM.

3.2.2 Energy losses in the Intergalactic Medium

Cosmic rays propagating through the IGM will interact with it and inevitably lose energy as a consequence. Especially in low density gas conditions, CRs can be an efficient heat source, as will be shown. In the case in which a CR proton ionizes an atom, a certain fraction of its kinetic energy is transferred to the electron, being subsequently used either for further atomic excitations and ionizations or distributed to other species of the medium through elastic collisions. Such collisions increase the kinetic temperature of the surrounding gas, thus, determining them is one of the aims of this study.

The ionization losses are modelled by the Bethe-Bloch equation, which in the limit $\gamma \ll m_p/m_e$ can be approximated as [204]

$$-\frac{dE}{dt}\bigg|_I = \frac{4\pi e^4}{m_e \beta c} \sum_Z Z x_{\rm HI} n_Z \left[\ln\left(\frac{2m_e c^2}{I_Z} P^2\right) - \beta^2\right] , \tag{3.30}$$

where m_e is the mass of the electron, n_Z is the number density of the element with atomic number Z, I_Z represents the ionization potentials $I_{\rm H} = 13.6$ eV and $I_{\rm He} = 24.6$ eV, and $P = p/(m_p c^2) = \sqrt{\gamma^2 - 1}$ is defined to be the dimensionless particle momentum. Obviously, protons only ionize the fraction of H and He which is neutral and this is where the ionization of the medium with redshift, studied in §3.3.1, is going to be employed.

The energy loss rate due to Coulomb collisions can be written as [205]

$$-\frac{dE}{dt}\bigg|_C = \frac{4\pi e^4 n_e}{m_e \beta c} \left[\ln\left(\frac{2m_e c^2 \beta}{\hbar \omega_{pl}} P\right) - \frac{\beta^2}{2}\right] , \tag{3.31}$$

where $\omega_{pl} = (4\pi e^2 n_e/m_e)^{1/2}$ is the plasma frequency and n_e is the number density of free electrons. The latter is also computed from the reionization model derived in §3.1.3 by assuming ionizations only due to stellar radiation. Ionizations due to CRs are negligible compared to stellar radiation ionizations, as will be clear below (in Fig. 3.7) and, therefore, insignificant to take into account when obtaining n_e.

Coulomb energy losses reflect the process in which the energy that protons lose is transferred directly into momentum of electrons in the plasma, and thus, in heating of the plasma.

Regarding inverse Compton scatterings with respect to CMB photons, these can be safely neglected, due to the fact that this process' timescale is much longer when compared to collisional processes [206].

Adiabatic energy losses, which are caused by the expansion of the Universe, are to be taken into account as [197]

$$-\frac{dE}{dt}\bigg|_a = \frac{E(E + 2m_p c^2)}{E + m_p c^2} \frac{1}{1+z} \frac{dz}{dt} . \tag{3.32}$$

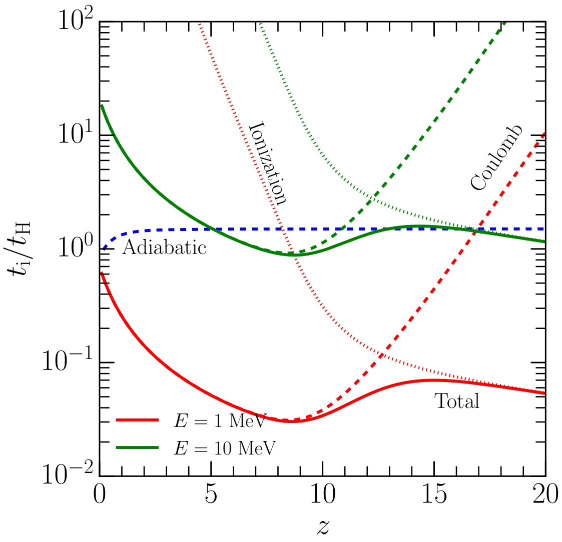

Figure 3.5: Energy loss timescale normalized to the Hubble time as a function of redshift for ionization, Coulomb and adiabatic processes according to (3.30), (3.31) and (3.32), respectively, for CR protons with kinetic energies of 1 and 10 MeV. From Ref. [4].

In order for a CR to have deposited its energy in the IGM, the energy loss timescale

$$t_i = \frac{E}{dE_i/dt}\,, \tag{3.33}$$

of each process i had to be much smaller than the Hubble time

$$t_H(z) = \int_\infty^z dz'\,\frac{dt}{dz'} \simeq \frac{2(1+z)^{-3/2}}{3H_0\Omega_m^{1/2}} \simeq 0.2\left(\frac{1+z}{21}\right)^{-3/2}\text{Gyr}\,, \tag{3.34}$$

where H_0 is the Hubble parameter, Ω_m is the density parameter of matter and where the approximation of a matter-dominated Universe has been taken again in order to obtain the simplified time evolution with redshift.

Plotting the energy loss timescale of the discussed mechanisms in Fig. 3.5, the relative importance of each of them can be analysed. For energies larger than about 10 MeV, energy losses are not efficient, since in general $t_i > t_H$ in that case. At earlier epochs, the IGM was mainly neutral and it was expected that ionization losses would dominate over Coulomb collisions, which is verified. This also points to the importance of knowing which fraction of energy lost by ionization processes is going to be converted into heating the surroundings.

3.2.3 Propagation in the Intergalactic Medium

After noticing that low-energy CR protons ($E \lesssim 10$ MeV) efficiently lose their energy in less than the Hubble time, it is now necessary to trace the number of CR protons in the IGM in order to determine the amount of heat that these can impart to the medium.

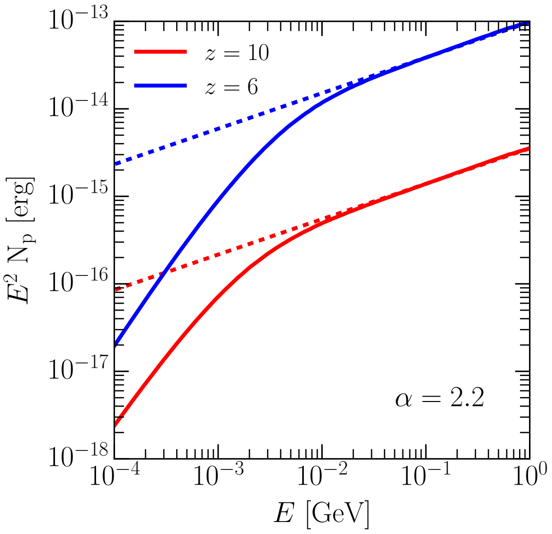

Figure 3.6: CR proton number as a function of kinetic energy for different redshifts obtained by solving (3.35) (solid curves) and comparison with its solution neglecting energy losses (dashed curves). From Ref. [4].

The evolution of the volume averaged CR proton number density, $n_p(E, z)$, is dictated by the transport equation, which can be written in the form [153, 197, 207]

$$\frac{\partial}{\partial t} N_p + \frac{\partial}{\partial E} (b N_p) + \frac{N_p}{t_D} = Q_p(E, z) \, , \tag{3.35}$$

where b is the total energy loss rate, t_D is the so-called destruction timescale and it is useful to normalize the proton number density and the source term in terms of $n_\mathrm{H}(z)$, yielding $N_p = n_p/n_H$ and $Q_p = q_p/n_H$, respectively.

In this approach, the total energy loss rate will be simply taken to be the sum of the loss processes described by (3.30), (3.31) and (3.32), namely

$$b \equiv \sum_i \frac{dE_i}{dt} \; . \tag{3.36}$$

The destruction term in (3.35) reflects the fact that interactions among protons lead CRs to lose energy in a timescale [208]

$$t_\mathrm{pp} = \frac{1}{n_b c \kappa \sigma_\mathrm{pp}} \, , \tag{3.37}$$

where $\kappa \approx 0.45$ is the inelasticity coefficient, n_b is the baryonic number density and $\sigma_\mathrm{pp} \approx 35$ mb is the proton-proton interaction total inelastic cross-section. Computing it, $t_\mathrm{pp} \approx 10^9 (1 + z)^3$ Gyr, which clearly shows that this process can be safely neglected in the following.

Since (3.35) is not solvable analytically, it is necessary to resort to numerics. The Crank-Nicolson implicit method, described in Ref. [209], can be used to solve the transport equation. The results are visible in Fig. 3.6. The redshift evolution of the proton spectrum, with and without the inclusion of the energy loss term, can be seen and it is confirmed that indeed for low energies ($E \lesssim 10$ MeV), energy losses change it significantly. This is in accord to what was concluded from Fig. 3.5.

3.3 Ionization and Heating of the Intergalactic Medium

The question that motivates this section is the determination of how much of the energy that CRs lose during propagation can contribute to heat up or reionize the IGM.

When a CR proton ionizes an atom, energy is transferred to the ejected electron as kinetic energy. Some of the energy budget of the ejected electron can go into a new ionization, some into excitations and some directly into heating by elastically colliding with thermal electrons from the background, and – at energies lower than the lowest H excitation energy – with neutral atoms.

Note that He ionization and excitation will be here discarded for the sake of simplicity.

The primary ionization rate of H by CR protons can be written as [210]

$$\Gamma_{\rm ion}^{\rm CR} = \frac{1}{W_H} \int_{E_{\rm min}}^{\infty} \left|\frac{dE}{dt}\right|_{\rm I} n_p(E) dE, \tag{3.38}$$

where $W_{\rm H} \simeq 36.3$ eV is the mean energy that a CR proton spends for an ion pair to be created.

The secondary and eventual higher generation ionizations are accounted for in a simple way, where the primary ionization rate gets multiplied by a factor $\xi(x_e)$, as developed in Ref. [211]. In order to model it, a linear interpolation between the extreme cases $\xi(1) = 1$ and $\xi(0) = 5/3$ is used in this work, such that

$$\xi(x_e) = \frac{5}{3} - \frac{2}{3} x_e. \tag{3.39}$$

The contribution that secondary electrons from ionization give to heating, depending on the energy of the electron, can be divided in three categories: (I) for $E > I_{\rm H}$ further ionization or excitation of H I can take place; (II) for $3\,I_{\rm H}/4 < E < I_{\rm H}$ Coulomb and excitation collisions can cause the electron to lose energy; and (III) for $E < 3\,I_{\rm H}/4$ the electron energy is too little for other processes to be able to occur and its energy is directly converted into heating.

Concerning Coulomb interactions, we assume that all energy lost by CR protons in Coulomb collisions is directly transferred to background heat of the medium. Using (3.31), such heating rate can be expressed as

$$\mathcal{H}_{\rm C} = \int_{E_{\rm min}}^{\infty} \left|\frac{dE}{dt}\right|_{\rm C} n_p(E) dE\,. \tag{3.40}$$

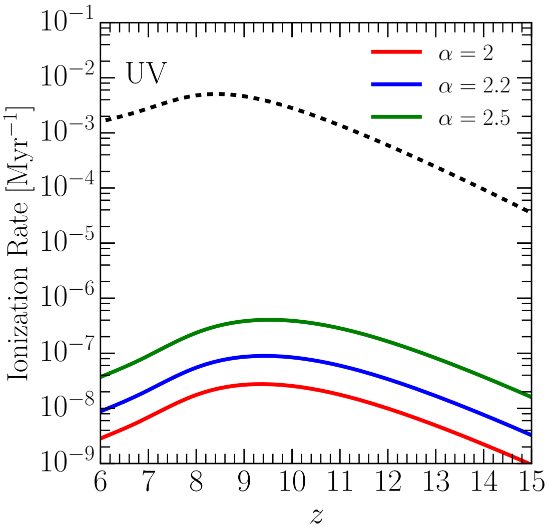

Figure 3.7: Ionization rate from CRs, according to (3.38), as a function of redshift (solid curves) for different injection slopes and comparison with the ionization rate from stellar UV photons $I_{\rm UV} = x_{\rm HI}\Gamma_{\rm HI}$ (dashed curve). From Ref. [4].

As seen above in §3.2.2, this becomes the dominating energy loss mechanism as soon as the IGM gets ionized to a sufficiently large degree.

A simple estimate including these processes is provided by Ref. [210], leading to the approximate total heating rate caused by CR protons

$$\mathcal{H}^{\rm CR} = [W_{\rm H} - \xi(x_{\rm e})I_{\rm H}]\,\Gamma^{\rm CR}_{\rm ion} + \mathcal{H}_{\rm C}\ , \tag{3.41}$$

This is the central expression in allowing one to estimate the role of CR heating. Energy losses from primary electrons via excitations were not taken into account, thus, despite this contribution being likely small, one must keep in mind that (3.41) slightly overestimates the heating rate.

In quantitative terms, (3.41) tells us that each ionization caused by CR protons leads to the transference of about $W_{\rm H} - 5/3\, I_{\rm H} \sim 13.6$ eV into the IGM.

3.3.1 Impact of Cosmic Rays on Reionization

In Figure 3.7, the CR proton ionization rate, computed from (3.38), is presented in parallel to the stellar UV radiation ionization rate, computed with (3.7). It is visible that the CR ionization rate is smaller than the UV photoionization rate by several orders of magnitude, as expected and previously considered in the literature [145, 147, 212]. It is then perfectly justified that the contribution of CRs in the description of the reionization model developed in §3.1.3 was neglected.

Let us understand the difference between the CR and UV ionization of the Universe taking a slightly different approach. In a simplified scenario, the comparison between stellar and CR emissivities can be insightful. The emissivity of ionizing photons produced in galaxies can be computed as

$$\epsilon_* = f_{\rm esc} E_\gamma f_{\rm SN} \dot{\rho}_* \,, \tag{3.42}$$

where the energy that photons carry can be written in the form

$$E_\gamma = \dot{N}_\gamma h\nu t_* \,, \tag{3.43}$$

with the rate of ionizing photons being $\dot{N}_\gamma \sim 5 \times 10^{47}$ s^{-1}, the average stellar life-time $t_* \sim 30$ Myr and $\langle h\nu \rangle \sim 2.1 \times 10^{-11}$ erg is the energy of a single photon. This implicitly assumes that the stars that dominate UV emission in galaxies are the same that explode into SN, i.e., with masses of around 10 $M_\odot$.

For cosmic rays, the emissivity is given by

$$\epsilon_{\rm CR} = f_d \epsilon E_{\rm SN} f_{\rm SN} \dot{\rho}_* \,, \tag{3.44}$$

where f_d is the fraction of energy that CRs deposit in the IGM. This corresponds to the fraction of energy of CR protons with $E \lesssim 10$ MeV, as found in §3.2.2, which implies the following energy integral

$$f(\epsilon) = \Phi_0 \int_{E_{\rm min}}^{\epsilon} dE\, E \left(\frac{p}{p_0}\right)^{-\alpha} = \Phi_0 E_0^2 \int_{E_{\rm min}/E_0}^{\epsilon} dx\, x \left(\frac{E_0 x^2 + 2m_p x}{E_0 + 2m_p}\right)^{-\alpha/2} \,, \tag{3.45}$$

where $x = E/E_0$. For $\alpha = 2.2$, it becomes $f_d = f(10\,\text{MeV})/f(10^6\,\text{GeV}) \sim 10^{-3}$. This optimistically assumes that the deposited energy would all be used in ionization.

The stellar flux is then given by $J_* = \epsilon_* \lambda_*$, where λ_* denotes the UV photon mean free path, while the flux for CRs yields $J_{\rm CR} = \epsilon_{\rm CR} \lambda_{\rm CR}$, with $\lambda_{\rm CR}$ the corresponding mean free path. The ratio between the two would be

$$\frac{J_{\rm CR}}{J_*} = \frac{\epsilon_{\rm CR}\lambda_{\rm CR}}{\epsilon_* \lambda_*} \sim 10^{-3} \frac{\lambda_{\rm CR}}{\lambda_*} \,. \tag{3.46}$$

The mean free path being approximately proportional to the timescale of energy loss, t_i, means that the ratio between the ionization rates, J_i/t_i, could be roughly 10^{-3}. Hence one concludes that under the fiducial parameters used, even assuming that CR energy would all be lost in ionization, still $J_{\rm CR} \ll J_*$. This serves to illustrate through a back-of-the-envelope-calculation why one is expecting the result shown in Fig. 3.7, in which cosmic rays did not contribute meaningfully to the reionization of the Universe.

3.3.2 Impact of Cosmic Rays on Heating

After just having convinced the reader that stellar UV photons are largely responsible for cosmological reionization, it will be shown now why there are very good reasons to be considering the influence that CRs had in the epoch of reionization as a whole. As effective as stellar UV radiation is in ionizing the IGM, the impact on its global temperature is limited to regions which are fully ionized. Compared to it, X-rays would be more relevant to consider in this context since their larger mean free path allows them to travel beyond the ionized regions. Different possible sources for X-rays at that epoch have been hypothetically considered, such as quasars, supernovae and/or early populations of relatively soft X-ray binaries [213]. If at the origin of these energetic photons are black holes, there were claims that the IGM could be heated prior to reionization up to 10^4 K [214]. The abundances, evolution and spectra of these potential sources are however highly uncertain, especially considering the high redshifts [215, 216]. In comparison, cosmic rays can be seen as a viable alternative source of heat in the neutral regions of the IGM.

The possibility that the IGM got heated by blazars of TeV energy has also been investigated [217]. It was concluded that TeV blazars at redshifts $z \lesssim 6$ can yield a heating rate higher than photoheating, especially in less dense regions of the IGM (see Fig. 9 of Ref. [217]). While this is an interesting result that should be taken into account when computing the 21-cm line signal, the analysis of the previous sections in terms of cosmic ray energy deposition are likely to result in a heat prior to the reionization epoch. Its contribution could thus be easily distinguishable from that given by TeV blazars.

After the preparations done in §3.3.1, it is now easy to compute the increment to the temperature of the IGM that CR protons produce

$$\Delta T(z) = \frac{2}{3}\frac{\mathcal{H}^{\rm CR}(z)}{k_B H(z)} \ , \tag{3.47}$$

where the Hubble parameter is again approximated to a matter-dominated Universe, $H(z) = H_0 \Omega_m^{1/2} (1+z)^{3/2}$, and the heat input given by CRs, $\mathcal{H}^{\rm CR}$, was computed in (3.41).

The temperature increase of the neutral IGM due to CRs is shown in Fig. 3.8. The CMB temperature evolves with redshift simply as $T_{\rm CMB}(z) = 2.725\,(1+z)$ K and one can compare it against the results just obtained. It is notorious that the IGM temperature can be raised up to $\sim 3 \times 10^3$ K before reionization is complete. Moreover, that would exceed the average CMB temperature at $z \lesssim 9(12)$ for $\alpha = 2(2.5)$. The implication is that, in fact, the neutral IGM is likely to be pre-heated by low-energy CRs well before being reionized.

These findings can be compared to the closest study on the topic, in particular to Fig. 1 of Ref. [151]. The results there presented also predict a temperature increment of 1-10^3 K, depending mainly on the minimum star-forming halo mass taken. In that analysis, the highest temperature increase corresponded to a minimum halo mass of $3 \times 10^5\, M_\odot$ and to a supernova explosion of $E_{\rm SN} = 10^{53}$ erg, which contributed with a fraction of 5% of its energy to low-energy CRs. That admits powerful supernova explosions from Pop III stars in low mass minihaloes that would be able to evaporate the halo and propagate

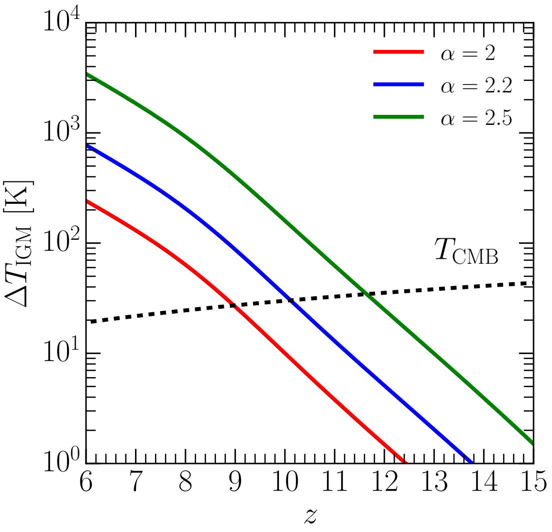

Figure 3.8: Average neutral IGM temperature increment as a function of redshift for different CR spectral slope (solid curves) and comparison with the CMB temperature at the same redshift (dashed curve). From Ref. [4].

through the IGM. On the contrary, the model developed here relies on a more standard stellar population and explosion energies, and on haloes which masses give the largest contribution to the SFR. Furthermore, it was imposed that the used SFR fits observations of star formation and that reionization is consistent with the Thomson scattering optical depth. Therefore, one notes that two complementary approaches, based on very different assumptions and using different methods, reached the conclusion that cosmic rays are likely to give an important thermal input to the IGM before reionization.

To understand the spatial distribution of the pre-heating predicted by Fig. 3.8, viz. to estimate whether it might be evenly distributed throughout the neutral medium or might be localized around the parent galaxies, it is necessary to understand the diffusion of CRs in the pre-reionized IGM. This will be superficially considered next.

3.4 Diffusion of Cosmic Rays in the Intergalactic Medium

Predicting the distribution of the additional heat caused by CRs in the IGM would be one way to inform the measurements from the 21-cm line signal of the expected morphology of the CR contribution that could in principle be probed. A more sophisticated investigation of this problem is however required. The following discussion aims only at finding the limiting cases, while a deeper analysis is encouraged.

Diffusion is a consequence of particles random-walking. As cosmic rays are injected into the IGM, they will suffer diffusion and travel a distance that is dependent upon the structure and strength of the intergalactic magnetic field. However, one is faced with the issue of not having much information on large-scale magnetic fields at such redshift.

3.4.1 Bohm Diffusion

Supposing that CRs reach the large-scale IGM, as motivated before, the slowest they can diffuse is if Bohm diffusion is assumed, which is given by one scattering per gyroradius r_L [218, 219]. The Larmor radius is

$$r_L = \frac{mv_\perp}{|q|B}, \tag{3.48}$$

where m is the particle mass, $|q| = Ze$ is its charge and $v_\perp$ the velocity perpendicular to the direction of the magnetic field B.

The Bohm diffusion coefficient for protons ($Z = 1$) as a function of momentum is [6]

$$\begin{aligned} D_B(p,z) &= \frac{1}{3} r_L c \qquad (3.49) \\ &\sim 1.1\,\mathrm{Mpc}^2\,\mathrm{Gyr}^{-1} \left(\frac{p}{\mathrm{GeV/c}}\right) \left(\frac{B_0}{10^{-16} G}\right)^{-1} \left(\frac{1+z}{21}\right)^{-2}, \end{aligned}$$

with B_0 the average magnetic field strength of the IGM at $z = 20$.

If low-energy CRs diffuse far enough to reach another halo before depositing all their energy in the IGM, the pre-heat induced by them would be rather uniform. This way, one can use the average distance between haloes, $\langle d \rangle$, as an indicator of the time needed for cosmic rays to diffuse that far. Under Bohm diffusion assumptions, the maximal diffusion timescale between haloes can then be estimated, as it is approximately given by

$$t_B \simeq \frac{\langle d \rangle^2}{D_B}\ . \tag{3.50}$$

The average *proper* distance between haloes $\langle d \rangle$ can be roughly estimated by considering them uniformly distributed, such that

$$\frac{4\pi}{3} \langle d \rangle^3 \sim \left(M_h \frac{dN}{dM_h} \right)^{-1} (1+z)^{-3}\,, \tag{3.51}$$

where dN/dM_h is the comoving halo density. To obtain it, one considers the typical halo of mass that gives the largest contribution to the star formation rate. At $z = 20$, this occurs for haloes with mass around $M_{\min}(z = 20)$ and their mean separation is $\langle d \rangle \sim 50$ kpc [220].

Assuming a value of $B_0 = 10^{-16}$ G for the strength of the IGM magnetic field at $z = 20$ following Ref. [151], the CR Bohm diffusion timescale can be computed. Using (3.50) and (3.34), one obtains $t_B \lesssim t_H$ for CR proton energies $E \gtrsim 20$ keV. If this is the slowest that CRs can diffuse, this corroborates the hypothesis that cosmic rays uniformly warm up the whole neutral IGM, as usually assumed (see, e.g. Ref. [196]).

However, standard Bohm diffusion might not be giving an adequate upper limit on the cosmic ray diffusion since CRs may have an impact on the environment that they propagate in. In other words, there is the possibility that a self-generated magnetic field stems out of plasma instabilities created by protons tranversing the intergalactic magnetic field [221].

3.4.2 Diffusion Supported by Self-Generated Magnetic Fields

In the process of escaping from the parent halo, CRs produce an electric current that induces in the background plasma a reactionary current, which in turn produces small scale instabilities. These instabilities can grow and turn into turbulent magnetic fields. Magnetic field instabilities that lead to turbulence are an interesting phenomenon that deserves a study on its own, but here the focus will be on how this effect might affect the diffusion of CRs. Turbulence in the magnetic field means that particles are subject to more scatterings, which causes the self-confinement of cosmic rays, as studied in Ref. [221].

An upper limit of the effect of self-generation of magnetic fields by cosmic rays can be derived (I) by generalizing the formalism developed by Ref. [221] for the non-relativistic regime and (II) by assuming that all CRs that escape to the IGM add up to generating the magnetic field.

First, the injection spectrum assumed throughout this chapter (see (3.27)) is rewritten as a function of the proton momentum $dN/d^3p \propto p^{-4}$, equivalent to $dN/dE \propto p^{-2}$. The differential number density of escaping CRs can be written as a function of p and of the distance from the halo, r, giving

$$f(p,r) = \frac{dN_\mathrm{p}}{dV d^3p} = A(r)\left(\frac{p}{p_0}\right)^{-4}, \tag{3.52}$$

where p_0 is the momentum normalization and the dependence on the distance from the halo is enclosed in the coefficient $A(r)$. In order to compute it, consider the total pressure that the cosmic ray source exerts on a surface $S = 4\pi r^2$, namely,

$$P_\mathrm{s} = \frac{F_\mathrm{s}}{S} \sim \frac{L_\mathrm{CR}/c}{4\pi r^2}, \tag{3.53}$$

where the second equality is obtained from relating the force exerted by the CR source F_s to the source luminosity L_CR. Such luminosity, for a typical star forming halo at $z = 20$, yields

$$\begin{aligned} L_\mathrm{CR} &= f_* f_\mathrm{SN} E_\mathrm{CR} \frac{\Omega_b}{\Omega_m}\frac{M_h}{t_\mathrm{ff}} \\ &\sim 10^{38}\,\mathrm{erg\ s^{-1}}. \end{aligned} \tag{3.54}$$

In parallel, the pressure exercised by cosmic rays can be roughly estimated as

$$P_\mathrm{CR} \sim \int_{p_\mathrm{min}}^{p_\mathrm{max}} dp\, p^3 v(p) f(p,r)\,. \tag{3.55}$$

By requiring the source pressure and the CR pressure to be equal at the same distance, one obtains $A(r)$. Thus, from (3.53) and (3.55), one has

$$A(r) = \frac{L_{\rm CR}}{4\pi r^2 c}\left[\int_{p_{\rm min}}^{p_{\rm max}} dp\, p^3 v(p)\left(\frac{p}{p_0}\right)^{-4}\right]^{-1} . \tag{3.56}$$

One can now determine the current induced by cosmic rays streaming away from the source through

$$\begin{aligned} j_{CR}(p) &= e\int_p^{p_{\rm max}} 4\pi p^2 dp\, v(p) f(p,r) & (3.57)\\ &\sim \frac{eL_{\rm CR}}{cr^2 p_0} g(p/p_0)\,,\ \text{with } g(x) = \frac{\int_x^{x_{\rm max}} dx \beta(xp_0)x^{-2}}{\int_{x_{\rm min}}^{x_{\rm max}} dx\, \beta(xp_0)x^{-1}}\,. & (3.58)\end{aligned}$$

There are two ways in which the instability can grow, namely in the resonant regime, when the energy density of CRs is larger than the magnetic energy density, and in the non-resonant regime. The first is probably an unlikely condition to be met by the system under study (considering as relevant only low-energy cosmic rays) and therefore the non-resonant regime is assumed. In this case, the saturation of the magnetic field instability, δB, can be estimated from the current associated with the cosmic rays, (3.57), under equipartition with the magnetic energy density of the amplified field

$$\frac{\delta B_{\rm sg}^2}{8\pi} \sim \frac{L_{\rm CR}}{cr^2}\left[\frac{p}{p_0}g(p)\right]_{\rm max} \sim 0.01\frac{L_{\rm CR}}{cr^2}\,, \tag{3.59}$$

where the last approximation was taken from the fact that the function $pg(p)$ has a maximum around GeV/c, while for larger momenta it remains fairly constant.

To have a sense for the self-generated fields that can be involved, choosing a distance from the halo $r = 1$ kpc, (3.59) yields $\delta B_{\rm sg} \approx 0.01\,\mu$G.

As previously mentioned, the background medium field strength was considered to be $B_0 = 10^{-16}$ G. Thus, since $\delta B_{\rm sg} > 10^{-16}$ G, the self-generated diffusion coefficient implies a longer diffusion timescale when compared to simple Bohm diffusion. For ordinary Bohm diffusion, one concluded that there is still enough time for the cosmic ray energy to be transferred to the IGM. This might not be the case if cosmic rays Bohm diffuse through self-generated magnetic fields though. That would then yield the slowest limit posed to their propagation and it is computed next.

The diffusion timescale associated with the Bohm diffusion caused by the self-generated magnetic field is related to the corresponding mean free path at a given epoch by $\lambda_{\rm CR} = \sqrt{t_B D_B}$. The self-generated magnetic field at a distance that corresponds to the cosmic ray mean free path in this regime is computed by identifying it with the distance from the halo ($\lambda_{\rm CR} = r$). Inserting in (3.49) the self-generated magnetic field (3.59), results in a mean free path

$$\lambda_{\rm CR} = 1\,{\rm kpc}\left(\frac{t_i}{\rm Gyr}\right)\left(\frac{L_{\rm CR}}{10^{38}\,{\rm erg\ s^{-1}}}\right)^{-1/2}\left(\frac{p}{\rm GeV/c}\right) . \tag{3.60}$$

What this reveals is that, in fact, cosmic rays might be self-confined and the pre-heat of the IGM due to them could be quite clustered around the star-forming early galaxies instead of uniformly distributed in the neutral background medium.

There are, however, some points that contribute for this limit to be so strong and that would need to be taken into account in a more realistic scenario, possibly leading to an increase of the mean free path of cosmic rays. An equipartition value, obtained by the saturation of the magnetic field instability in (3.59), might never be reached if the conversion from CR kinetic energy to magnetic energy is not efficient enough. Additionally, the non-resonant regime might not be attained if the intergalactic magnetic field was too strong at those times or by means of lower cosmic ray luminosities, which would cause the ratio between magnetic and CR energy densities to be too large.

The interest in understanding CR diffusion comes not only from our thirst for its comprehension, but also because measurements of the 21-cm line signal from this epoch will soon be able to discriminate between a neutral region which was pre-heated by cosmic rays or not. If the incremental temperature given to the IGM by cosmic rays remains confined to the neighbourhood of haloes, one expects the power spectrum of such radiation to leave unique imprints, since the HI 21-cm line observations should be quite sensitive to the morphological properties of the signal.

X-rays have a mean free path given by [151]

$$\lambda_{\mathrm{X-ray}} \sim 926\,\mathrm{Mpc}\,(1+z)^{-3}\left(\frac{E}{300\,\mathrm{eV}}\right)^{3.2}, \tag{3.61}$$

which is substantially different from the cosmic ray mean free path, making it in principle also possible to distinguish between the heating source if the temperature of the neutral intergalactic regions show a pre-heat. Another motivation is the information on the high-redshift IGM magnetic fields that could be inferred from analysing the diffusion to which CR protons are subject to. This would additionally inform about details of CR acceleration by early SNe.

3.5 Summary and Discussion

This chapter studied the impact that cosmic rays can give to the temperature of the neutral intergalactic medium before reionization.

The developed reionization model is simplified enough to allow one to obtain the ionization fraction with redshift including only a modest amount of parameters. This is pivotal to improve the results of previous studies that consider x_{HII} constant when computing cosmic ray energy losses. With this model (I) the observed optical depth is reproduced; (II) the Universe is reionized in the expected redshift range; and (III) the average kinetic temperature of the ionized regions, induced by UV photons, matches low-redshift measurements.

Concretely, as fiducial values, the injection energy spectral index was varied between α =2-2.5 and the efficency of converting energy from supernovae explosions into cosmic rays was taken as $\epsilon = 0.1$. Adjusting the theoretical expressions to the experimentally observed star formation rate and optical depth, the conversion efficiency of halo mass into stars was obtained to be $f_* = 0.02$ and the fraction of photons capable to ionize that escape into the IGM $f_{\rm esc} = 10^{-2}$.

It was assumed that cosmic rays escape their host galaxies by advecting in a timescale sufficiently short to be negligible in comparison with the CR energy loss timescale. Although this is valid for protons of $E > 100$ MeV in our Galaxy, this assumption might not hold for early star-forming galaxies. This would depend on quantities that are extremely uncertain, e.g., the turbulent magnetic fields of the early haloes. From a broader, simplified perspective, the rationale that weaker magnetic fields correspond to larger diffusion coefficients and to smaller magnetic halo sizes, supports the assumption that the diffusion timescale in those objects should be smaller than in the Milky Way. The fact that a certain amount of the energy lost by CRs can first excite HI and only subsequently be converted into heat was neglected. This simplification is not expected to yield a significant modification to the results.

According to the injected CR source function, protons of around 1 GeV carry away most of the energy from the SN explosion converted into CR. However, protons suffer energy losses in relevant timescales, as already noted in Ref. [151], at much lower kinetic energies. With this in mind, cosmic rays of MeV energies, particularly below 10 MeV, are of interest. Energy losses are dominated at redshifts $z < 13$ by Coulomb scatterings and for higher redshifts by ionizations. The energy lost in Coulomb collisions is immediately available to heat the IGM. This fact explains why larger temperature increments are obtained for smaller redshifts.

When compared only to adiabatic thermal evolution, prior to reionization being complete, the temperature of the neutral IGM can be significantly increased by considering low-energy CRs. The contribution from cosmic rays with energies $E \lesssim 10$ MeV is likely to exceed the CMB temperature for $z \lesssim 10$, and probably even for higher redshifts. This would depend on the injection slope α. It can amount to about 10-200 K more than standardly predicted. Such pre-heat is expected to be measurable with 21-cm signal experiments, considering their high sensitivities. Accordingly, signal predictions and simulations that take into account this pre-heating mechanism are encouraged. Note that this temperature increment is comparable or higher than that produced by more popular alternative heating mechanisms, including dark matter annihilations [222], TeV blazars [217] and X-rays [213].

An estimate of a more conservative CR mean free path is given based on the hypothesis that CRs that escape from their haloes trigger streaming instabilities. This can lead to an amplification of the intergalactic seed magnetic field up to equipartition with the CR energy. It was found that favorable assumptions for the development of a self-generated magnetic field confine very efficiently CRs around the parent galaxy for a timescale that exceeds the Hubble time at $z \sim 20$. Under these conditions, detecting the 21-cm line signal that such a clustered or evenly distributed emission would leave, could represent the first probe of the magnitude and structure of magnetic fields in the Dark Ages.

Chapter 4

Synchrotron Emission in Dark Matter Indirect Searches

The standard cosmological picture nowadays is the ΛCDM model. It incorporates into an approximately flat Universe that has begun from the Big Bang singularity and whose evolution is governed by general relativity and, in particular, by Friedmann's equations, both a dark energy, in the form of a cosmological constant Λ, and a cold dark matter (CDM) component. Since our comprehension of the cosmos is ruled by two dark entities that have been introduced in order that standard cosmology matches astrophysical observations, where "dark" refers to the fact that they are non-absorbing and non-luminous, there is a tremendous interest in understanding their nature and properties.

Dark matter was postulated in the thirties when astronomers could not reconcile the mass of the Milky Way, obtained through observations of the visible stars, with the amount of mass required for stars to rotate around our galaxy [223]. Soon afterwards, the same was observed at a much larger scale: the Coma Cluster observed mass would not be sufficient to explain the rotation of its galaxies [224]. The idea that there was a missing mass component was then born, and enforced through subsequent studies of galaxy rotation curves (orbital velocity of an emitter as a function of its distance to the center of the galaxy), which did not decrease with distance as a system where most of the emitters are located at its center should [225]. In terms of larger scales, the Bullet Cluster provides a snapshot of a past collision between two clusters where the images obtained through X-ray and gravitational lensing show a displacement between gas particles that have interacted electromagnetically and where most of the matter, seemingly non-baryonic, sits [226].

Also the cosmic microwave background (CMB), which has been studied in the last years with an unprecedent accuracy [155, 227], presents anisotropies that can be reproduced if a matter component that interacts only gravitationally is added. A suitable candidate for dark matter has to fulfill several requirements to be compatible with all observations, to fit the current models of structure formation and furthermore to have escaped direct and indirect detection so far, although efforts were not spared.

The hypothesis that dark matter consists of large baryonic objects such as brown dwarf stars or black holes – MACHOs (Massive Astrophysical Compact Halo Object) – was mostly abanoned after realizing that the contribution from all the possible non-luminous objects would but constitute a small percentage of our galaxy's mass, along with the strong constraints imposed on baryonic matter by Big Bang nucleosynthesis and the CMB. This favours non-baryonic subatomic particles as the constituents of dark matter. In order for the mass that would account for the non-baryonic component of haloes to clump together, its particles need to be non-relativistic, which is the reason behind the most favoured (by cosmological N-body simulations) dark matter candidates being called cold. However, non-baryonic non-relativistic types of matter have not been directly observed nor are expected in the standard model of elementary particles. Allied to this got the fact that supersymmetric extensions of the standard model predict the existence of particles with such massive but weakly interacting properties as would be expected, therefore generating what was called the WIMP (Weakly Interacting Massive Particle) [228] miracle. FIMPs (Feebly Interacting Massive Particle) and EWIPs (Extremely Weakly Interacting Particle) are also among the pletora of candidates that have been suggested[1]. In the category of non-relativistic but light particles, one finds weakly interacting slim particles (WISPs) [230] such as axions, which were first proposed in order to give an answer to the strong CP problem [231], axion-like particles and dark/hidden photons [232–235]. Neutrinos have also long figured among the possible candidates [236].

Disclosing more than the gravitational interaction of dark matter has been the goal of numerous direct experiments that often consist of underground facilities containing specific atomic nuclei with the aim of finding the recoil that the dark matter particles interacting with nuclei would cause [237–243] or that include experiments devised to detect the convertion of photons into WISPs and reconvertion into photons by making (strong laser) "light shine through walls" [244, 245].

On the other hand, indirect detection methods focus on detecting the signal from decay or annihilation of dark matter particles. Several were the experiments that have been proposed and realized in astrophysical settings with that aim [246–250]. They focus on finding a signal that would be anomalous with respect to the one expected from astrophysical sources. It should coincide with the expected signal from dark matter, at the same time that it should not be able to be ambiguously attributed to other astrophysical processes. If dark matter exists and is decaying and/or annihilating, the products of such processes could generate gamma rays, radio signals, X-rays [251, 252] and neutrinos [253–255] that might reach us. Therefore, the data from telescopes and radiotelescopes that have surveyed the sky in regions, or focusing on objects, that are expected to have a

---

[1] The reader is directed to Ref. [229] for a review on dark matter searches.

large dark matter contribution can be used in order to pose constraints on the dark matter properties, in particular, on their interaction cross-section.

If a certain theoretical assumption on the dark matter (DM) nature and annihilation/decay scheme is capable to, taking into account the astrophysical conditions, predict a certain measurable associated signal, one can compare it with the observed fluxes of particles and verify such predictions. In ideal conditions, this would lead to the dismissal of several hypothesis with strong predictive power, but in reality we are faced with numerous uncertainties related with the astrophysical environment, such that it is difficult to model the different contributions that are part of galactic and extragallatic backgrounds in order to isolate the dark matter contribution. By virtue of their properties, gamma rays have been the most studied messengers in the indirect DM hunt [256–267] and indeed the most stringent results of non-detection of DM come from the γ-ray Fermi telescope [268–270].

This chapter, however, is dedicated to present the potential that lies in the radio band. Given the difficulty in understanding the astrophysical background, all possible techniques at hand must be jointly employed for a thorough analysis to emerge [271–276]. The fact that radio waves are complementary to other search methods and that a new generation of low frequency radiotelescopes is coming up, makes it a powerful and timely-relevant method to probe dark matter. Previous radio searches were mostly focused on the Galactic Center, which is an excellent region since that is where synchrotron radiation from DM annihilation would be more concentrated [277–284]. This is the case since the galactic magnetic field is stronger in the center. A disadvantage of these analyses is that they highly depend on the assumed dark matter mas distribution, which is unknown [285]. The Galactic Center is also where astrophysical foregrounds are stronger. That has been bypassed by looking at galactic latitudes far from the galactic disk, since the highest concentration of objects in the central region lies in the disk. Instead, the subject of interest in this chapter will be the study of possible annihilation products in galactic subhaloes. This has been analysed, for example, for dwarf galaxies [286–289] and the galactic halo [290,291]. We will focus in a particular High Velocity Cloud called the Smith Cloud [292]. Natural units are used throughout this chapter.

4.1 Synchrotron Radiation and Radio Flux

First, the basics of synchrotron emission in the context of dark matter are shortly overviewed in order to derive the relevant radio flux to our case. DM particles can in principle annihilate in several different final state particles, out of which charged particles.

Synchrotron radiation is a result of charged particles moving through a magnetic field [293] and is present throughout the galaxy due to the galactic magnetic field – leading to the diffuse synchrotron background, which has been observed in radio sky maps [294].

It can be shown (see e.g. [295] for derivation) that the synchrotron power spectrum of a particle of charge e in a uniform magnetic field, as a function of the particle's energy and frequency, is

$$P_{\text{synch}}(E, \nu, \boldsymbol{r}) = \frac{\sqrt{3}e^3}{m_e} B(\boldsymbol{r}) F\left(\frac{\nu}{\nu_c}\right) , \tag{4.1}$$

where ν is the frequency, $B(\boldsymbol{r})$ is the magnetic field and F is a function whose definition depends on the type of magnetic field the electron or positron is embedded in. Assuming a uniform magnetic field, $B(\boldsymbol{r})$ can be reduced to the perpendicular component along the line of sight (i.e. $B_\perp = B(r)\sin\alpha$, where α is the pitch angle) and

$$F_{\text{uni}}(x) \equiv x \int_x^\infty K_{5/3}(x')dx' , \tag{4.2}$$

with $K_n(x)$ the modified Bessel function of order n.

If instead a randomly oriented magnetic field is considered, the changes it implies for the synchrotron power spectrum can be absorbed in a different function [296]

$$F_{\text{rand}}(x) = x^2 \left[K_{4/3}(x)K_{1/3}(x) - \frac{3x}{5}\left(K_{4/3}^2(x) - K_{1/3}^2(x)\right)\right] , \tag{4.3}$$

The critical frequency has been defined as

$$\nu_c \equiv \frac{3}{4\pi}\frac{e}{m_e} B_\perp \gamma^2 \tag{4.4}$$

$$\simeq 16\,\text{MHz}\left(\frac{E}{\text{GeV}}\right)^2\left(\frac{B_\perp}{\mu\text{G}}\right) , \tag{4.5}$$

where γ is the Lorentz factor. The synchrotron emission from one electron can be related to the emissivity through [295]

$$j_\nu = \int dE P_\nu^{\text{synch}} f_e , \tag{4.6}$$

where f_e is the number density of electrons per unit energy. Integrating it along the line of sight (l.o.s.) provides the synchrotron flux produced by an isotropic distribution that reaches an observer on earth. The flux density produced by a generic distribution of isotropic emitters is given by [297]

$$S(\nu) = \frac{1}{4\pi}\int d\Omega \cos\theta \int_{\text{l.o.s.}} d\ell(\Omega) j_\nu(\boldsymbol{r}) \tag{4.7}$$

$$\simeq \int dV \frac{j_\nu(\boldsymbol{r})}{4\pi\ell^2} , \tag{4.8}$$

where $\boldsymbol{r}$ is the central position on the solid angle Ω enclosed by a volume V and where $\mathcal{O}(\theta^2)$ terms have been neglected, since only sources of a small angular size are to be of interest in the following.

To obtain the electron number density, one has to solve the equation that determines the electron propagation of the system. Before, it is necessary to assess the characteristics of the system under study before proceeding, which shall then be introduced in the next section.

4.2 The Smith Cloud

The Smith Cloud was first detected in the sixties through the 21-cm HI line measurements of the Dwingeloo radiotelescope [292]. It is situated at around 12.4 ± 1.3 kpc away from the Sun and 2.9 ± 0.3 kpc below the galactic plane [298] and its large radial velocity consecrate it as a High Velocity Cloud (HVC).

HVCs are objects that stand out due to their velocities with respect to the local standard of rest being too high to be compatible with galactic rotation. Their formation can apparently be attributed to more than one effect, for example, due to the Galactic Fountain (where supernovae from the galactic disk spring hot gas into the halo, which after cooling down falls back towards the disk), by neighbouring dwarf galaxies tides that stream gas outwardly (of which the Magellanic Stream is an example) or through intergalactic clouds of low-metallicity being accreted to the Milky Way [299]. The closer the cloud to the Milky Way, the more likely it is that it was originated from the Magellanic Clouds, while more distant clouds show to be compatible with models of gas which is infalling for the first time and, thus, that have no DM subhalo present [300, 301]. The suggestion of a DM subhalo was posed due to the compatibility between the expected dark matter clump distribution and the spatial distribution of a sub-population of HVCs [302, 303]. To the class of HVCs that are expected to be have a significant DM subhalo belong clouds that originated in DM subhaloes that, instead of forming stars, only retained their gaseous component [303, 304].

The metallicity of the Smith Cloud (SC) was pointed out as a reason for it to possibly be galactic recycled material [305], which would correspond to the absence of a dominant DM component. In contrast, other studies have concluded that only through the assumption of the presence a DM subhalo could the cloud gas have survived crossing through the galactic plane (at around 70 Myr ago), for which evidence is gathered considering the orbit of the cloud that can be inferred from its velocity, along with other features. Tidal stripping would have disrupted a cloud with the same HI content upon its the passage through the galactic disk. However, the cloud could have endured to be gravitationally bound if embedded on a $2 \times 10^8 M_\odot$ DM halo [306]. This has been substantiated by simulations that furthermore favour a spherically symmetrical shape for the SC [307]. The approximation of the cloud to a spherical symmetric object is thus justified and this assumption taken from here onwards.

Measurements of the magnetic field of the SC are key to our interest in using it for DM detection through synchrotron methods, since from (4.1), one expects that the stronger the magnetic field magnitude, the higher the resulting flux, which is essential to be able to discriminate between other sources of radio and the expected DM signal. The SC has in fact a field even stronger that the typical Milky Way magnetic field (of a few μG), with a peak of $\gtrsim 8\,\mu$G [308] and with a line of sight component of about $B_{||} \geq 6\,\mu$G [309].

4.3 Propagation of Synchrotron Emission from the Smith Cloud

Once acquainted with the Smith Cloud, one can come back to the problem of obtaining the electron number density distribution. The situation in this case is clearly parallel to the one found in the propagation of cosmic rays through the intergalactic medium performed in §3.2.3 – one of the consequences of physical phenomena being regulated by the same laws is that the same methods apply to study countless situations. The propagation of the injected electrons f_e can be modelled through the Boltzmann equation, which can be used in the limit where one considers that electrons adiabatically lose energy through different processes and randomly scatter with the magnetic field, suffering diffusion – resulting in the diffusion-loss equation. Taking it in the stationary regime, i.e., assuming that the total number of electrons does not change in time, the diffusion-loss equation in a spherically symmetric form yields

$$\partial_t f_e = D(E)\frac{1}{r}\partial_r^2(rf_e) - \partial_E[-b(E)f_e] + Q_{\mathrm{DM}}(r,E) \equiv 0 \ , \tag{4.9}$$

where D represents the diffusion coefficient, b is the energy-loss coefficient and Q_{DM} is the electron source function. Determining these coefficients and function is therefore essential to obtain the radio flux through (4.6), which is the focus of the next subsections.

4.3.1 Dark Matter Annihilation and Source Function

The annihilation rate per volume is proportional to the product of the DM particles density n_{DM}, following

$$\Gamma_{ann} = \langle\sigma v\rangle n_{\mathrm{DM}}^2 \ , \tag{4.10}$$

where σ is the annihilation cross section and v is the electron velocity. This implies that the number of annihilations per unit volume per unit time is $\Gamma_{ann}/2$, which allows the number of $e^{\pm}$ (produced in the annihilation or decay and fragmentation process) per unit time per volume and per particle energy to be written as

$$Q_{\mathrm{DM}} = \frac{\langle\sigma v\rangle}{2m_{\mathrm{DM}}^2}\rho^2(\boldsymbol{r})\sum_{\mathrm{chann.}}\mathrm{BR}\frac{dY_e}{dE} \ , \tag{4.11}$$

where m_{DM} is the DM particle mass, $\rho(\boldsymbol{r})$ is the DM mass density of the cloud as a function of its center $\boldsymbol{r}$ and dY_e/dE is the electron yield of an annihilation channel with a certain branching ratio BR between energies $(E, E+dE)$. In the case of considering that dark matter is not its own antiparticle, a factor of 1/2 is to be added to (4.11). The velocity average is for most of the dark matter models straightforward.

The benchmark channels that will be considered here are annihilations into $b\bar{b}$, W^+W^-, $\tau^+\tau^-$, $\mu^+\mu^-$ and e^+e^-. Furthermore, let CP conservation be assumed, implying that in each annihilation there are as many electrons as positrons produced.

The electron yield as a function of energy and of the considered dark matter mass is tabulated and can be publicly accessed through software packages (e.g. DarkSUSY [310] or micrOmegas [311]), out of which the "Poor Particle Physicist Cookbook for Dark Matter Indirect Detection" [312] was used in this work.

The macroscopical features of the injection are included in (4.11) through the mass distribution ρ. Various profiles have been suggested to mimic the unknown way in which DM mass density gets distributed. To illustrate the impact that the distributions have, two different profiles are subsequently considered, namely a Navarro-Frenk-White distribution [313]

$$\rho_{\mathrm{NFW}}(r) = \frac{r_s \rho_s}{r\left(1+\frac{r}{r_s}\right)^2} \ , \tag{4.12}$$

and an Einasto profile [314]

$$\rho_{\mathrm{Ein}}(r) = \frac{\rho_s}{4} \exp\left\{-\frac{2}{\alpha}\left[\left(\frac{r}{r_s}\right)^{\alpha} - 1\right]\right\} \ , \tag{4.13}$$

where the normalizations ρ_s and r_s are the scale density and scale radius, respectively.

For the Smith Cloud, these parameters were estimated as r_s =1.00-1.08 kpc ρ_s =0.23-0.76 GeVcm^{-3} [315]. The lowest limit on the mass of the DM halo is given, as mentioned, from the fact that the cloud has to survive the passage through the galactic disk, while the upper limit comes from the requirement that the halo did not allow for star formation and therefore it could not have been excessively heavy.

4.3.2 Energy Losses

Following a logic similar to the previous chapter, where cosmic ray protons inevitably lose energy (see §3.2.2) as they propagate, it does not come as a surprise that as electrons propagate in the Galaxy, several interactions that result in energy losses have to be taken into account. Their contributions can be summed in a total term

$$b_{\mathrm{tot}}(E,B) = b_{\mathrm{syn}}(E,B) + b_{\mathrm{ICS}}(E) + b_{\mathrm{Coul}}(E) + b_{\mathrm{Brem}}(E) \ . \tag{4.14}$$

The energy loss due to synchrotron emission can be written as [316]

$$b_{\mathrm{syn}}(E,B) = \frac{4}{3}\sigma_T \left(\frac{E}{m_e}\right)^2 u_B \ , \tag{4.15}$$

where $\sigma_T = 8\pi/3(\alpha_{em}/m_e^2)^2$ is the Thomson cross section and $u_B = B^2/8\pi$ is the magnetic energy density.

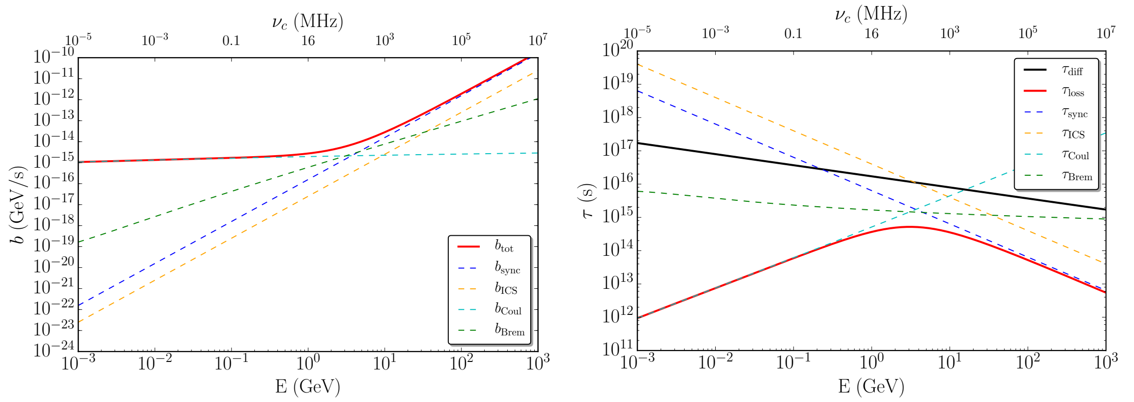

Figure 4.1: Energy loss rate (left panel) and energy loss timescale (right panel) for $e^{\pm}$ arising from DM annihilations in the SC due to different loss processes according to (4.15) (4.16), (4.18) and (4.19).

An analogous expression allows us to estimate the losses through Inverse Compton Scattering off background particles, which occur towards CMB photons and towards star light and infrared light that is diffused by dust particles [316]

$$b_{\rm ICS}(E,B) = \frac{4}{3}\sigma_T \left(\frac{E}{m_e}\right)^2 u_r \ , \tag{4.16}$$

where the radiation energy density u_r includes the contribution from the CMB

$$u_{\rm CMB} = \frac{8\pi^5 T^4}{15} \approx 0.26 \ {\rm eV/cm}^3, \tag{4.17}$$

from the optical and infrared extragalactic background and from the interstellar radiation field.

For collisions with thermal electrons, the Coulomb term is given approximately by [317]

$$b_{\rm Coul}(E) \approx 1.2 \times 10^{-12} n_e \left[\frac{\log(\gamma/n_e)}{75} + 1\right] \tag{4.18}$$

and for Bremsstrahlung losses one can use [318]

$$b_{\rm Brem}(E) \approx 1.51 \times 10^{-16} n_e E \left[\log\frac{\gamma}{n_e} + 0.36\right] \ , \tag{4.19}$$

where n_e is the average number density of electrons. Hydrodynamical simulations of the SC have taken gas densities in the range $n_{\rm H} = 0.1 - 0.5$ cm^{-3} such that $n_e = 0.5$ cm^{-3} is chosen as fiducial value and the average magnetic field value taken is $B = 10$ μG [306,308]. Plotting in Figure 4.1 the contributions of each energy loss mechanism and the respective energy loss timescale $\tau = E/b$, one sees their relative importance. It is also visible that the diffusion timescale is larger than the timescale for synchrotron losses for $\nu \gtrsim$ MHz. In this way, one ensures that it is viable to study the synchrotron emission of the Smith

Cloud for frequencies of the order and higher than MHz, because the signal is likely to remain unaffected by diffusion. The timescale for diffusion is computed through

$$\tau_{\text{diff}}(E) = \frac{R_{\text{SC}}^2}{D_0}\left(\frac{B}{E}\right)^{1/3} , \tag{4.20}$$

where the radius of the Smith Cloud is $R_{\text{SC}} = 3$ kpc and where the diffusion coefficient will be introduced in the next subsection in (4.21). At lower energies, electrons mostly suffer energy losses from Coulomb scatterings, while for electrons of energies of a few GeV and higher, synchrotron emission is the dominant energy loss process.

4.3.3 Diffusion

Recall the discussion around diffusion in the context of cosmic rays in §3.4, which can also be applied in this case, where diffusion takes place due to the turbulent component of the magnetic field. The Bohm diffusion approximation yields for the energy dependence of the diffusion coefficient the usual power law

$$D(E) = D_0\left(\frac{E}{E_0}\right)^{\delta} , \tag{4.21}$$

with the spectral index δ and the normalizations D_0 and E_0 for the diffusion coefficient and energy, respectively. In the following, E_0 was arbitrarily chosen as 1 GeV, since this is the order of magnitude at which synchrotron losses become dominant, and D_0 is a free parameter, which will be varied to show the impact of stronger or weaker diffusion assumptions in §4.6.

Introducing the Syrovatskii Variable

The way in which D, b and Q were represented in the above sections is such that they depend only on the particle's energy and not on the variable $\boldsymbol{r}$. This is pivotal for the next step that will be performed in order to solve (4.9) analytically: introducing the Syrovatskii variables T and λ that enable the effective number of variables of the system to be reduced [319]. Defining the Syrovatskii variables as [319, 320]

$$d\lambda = -\frac{D(E)dE}{b(E)} \quad ; \quad T = t - \tau \, , \quad d\tau = dt - \frac{dE}{b(E)} , \tag{4.22}$$

we can redefine $\tilde{f} \equiv b f_e$ and $\tilde{Q} = bQ/D$. The diffusion-loss equation (4.9) turns then to be analogous to a heat equation of the kind of

$$\frac{\partial}{\partial\lambda}\tilde{f}(r,\lambda,\tau) - \frac{1}{r}\frac{\partial^2}{\partial r^2}[r\tilde{f}(r,\lambda,\tau)] = \tilde{Q}(r,\lambda) \, . \tag{4.23}$$

It is possible now to use Green's function to obtain the most general solution of (4.23), resulting in

$$\tilde{f}(r,\lambda) = \int d\lambda' d\tau' dr' \frac{r'}{r} G(r,r';\lambda,\lambda';\tau,\tau')\tilde{Q}(r',\lambda') \, , \tag{4.24}$$

where the Green's function that satisfies the one dimensional heat equation is

$$G(r,r';\lambda,\lambda';\tau,\tau') = \Theta(\lambda-\lambda')\frac{\mathrm{e}^{-\frac{r^2+r'^2}{4(\lambda-\lambda')}}}{\sqrt{\pi(\lambda-\lambda')}}\sinh\left[\frac{rr'}{2(\lambda-\lambda')}\right]\delta(\tau-\tau')\ , \tag{4.25}$$

with boundaries set at infinity. This is an adequate boundary because the Smith Cloud is located within the Milky Way's diffusion disk. These considerations show that the most appropriate variable to determine electron propagation is $\lambda(E)$, whose physical meaning is the typical length scale of diffusive transport $\sqrt{\lambda}$ in which an electron's energy significantly drops. The Syrovatskii variable λ is positive under the condition that the energy dependence of the total energy loss b is harder than that of the diffusion coefficient D, which are positively defined, along with Q.

The breaking point of this approximation is reached when λ is greater than the height of the diffusion zone of our galactic disk squared. For the propagation parameters to be compatible with Boron over Carbon ratio measurements, it implies that $\sqrt{\lambda} \lesssim 5$ kpc [321].

Changing to the Syrovatskii variable in (4.11), results in

$$\tilde{Q}(r,\lambda) = \frac{\langle\sigma v\rangle}{2m_{\mathrm{DM}}^2}\rho^2(r)\sum_{\mathrm{chann.}}\mathrm{BR}\frac{dY_e}{d\lambda}\ , \tag{4.26}$$

which leads the synchrotron emission to be cast in the form

$$\begin{aligned} j_\nu(r) &= \int d\lambda\frac{P_\nu^{\mathrm{synch}}[E(\lambda)]}{D[E(\lambda)]}\int d\lambda'\int dr'\frac{r'}{r}G(r,r',\lambda,\lambda')\tilde{Q}(r',\lambda') \qquad (4.27)\\ &= \int dE\frac{P_\nu^{\mathrm{synch}}(E)}{b(E)}\int d\lambda'\int dr'\frac{r'}{r}G(r,r',\lambda(E),\lambda')\tilde{Q}(r',\lambda')\ . \end{aligned}$$

At higher electron energies, $E \gg 1$ GeV, the Syrovatskii variable follows also a power law, $\lambda = \lambda_0(E/E_0)^{-\alpha}$, where the normalization $\sqrt{\lambda_0}$ is chosen to be the typical distance diffused by an electron of 1 GeV until it loses most of its energy. The spectral index for a Kolmogorov spectrum is $\alpha = 3/2$, which will also be used here.

4.4 Radio Flux from the Smith Cloud

Another bridge can be built with the ingredients presented so far by linking the integrated P_{synch} in frequency with the synchrotron energy loss rate

$$\begin{aligned} P_{\mathrm{synch}} &= \frac{b_{\mathrm{synch}}(E,B_\perp)}{\nu_c(E,B_\perp)}\tilde{F}\left(\frac{\nu}{\nu_c}\right) \qquad (4.28)\\ &= \frac{b_{\mathrm{synch}}(E_0,B_\perp)}{\nu_c(E_0,B_\perp)}\tilde{F}\left(\frac{\nu}{\nu_c}\right)\ , \qquad (4.29) \end{aligned}$$

where the fact that the energy dependence of P_{synch} in (4.1) is enclosed only in the function F was used. For a uniformly oriented magnetic field $\tilde{F}_{\mathrm{uni}}(x) = 9\sqrt{3}/(8\pi)F_{\mathrm{uni}}(x)$, while for a randomly oriented field $\tilde{F}_{\text{rand}}(x) = 27\sqrt{3}/(4\pi)F_{\text{rand}}(x)$, which were normalized in order that $\int \tilde{F}(x)dx = 1$.

Assuming that for the purpose of this analysis the point source approximation holds, the flux can be written as

$$S(\nu) \simeq \frac{1}{4\pi d^2}\int dV n_e(\boldsymbol{r})\epsilon_\nu(\boldsymbol{r}) = \frac{1}{4\pi d^2}\int dE P_\nu^{\text{synch}}(E)N_e(E) \ , \tag{4.30}$$

where the total number of electrons inside the cloud is given by $N_e(E) = \int dV f_e$. By virtue of the Gauss theorem, the number of electrons $N_e(E)$ with energies between E and $E + dE$ can be written in the following simple way

$$\frac{d}{dE}[b(E)N_e(E)] = -4\pi \int dr r^2 Q_{\text{DM}}(r, E) - 4\pi R_d^2 D(E)\nabla_r f_e|_{r=R_d} \ , \tag{4.31}$$

where the last term represents the escape rate of electrons and which is the only quantity dependent on the diffusion model. This term can be neglected in the regime where the diffusion volume is large, $R_d^2 \gg \lambda(E)$. Inserting into it (4.11), the total flux (4.30) can be factorized in a form that isolates the frequency-dependent terms

$$S(\nu) \simeq J_{\text{SC}}\frac{\langle\sigma v\rangle}{8\pi m_{\text{DM}}^2}\sum_{\text{chann.}} \text{BR}\frac{dY_{\text{radio}}}{d\nu}, \tag{4.32}$$

where the advantage of defining J_{SC} is that it is the same as the one found in gamma ray DM annihilation studies of the Smith Cloud. In (4.32) the radio yield is defined in terms of the electron yield as

$$\frac{dY_{\text{radio}}}{d\nu} = \int dE P_\nu^{\text{synch}}(E)\frac{2Y_e(E)}{b(E)} \tag{4.33}$$

$$= \int dE \frac{2f_{\text{syn}}(E)Y_e(E)}{\nu_c(E)}\tilde{F}\left(\frac{\nu}{\nu_c(E)}\right) \ , \tag{4.34}$$

where $f_{\text{syn}} = b_{\text{syn}}/b_{\text{tot}}$ denotes the fraction of energy lost by the electron in synchrotron emission and $Y_e(E) = \int_E^{m_{\text{DM}}} dY_e/dE$ is the total yield of electrons with energies larger than E. The meaning of the radio yield, in an analogous way to the particle physics yield, is then the energy that a single annihilation radiates in the radio band between frequencies ν and $\nu + d\nu$.

The factorization of (4.32) enables the total flux to be easily obtained and compared to the gamma ray flux. It is sensible that both fluxes can be cast under similar forms since the physical process they represent is the same, namely, the straight propagation of electromagnetic radiation. Note that this result is totally independent from the diffusion model assumed, representing a quite general feature. If diffusion would not have been approximated to such a simple form as (4.21), but taken as a more complicated tensor, (4.31) would still hold as long as the volume is infinite. This is a consequence of energy losses being efficient regardless of the manner in which electrons diffuse.

As long as the volume of the Smith Cloud is larger than the typical diffusion volume, i.e. $\sim \lambda^{3/2}$, (4.32) is expected to be valid. It is important to understand why this is a reasonable assumption. The SC moves at 89.7 km s^{-1} relative to the Local Standard of Rest (LSR), which follows the mean motion of Milky Way's matter. During a timescale of Myr, which represents the typical diffusion timescale of the SC, the cloud is going to move on the kpc scale, which is about the scale of the diffusion halo. Therefore, the assumption that the problem is stationary and spherically symmetric can be questioned. To gain a better understanding of the situation, let us consider the rest frame of the Smith Cloud, which is embedded on a wind of baryonic galactic matter of density ρ_m and moves at $v_{\rm LSR}$. First, if the velocity of the wind is constant, stationarity still applies. A wind gradient is in principle negligible since the SC is not in the vicinity of the galactic arms. Regarding isotropicity, one has to consider whether the ram pressure of the wind has the capacity to significantly distort the diffusion halo when compared to a spherical symmetric shape. It is the magnetic field that confines electrons and positrons within the Smith Cloud, therefore one can compare the magnetic pressure $p_B \sim B^2/2$ with the ram pressure $p_R \sim \rho_m v_{\rm LSR}^2$. It has already been concluded in Refs. [308, 309] that the magnetic pressure is larger than the ram pressure and thus is it also justified that the problem gets approximated to a spherical symmetric one.

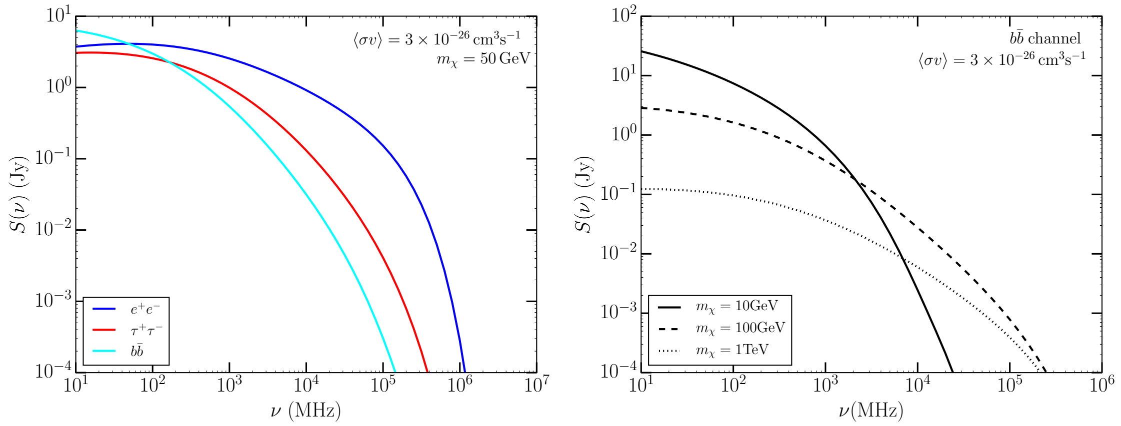

Figure 4.2: Prediction of the synchrotron emission flux density of the Smith Cloud from DM annihilations as a function of frequency, according to (4.32). *Left*: Flux $S(\nu)$ due to the annihilation into different particle pairs with BR=1 for a fiducial mass m_χ =50 GeV. *Right*: Flux $S(\nu)$ due to the annihilation into $b\bar{b}$ pairs with BR=1 for different DM masses. Adapted from Ref. [3].

The total radio flux can then be obtained through (4.32), as plotted in Figure 4.2, where the J-factor used in Ref. [306] is also taken here. An NFW DM distribution profile was assumed, with ρ_s =0.57 GeVcm^{-3} and r_s = 1.07 kpc and the magnetic field of the SC

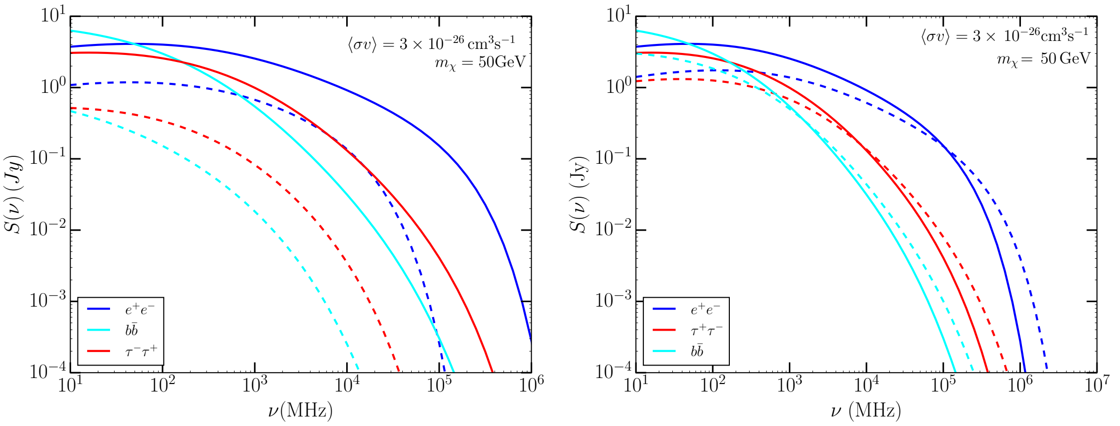

Figure 4.3: Prediction of the synchrotron emission flux density of the Smith Cloud from DM annihilations as a function of frequency, according to (4.32). *Left*: Comparison between the flux obtained for a random magnetic field of strength $B = 10\,\mu$G (solid curves) and $B = 1\,\mu$G (dashed curves). *Right*: Comparison between the flux obtained for a randomly distributed magnetic field (solid curves) and a coherent magnetic field (dashed curves).

was admitted to be randomly oriented with an average strength of $B = 10\,\mu$G [308]. The DM annihilation cross-section used here is that obtained from cosmology if DM would have thermally decoupled, i.e. $\langle\sigma v\rangle = 3\times10^{-26}$ cm^{3}s^{-1}.

Changing the annihilation channel, the DM particle mass and the magnetic field, the synchrotron signal in Figs. 4.2 and 4.3 shows a cut-off in frequency that is a general feature of synchrotron emission related to dark matter annihilation. This can, for example, also be observed in galactic center studies, e.g. in Fig. 3 of Ref. [322], both for annihilation and decay synchrotron fluxes. This cut-off occurs at a frequency given by (4.4) and it is noteworthy that the radio spectrum at frequencies sufficiently smaller than ν_c is relatively flat. As a consequence, in our case, for frequencies below approximately 100 MHz, regardless of the annihilation channel or mass considered, one can approximate the synchrotron spectrum to a constant value. The critical frequency (4.4) expresses the frequency at which the power peaks and this is the sense behind the upper axis of Fig. 4.2, which relates a certain energy to only one frequency value – monochromatic approximation. Since the heavier the mass of the DM particle, the higher the critical frequency associated to it, at higher frequencies, a lighter DM particle – which would display a lower cut-off frequency – would be less likely to be observed that a heavier one. Therefore, one concludes that this sort of analyses is both better suited for low frequencies searches and for heavier dark matter candidates.

The effects of the assumptions on the magnetic field are shown in Fig. 4.3. In terms of field strength, reducing B by one order of magnitude (from 10 to 1 μG) results also in a reduction of the total flux by the same amount. In terms of orientation of the magnetic field, it is noticeable that a field randomly oriented, as described by including (4.3) in (4.1), yields a synchrotron flux that is slightly higher than if the field is considered to be uniformly oriented in the region where the spectrum is relatively flat (at lower frequencies). In contrast, a field oriented in a uniform direction, taking (4.2) in (4.1), will result in a slightly higher flux in the region of the cut-off frequency than a field oriented randomly.

4.5 Brightness Temperature

Not only the spectral description of the signal but also its morphological properties are a subject of interest. The latter can be assessed by measuring the brightness temperature, which can be defined as

$$T_B = \frac{1}{8\pi\nu^2}\int_{\text{l.o.s.}} d\ell j_\nu \ . \tag{4.35}$$

Contrary to the results of §4.4, which are independent of the diffusion model, the spatial features of the signal are expected to strongly depend on it. Modelling diffusion as presented in §4.3.3, one can estimate the predicted brightness temperature coming from dark matter annihilations in the Smith Cloud. Choosing a DM mass of 50 GeV, assuming the thermal annihilation cross-section and for annihilations exclusively into $b\bar{b}$ pairs, Fig. 4.4 shows the brightness temperature at a frequency of 1.4 GHz, which corresponds to the 21-cm neutral hydrogen line wavelength, at which the SC was observed first. Despite the previous remark on the better suitability of this approach to lower frequencies, this frequency was investigated due to data availability.

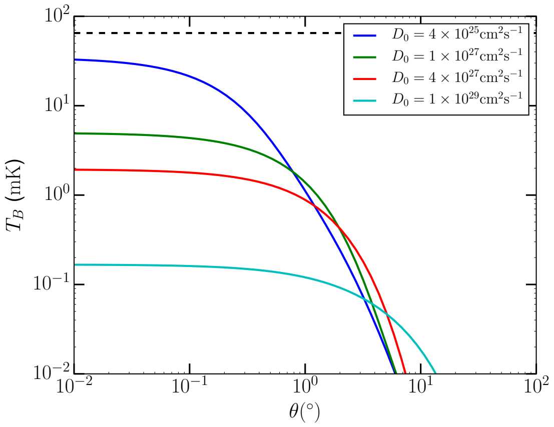

Figure 4.4: Signal brightness temperature at 1.4 GHz as a function of the observational angle for different diffusion coefficients, according to (4.35), for a DM mass of 50 GeV annihilating into $b\bar{b}$ pairs. Adapted from Ref. [3].

To the different diffusion coefficient normalizations $D_0 = 4\times10^{25}$ cm^{2}s^{-1}, 10^{27} cm^{2}s^{-1}, 4×10^{27} cm^{2}s^{-1} and 10^{29} cm^{2}s^{-1} correspond different Syrovatskii variables $\lambda_0 = (0.1\text{ kpc})^2$, $(0.5\text{ kpc})^2$, $(1\text{ kpc})^2$ and $(5\text{ kpc})^2$, respectively. The dependence of the signal with the angle θ around which the emission is centered can be clearly seen: within a certain angular circle of a size determined by the diffusion coefficient, the brightness temperature is going to remain basically constant, while outside of it, the temperature exponentially decays. This is obtained under the simplified conditions assumed for the SC, therefore, it is to be expected that tidal effects of its DM subhalo and anisotropies of, for example, its magnetic field would influence these findings. Nevertheless, the qualitative nature of the signal, i.e., it being localized around a radius which is associated to the typical diffusion length $\sqrt{\lambda}$, is quite general. An implication of this fact is the lack of sensitivity that the radio signal will present with respect to the subhalo distribution of dark matter (see Fig. 4.8).

4.6 Annihilation Cross Section Constraints

After getting acquainted with the spectrum and shape of the signal that DM annihilations in the Smith Cloud could produce, one confirms the potential for detecting a DM signal through synchrotron radiation, viz. the predictions expect emission in the radio band with fluxes large enough that radiotelescopes would be able to resolve them. It is now time to investigate the implications of this signal, i.e. does it have a predictive power that could significantly improve the understanding we already have and push indirect DM detection forward? Various comparisons will be done in this section to analyse and constrain the annihilation cross-section of DM in the context and with the tools gathered in the previous sections. Essentially, the non-observation of DM annihilation products sets limits on the cross-section; the harsher the limits posed by a certain approach, the more predictive power it possesses.

4.6.1 Conservative & Optimistic Limits

The Smith Cloud has been observed in surveys that look at spectral lines, but there is no reason to restrict ourselves to them since the predictions of Fig.4.2 point to a broader spectrum. Therefore, it is all the more interesting to generally consider also continuum radio surveys looking at the Cloud's position. The simplest logical argument that can be constructed is that the non-detection of the cloud implies a bound for the annihilation cross-section of DM.

More concretely, data from the *Radio Continuum Survey of the Northern Sky at 1420 MHz* [323] and from the *Dominion Radio Astrophysical Observatory* (DRAO) 22 MHz [324] are publicly available[2] and have surveyed the location of the Smith Cloud ($l \simeq 39°$

---

[2] `http://www3.mpifr-bonn.mpg.de/survey.html`

$b \simeq -13°$). The emission at these frequencies is dominated by the foreground coming from the Galaxy, making it not possible to resolve the cloud. The predicted brightness temperature caused by potential DM annihilations needs then not to over-shoot the measured brightness temperature evaluated at the center of the cloud, which is assumed to be the DM halo center as well. In other words, the maximal temperature stemming from DM annihilations ($T_{\rm DM}^{\rm max}$) has to be smaller than the observed temperature stemming from the galactic foreground ($T_{\rm fg}^{\rm max}$), which can be formulated, for example, as

$$T_{\rm DM}^{\rm max} < T_{\rm fg}^{\rm max} + 2\sigma \;, \tag{4.36}$$

where here σ is the noise level of the image. The conservative upper limits for DM's annihilation cross-section that can be inferred from this condition are shown in Fig. 4.5 for the mentioned surveys. The same fiducial parameters as in the previous section were taken, along with a diffusion coefficient normalization of $D_0 = 10^{27}$ cm^{2}s^{-1} for an NFW profile (which are also the benchmark parameters taken from here onwards unless otherwise stated).

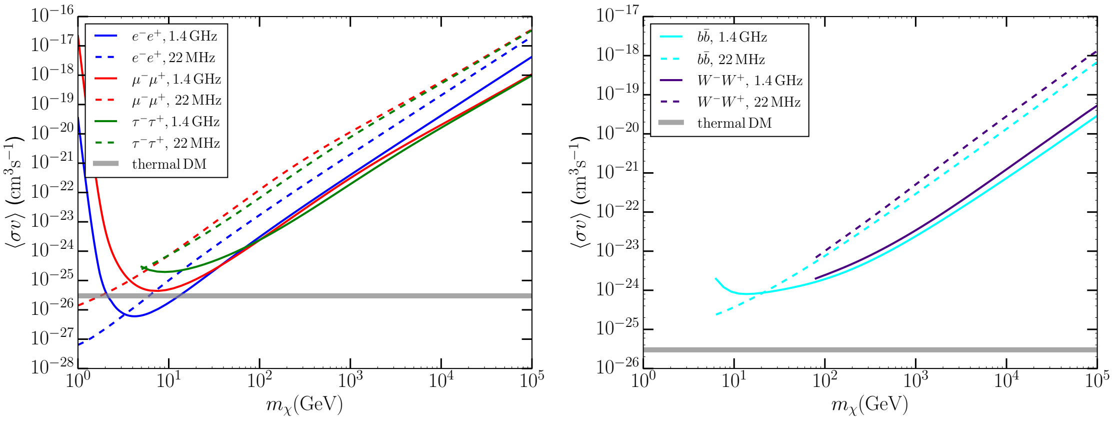

Figure 4.5: Conservative limits on the annihilation cross-section of DM in the SC drawn from the radio continuum surveys of 22 MHz [324] and 1.42 GHz [323]. *Left:* Leptonic annihilation channels; *Right:* $b\bar{b}$ and W^+W^- annihilation channels. Adapted from Ref. [3].

Despite conservative, these limits do not offer much insight, since by assuming that all the cloud's emission would be caused by DM, the constraints are naturally going to be weak. However, to make assumptions on the flux from galactic emission – which contributes the most to the cloud's flux – is an uncertain complex task, since modelling the galactic foreground is subject to numerous unknowns.

The ideal would be to keep the simplicity of the analysis while being more realistic on the foreground emission. One way to strive towards this goal is by performing a rescaling of the Haslam map at 408 MHz [294].[3] The galactic brightness temperature

---

[3] `https://lambda.gsfc.nasa.gov/product/foreground/2014_haslam_408_info.cfm`

will be assumed to follow a power-law in frequency $T_{\rm MW} \propto \nu^{-\beta}$, with the spectral index $\beta \sim 2.5$ [324]. It is reasonable to consider that the DM contribution to the total brightness temperature does not exceed more than 10% of the foreground component. With this criterion ($T_{\rm DM}^{\rm max} < 0.1 T_{\rm fg}^{\rm max}$) the limits on the annihilation cross-section get improved by one order of magnitude compared to what Fig. 4.5 presents.

Allowing for a more speculative limit attainment procedure, one can perform data reduction in order to extract the most meaning from the observations. Let us employ the data reduction of the Green Bank Telescope (GBT) observations performed in Refs. [298, 306], whose maximal HI line frequency emission achieved a median noise level of about 65 mK. Let us estimate this as also the median noise level in the only-noise images of the GBT, that is, at the location of the SC in frequencies slightly shifted from the 1.42 GHz, at which the SC shows no HI emission. Such frequency shifted images can be found in Fig. 2 of Ref. [298], characterized by LSR velocities of ~ -50 km s^{-1} or ~ 150 km s^{-1}. Taking advantage of the relatively moderate signal-to-noise ratio and approximating it to 65 mK should be understood as the rough best limits that can be drawn for the annihilation cross-section from Refs. [298, 306] GBT 1.42 GHz data and not as a statement of the extreme level of accuracy of the results. For that, more detailed studies and data analyses are encouraged to be performed.

The cross-section can be constrained in a way analogous to the conservative limits presented above. More concretely, by comparing the predicted brightness temperature calculated in (4.35) at $\theta = 0$ with the detectability limit,

$$T_{\rm det} \simeq \frac{65 \text{ mK}}{\sqrt{N_{\rm samp} N_{\rm freq}}} \ , \tag{4.37}$$

of an extended signal sampled a number of times $N_{\rm samp} N_{\rm freq}$ by the survey, where $N_{\rm samp}$ is the needed number of pointings to sample the whole angular extension of the DM signal and $N_{\rm freq}$ is the number of independent only-noise maps of the data. The first is obtained via the ratio of the solid angles between the predicted DM signal and the beam solid angle $\Omega_{\rm sig}/\Omega_{\rm beam}$, with

$$\Omega_{\rm sig} = \pi \theta_{\rm eff}^2 \ , \ \theta_{\rm eff} \sim \frac{\sqrt{\lambda_0}}{12 \text{kpc}} \ , \tag{4.38}$$

where the estimated effective angular size is supported by Fig. 4.4, in which one can see that $\theta_{\rm eff} \sim 1^\circ$ if $\lambda_0 = (0.5 \text{ kpc})^2$. The mass of the DM candidate does not play a significant role in estimating the effective angular sizes within the range considered. It is actually the normalization of the diffusion coefficient that has a bigger impact on the angular size, as can be seen through (4.22), where the DM mass will only act as an integration constant. Assuming the beam to be Gaussian, $\Omega_{\rm beam} \simeq 1.133 \theta_{\rm beam}^2$.

The number of only-noise maps depends on the number of line-free images in different shifted frequencies and since the data from Refs. [298,306] is used in this work, so will $N_{\rm freq}$ depend on the amount of images considered in these analyses. The samples at relevant frequencies for us should portray the SC at velocities larger than 150 km s^{-1} or smaller than about -10 km s^{-1} LSR, which correspond to frequencies where the HI line does not dominate the emission (see again Fig. 2 of Ref. [298]). Assuming that out of the 485 frequencies surveyed in Ref. [298], 2/3 are of interest, $N_{\mathrm{freq}} = 323$. The same observations give information on the angular size of the beam, namely that its full width to half power (FWHP) is $3'$. Inserting these values gives the corresponding $N_{\mathrm{samp}} \simeq 1109\theta^{\circ 2}_{\mathrm{signal}}$.

One can now obtain the cross-section limits from the GBT data at 1.42 GHz, as shown in Fig. 4.6 by assuming that no diffuse signal with an angular size of the order of the degree was obtained in the data set chosen. A direct comparison to the limits obtained in Ref. [263] can be done, where the non-observation of an excess of γ-rays by the Fermi Large Area Telescope (LAT) corresponding to the Smith Cloud position constrained the annihilation cross-section.

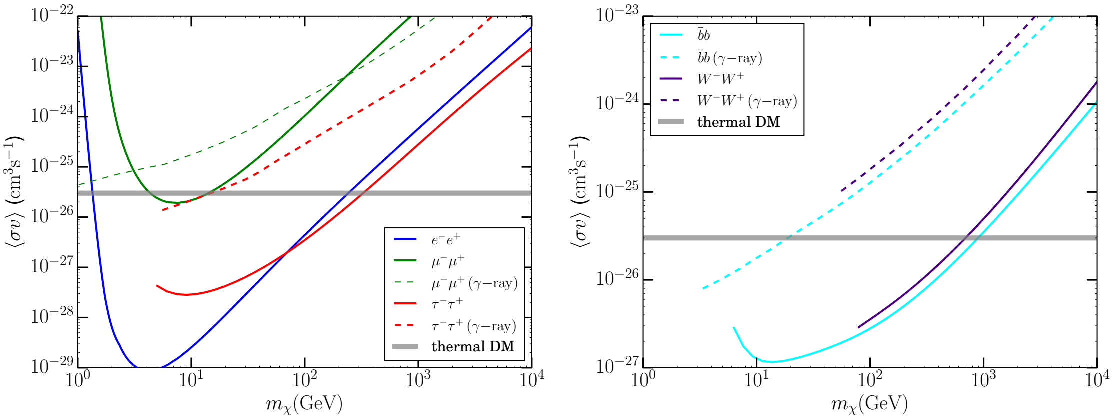

Figure 4.6: Limits (of 2σ) on the DM annihilation cross-section from synchrotron emission using the GBT 1.42 GHz observations of the SC (solid curves). Comparison with the limits obtained from γ-rays in Ref. [263] (dashed curves). *Left:* leptonic annihilation channels; *Right:* $b\bar{b}$ and W^+W^- annihilation channels.

If the diffusion coefficient is expected to impact these results, it is important to have an estimate of by how much. A simple way to realize this is by taking different diffusion coefficient normalizations, namely considering limiting cases. Varying the normalization in the range $D_0 = 4 \times [10^{25} - 10^{29}]$ $\mathrm{cm^2 s^{-1}}$, which corresponds to $\sqrt{\lambda_0} = 100$ pc $-$ 5 kpc, yields the results presented in Fig. 4.7 for the different annihilation channels. To a larger value of D_0 corresponds a weaker limit, which is to be expected from thinking about how a faster diffusion causes the emitting particles to be less localized and thus the synchrotron emission becomes less intense, and vice versa (smaller D_0 values mean that electron diffusion is not so efficient and they remain around a smaller volume, therefore yielding larger synchrotron fluxes).

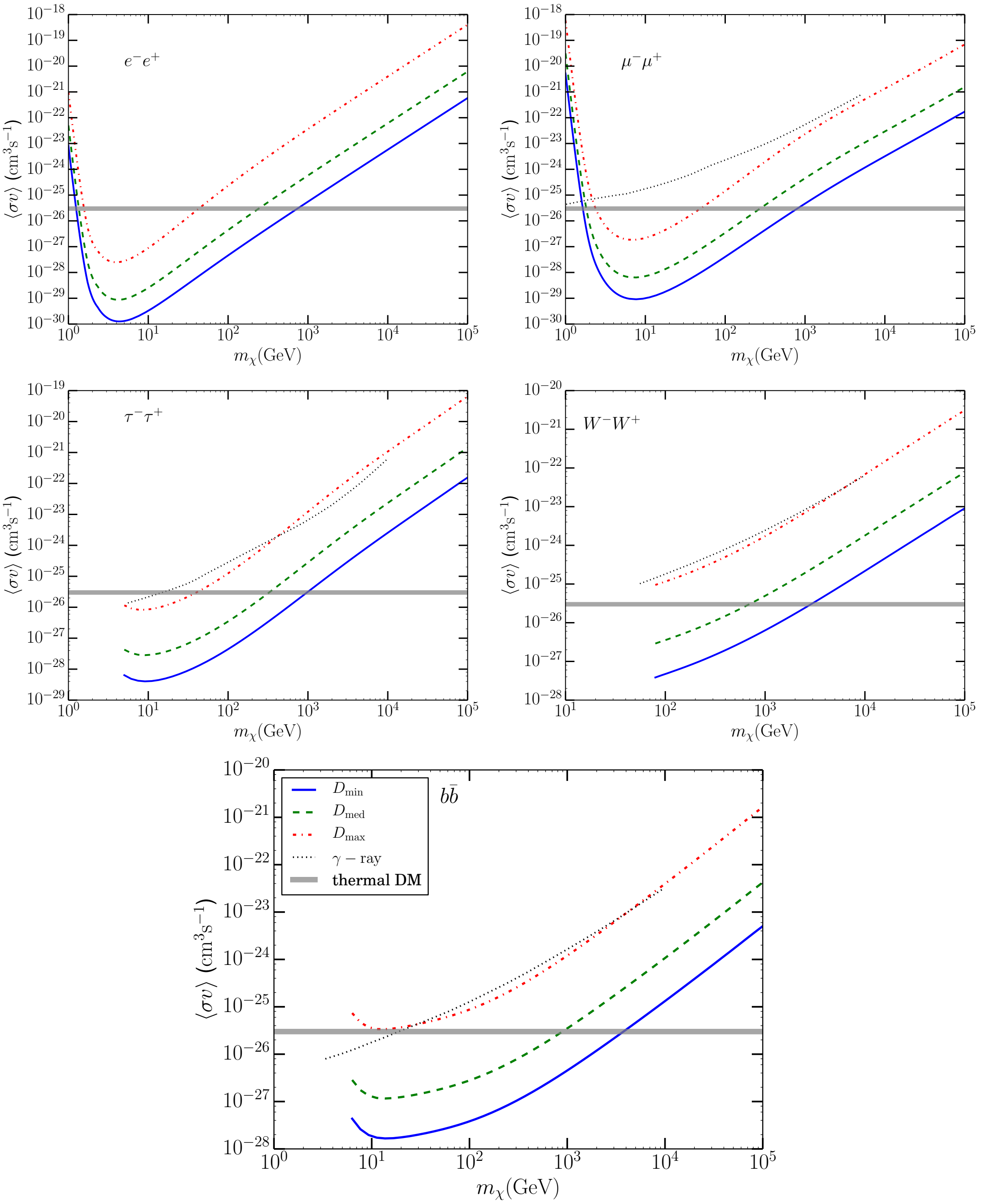

Figure 4.7: Prediction of the annihilation cross-section for different values of the diffusion coefficient normalization D_0 assuming a Kolmogorov diffusion model: $D_{\rm min} = 4 \times 10^{25}$ cm^{2}s^{-1}, $D_{\rm med} = 4 \times 10^{27}$ cm^{2}s^{-1} and $D_{\rm max} = 4 \times 10^{29}$ cm^{2}s^{-1} Comparison with the limits obtained through γ-rays by Ref. [263] for each annihilation channel. From Ref. [3].

It is interesting to compare it to the limits drawn through cosmic ray data, since varying the diffusion coefficient normalization has the contrary effect than in those results. That is the case since the larger the normalization, the faster cosmic rays diffusively propagate and under this condition they can best reach an observer at Earth. Therefore the strongest constraints are given by the higher diffusion coefficient normalizations in the cosmic ray limits, while the nature of synchrotron radiation induces the results of the annihilation cross-section opposite to that of common positron and antiproton signals [325, 326].

Another parameter that enters the limit computation is the magnetic field strength of the cloud. As mentioned previously along with the assumption of a randomly oriented field, Figs. 4.6 and 4.7 were obtained for $B = 10\ \mu$G. Decreasing the magnetic field by one order of magnitude, $B = 1\ \mu$G, has the consequence of weakening the limits here put forward by also approximately one order of magnitude.

One last ingredient that takes part in obtaining the cross-section remains to be analysed: the mass distribution of the cloud. In general this is quite uncertain since simulations of structure formation cannot resolve too small scales (below ~ 100 pc). In the present study however, it was confirmed a posteriori that changing between different profiles yields no terrific insigths and therefore the comparison between an NFW, (4.12), and an Einasto, (4.13), mass distribution is shown for illustrative purposes. In Fig. 4.8 one can see the comparison between the limits on the annihilation cross-section into several channels for both distributions, which differ only on their normalizations. Actually, the ratio between the J-factors from the flux (4.30) in both cases corresponds approximately to the ratio between their annihilation cross-sections.

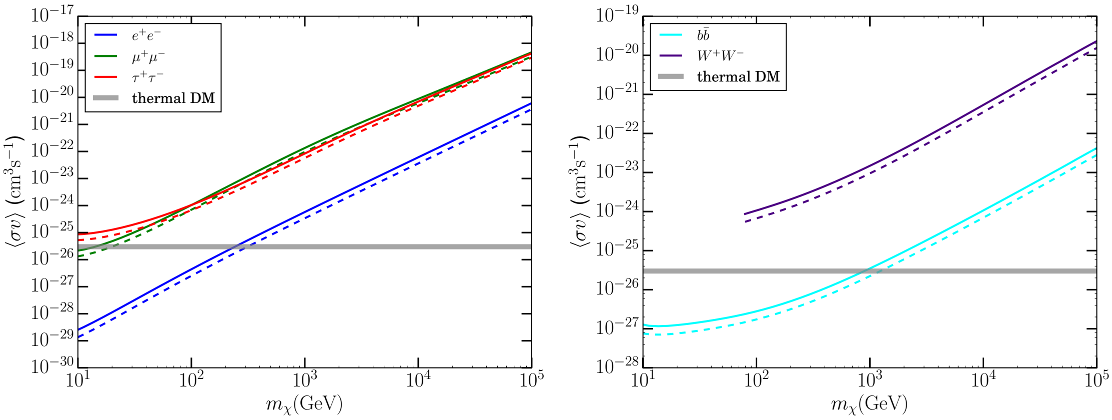

Figure 4.8: Limits on the annihilation cross-section for the SC when considering an NFW profile as in Fig. 4.6 (solid line) and an Einasto profile (dashed line). *Left:* leptonic annihilation channels; *Right:* $b\bar{b}$ and W^+W^- annihilation channels.

An important remark regarding the mass dependence of the limits is yet to be done. In the lower end of the considered DM particle mass range, for $m_\chi \lesssim 10$ GeV, the constraints lift exponentially (cf. left panel of Fig. 4.6). As has been seen in §4.4 through the discussion of Fig. 4.2, there is a characteristic frequency after which the signal suffers a steep cut-off. At a frequency of 1.42 GHz – here considered due to the availability of data on the SC – the signal that annihilating 10 GeV DM particles would produce is negligible and it is no wonder that the limits get substantially weaker for smaller masses. As long as the spectrum of Fig. 4.2 is approximately flat, the limits are relevant, which is the case for heavier DM candidates at this and other such high frequencies. On the other hand, lower frequency searches are more probable to include the region where the spectrum is flat also for lighter DM particles. Comparing radio and γ-ray signals, for heavy masses ($m_\chi \gtrsim 10\text{TeV}$) the first show a softer mas dependence than the latter.

It is clear from Figs. 4.6 and 4.7 that under the chosen regime, the annihilation cross-section of DM from the SC halo drawn by radio is comparable to the constraints that γ-ray studies have set, even though the frequency of 1.42 GHz is much higher than ideal for our approach. One can conclude that radio studies have a comparable predictive power to γ-ray ones, which have deserved much more attention so far.

With the aforementioned strong assumptions on the systematics of the data reduction, the annihilation cross-section is constrained stronger using the radio signal from the Smith High Velocity Cloud with GBT data than using dwarf Spheroidal galaxies (dSphs) with Fermi-LAT data [263, 306].

4.6.2 Prospects with LOFAR

Since – as made clear by Fig. 4.4 and confirmed in terms of the annihilation cross-section for low DM masses by Fig. 4.6 – DM indirect detection through radio yields more potential in the the sub-GHz frequency range, it is natural to ask ourselves what limits are obtained at low frequencies. There are so far no observations of the Smith Cloud in the desired band, but in fact soon a new generation of radiotelescopes, such as LOFAR [327] and the upcoming SKA, is hopefully going to provide them.

This subsection is dedicated to the ones too eager to wait until data is available, since a projection of what can be expected from LOFAR in the context of posing $\langle \sigma v \rangle$ constraints from the Smith Cloud can already be done. In the attempt of accounting for the systematic errors the best way possible, the image noise sensitivies reported in Table B.3 of Ref. [327] are assumed and multiplied by the correction factor

$$1 + \frac{T_{\text{fg}}}{T_{\text{sys}}} \ , \tag{4.39}$$

which should account for the contribution given to the temperature of the system, T_{sys}, i.e. of the LOFAR antennas, by the galactic foreground [328, 329]. The way in which the foreground temperature was estimated was by considering the maximum brightness temperature of several surveys[4] in a square of 3° × 3° centred on the SC, although in all

---

[4] `http://www3.mpifr-bonn.mpg.de/survey.html`

considered cases this implied only a correction on the level of 1%.

The same method as used above (see (4.37)) can then be employed to translate the brightness temperature predicted by DM annihilations in the SC into the temperature detected by the specific experiment under consideration. The detectability limit for an extended source yields a temperature

$$T_{\rm det} \simeq \frac{\Delta S_\nu}{2\nu^2 \Omega_{\rm beam}\sqrt{N_{\rm samp}}} = \frac{\Delta S_\nu}{2\nu^2 \sqrt{\Omega_{\rm beam}\Omega_{\rm sig}}} \,, \tag{4.40}$$

where ΔS_ν is the LOFAR sensitivity at the frequency ν (extracted from Table B.3 of [327]).

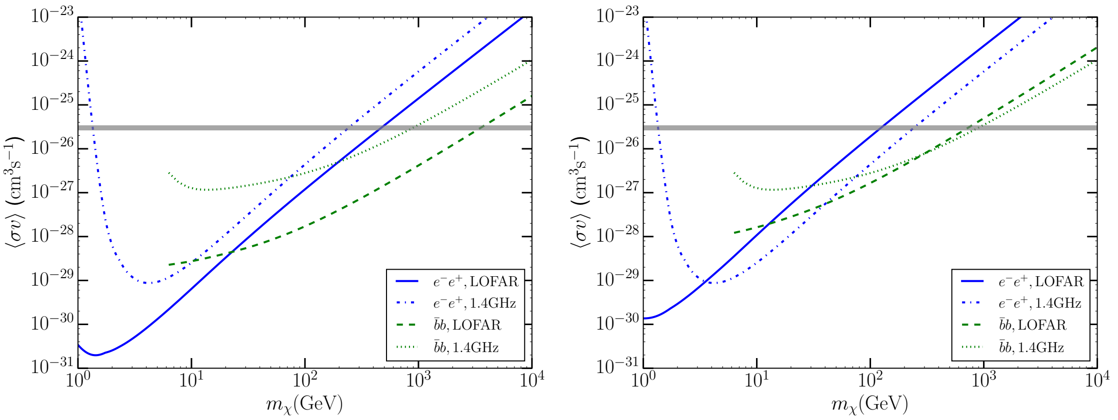

Figure 4.9: Prospect of 2σ limits on the DM annihilation cross-section using LOFAR for 8 hrs of observation time and for a typical beam size of 25″. *Left:* At frequency of 150 MHz (HBA); *Right:* At frequency of 60 MHz (LBA).

Taking LOFAR's Low Band Antenna (LBA, 60 MHz) and High Band Antenna (HBA, 150 MHz) with a beam size of 25″ and a hypothetical observation time of 8 hours with an effective bandwidth of 4 GHz, the cross-section projections are shown in Fig. 4.9. If these measurements would not be able to detect the SC, the results shown would represent the 95% confidence level on the annihilation cross-section of DM provided that the assumptions taken throughout this chapter are valid. The improvement in lowering the cross-section value by this prospect in comparison to the previous limits at high frequency is actually not so prominent, although one does observe that these limits are stronger. To give a broader perspective to these estimations, one should recall the importance of the simplifications assumed, especially the fact that the galactic foreground and astrophysical backgrounds were not conveniently subtracted from the spectrum and that at lower frequencies performing this kind of data reduction is expected to be quite important. Notice that this is well depicted by comparing the limits obtained with LBA and HBA. The enhancement on the signal that is expected as a result of lowering the frequency from 150 MHz to 60 MHz is counteracted and superseded by the inevitable loss in sensitivity,

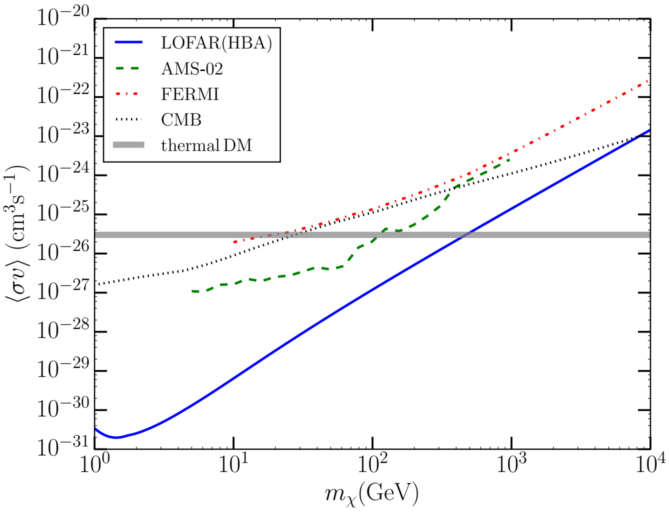

Figure 4.10: Comparison with e^+e^- annihilation cross-section constraints drawn using data from AMS-02 [330], dSphs studies using Fermi-LAT data [331] and the CMB using PLANCK data [332].

making the HBA predictions stronger. This points to the need, not only for a good understanding of the systematics of the observation, but also of realizing signal correlations in a multi-wavelength fashion on the low frequency range.

Before closing the analyses of the results of this chapter, let us compare the LOFAR projections with some of the strongest limits on the annihilation cross-section of DM from various sources of indirect (non-)detection. In Fig. 4.10 a comparison is given between the projected limits given by future HBA LOFAR observations and the limits obtained from the CMB with PLANCK satelitte data [332], from dSph galaxies of the Milky Way observed by Fermi-LAT [331] and from the positron flux derived from the AMS-02 data [330]. It follows that in the case that the data reduction is ideally performed, LOFAR data is among the best ways to constrain dark matter. One should however keep in mind that it is a simplistic procedure to directly compare all of these results, since they are based on some more conservative and some more speculative assumptions. Nevertheless, this serves to contextualize the potential of constraining DM by targeting the SC.

4.7 Summary and Discussion

A look into the Smith high velocity cloud was taken in the light of dark matter phenomenology. If it is a dark matter halo that supports the SC, then this would definitely be a priviledged environment to study the imprint of eventual products of annihilation between dark matter particles that would be carried to us by synchrotron radiation. That is so not only because of the significant amount of DM predicted to exist therein, but also because of the cloud's large magnetic field and its location – out of the galactic disk and not in the direction of the Galactic Center when compared to the earth position, which makes the signal from the cloud be less polluted by the galactic background. The geometry of the SC also collaborates in our favour, since, as discussed, it is likely that the cloud can be described by a spherically symmetric shape. This is one of the most important features to be able to perform a semi-analytical treatment of the synchrotron emission propagation.

One of the general conclusions on the spectral properties of the synchrotron signal induced by DM annihilation is that the spectrum shows a flat behaviour quite independent from the assumed diffusion model in certain ranges. This is verified in the special analysed case of the Smith Cloud for DM particles with masses of [1, 100] GeV and for sub-GHz frequencies, whereas the spectrum is exponentially cut-off after a critical frequency.

Dark matter searches that focus on the Galactic Center have the disadvantage of being highly impacted by the uncertainty around the DM mass distribution of the Galaxy. In our approach, the biggest source of uncertainty is related to the diffusion volume, encapsulated through the Syrovatskii variable. The scale radius of the object under interest must be compared to the Syrovatskii variable. This implies that the signal from the Smith Cloud, as well as from other sub-galactic structures, is going to be rather localized, while this would not be the case in the Galactic Center.

The description of the radio flux that DM annihilations in the SC would cause enabled to draw different constraints for the annihilation cross-section of DM. Although these correspond to a preliminary attempt, where data reduction is not exhaustively performed, it opens up the path that radio searches in the low frequency range could follow to obtain reasonably strong and very competitive limits on the annihilation cross-section. The exploration of the various limits that can be obtained with the present data and that are expected to be obtained with upcoming one followed different approaches. First, conservative limits can be set based on the continuum radio surveys where the SC has not been observed (at 1.42 GHz and at 22 MHz) by simply requiring that the DM signal is lower than the observed in the data. The limits obtained then cannot compete with constraints obtained by analogous γ-ray studies for the Cloud. A simplistic semi-subtraction of the foreground, based on rescaling the Haslam map, improves by one order of magnitude these limits. Daring to pose stronger constraints, the 21-cm line observation of the SC from the GBT was used. Taking its noise level temperature and accounting for details on the beam and sample sizes, the predicted brightness temperature yielded by synchrotron emission from DM annihilation could be compared with these observations. At that frequency, constraints are stronger than that obtained for the SC using γ-rays from dSphs.

The realistic DM signal should lie in between the conservative and the optimistic limits that were presented here. When more evolved methods to remove the effects of fore- and back- ground are employed, the results that are expected to be yielded look rather promising.

For a complete study of this topic, a projection of the limits that will be able to be set with data from LOFAR observations, specifically with the HBA and LBA, was done. This was motivated by the spectral features of the signal favouring studies in the sub-GHz frequency range. Provided that systematics are understood, the constraining power of LOFAR on the annihilation cross-section of DM by targeting the SC is of relevance compared to other methods. The latest results from γ-ray dSphs using Fermi-LAT [270] observations render cross-sections more constraining for large DM masses and less for lighter candidates than Ref. [268], compared for the e^+e^- channel in Fig. 4.10 with the LOFAR prospects.

Finally, let us compare the derived cross-section limits to other synchrotron studies. One finds that compared to targeting the Galactic Center, as in Ref. [322], our results are less stringent in case one takes the conservative bounds. On the other hand, our optimistic bounds are more stringent than the optimistic ones from Ref. [322] in the $b\bar{b}$, e^+e^- and $\tau^+\tau^-$ channels. A comparison can also be made between the contraints drawn from dSphs from the Local Group based on observations from the *Australia Telescope Compact Array* (ATCA) [288] in the $b\bar{b}$ channel. In terms of conservative scenarios, our cross-section is very similar to the one derived in Ref. [288]. In the most optimistic scenario, our cross-sections are less constraining by 3 to 4 orders of magnitude. If all the backgrounds would be successfully subtracted, in this annihilation channel these results would thus place the best bounds on $\langle\sigma v\rangle$. Similarly to our case, it is noticeable, in all but the most daring optimistic case of Ref. [288], that the constraints grow harder as the DM particle mass goes from TeV to GeV values and relax again for masses smaller than a few GeV.

Multi-wavelength searches are encouraged by our results, as well as a good model for the astrophysical processes that can influence the detected signal. It is thus concluded that HVCs are very interesting objects in terms of indirect dark matter searches and that the upcoming radio surveys can be extensively used for this purpose.

Chapter 5

Conclusions and Outlook

In the previous chapters, different systems that rely on the interconnectedness of magnetic fields and particle physics were investigated. The multiple results derived show that applying the same physical principles to various cases permits us to gain insight, or more accurately, to make educated guesses, about a broad range of topics that take place at different scales and moments of the evolution of the Universe. The body of work presented in this thesis can be summarized by the results reported in §2.2.4, 2.3.4, 3.5 and 4.7. This includes, as well, the assumptions and corresponding validity limits relied upon through the course of each chapter.

We have first seen that triangle anomalies change the standard description of magnetohydrodynamics in the presence of a chiral asymmetry. Core collapse supernovae naturally lead to a chiral asymmetry in the core of a protoneutron star that affects the seed magnetic field of the star. If the core of the star is hot enough ($T \gtrsim 20$ MeV), the energy stored in chiral fermions is transferred into magnetic energy. This can amplify a seed magnetic field by several orders of magnitude in a short timescale, after which chirality flipping rates dominate the evolution of the chiral asymmetry and it gets damped along with the decay of the induced field enhancement. Additionally, seed magnetic fields amplified by the CME become maximally helical. However, the length scale and maximal strength of the obtained magnetic fields point towards the fact that the chiral magnetic effect does not produce magnetic fields with characteristics that correspond to the observed surface fields of magnetars, unless other mechanisms that transport the field from small to large scales of the star, and amplify it in this process, are at play. Such could for example be the case of transport via inverse cascade.

The analysis of the CME in the early Universe, in this case at the electroweak symmetry breaking, allowed us to understand how the general features of the evolution of the chiral chemical potential are related to the particle processes. This was specifically realized by analysing the processes the induce chirality flips, both before and after the electroweak transition. It was verified that from non-helical primordial fields, magnetic helicity is created in the presence of a chiral asymmetry. Even weak primordial magnetic fields ($\Omega_{\rm mag} \gtrsim 10^{-15}$) are capable of sustaining a finite asymmetry throughout the transition until electromagnetic chirality flips dominate, around a temperature of 40 MeV. The presence of a chiral asymmetry, in its turn, sustains the magnetic field strength for longer timescales in comparison with the resistive decay that they would suffer in the absence of the CME. These results are relevant, e.g., for hypotheses on the baryon asymmetry of the Universe that are based on the link between helicity and particle processes. They can also be used for predictions of the signature left by primordial magnetic fields on the gravitational wave spectrum.

An important point to take into consideration in further studies of anomalous MHD is the way in which the presence of turbulence affects the aforementioned results. In general, there will be a tendency of the system either to let the magnetic field evolution be dominated by the chiral anomaly or by turbulence. While this work covers the first case, incorporating the latter will not only be a matter of completeness but might change the derived conclusions, especially because the energy transfer rate will be modified. It is known that helical magnetic fields can present an inverse cascade in the presence of turbulence. A magnetic field whose helicity has been created through the chiral magnetic effect that would evolve according to an inverse cascade would be an example of a setting where allying turbulence to the CME renders interesting results. This would apply both in the case of compact stars and in the early Universe. The timescales that dominate the processes in the core of a protoneutron star are rather small. This can allow for a fast transfer of energy from small to large scales if the effect of the chiral anomaly is supported by an adequate turbulent spectrum. In this way, it is possible that the surface magnetic field of compact objects suffers an additional contribution from the field enhancement generated in the core after collapse. One of the consequences of an inverse cascade in turbulent MHD is the growth of the correlation length. By producing helical fields from an initial non-helical seed field, the CME could have enhanced the cosmological magnetic correlation length significantly with respect to the correlation length predicted by magnetogenesis scenarios.

Another example in the past history of the Universe where magnetic fields of the cosmos meet particle interactions was then studied at reionization. The light from the earliest stars caused our Universe to change from a neutral to an ionized state. In parallel, propagating cosmic rays from the first supernovae would, according to what is argued in this work, leave an imprint on the temperature of the traversed medium. A simple but robust reionization model, which can be used for other estimates that do not require a full simulation of the reionization epoch, was developed. Studying the details of energy losses that cosmic rays incur during propagation, culminated in concluding that cosmic ray protons of energies $E \lesssim 10$ MeV can effectively raise the temperature of the neutral intergalactic medium by hundreds of K, leaving a trace that will be measurable by HI 21-cm experiments. This analysis revealed that the degree of magnetization of the IGM at that time can be inferred from such future measurements. The reason being that the mean free path of cosmic rays will significantly change as a function of the magnetic field they were subject to during diffusion. The natural next step to be taken is the computation of the total 21-cm line signal expected to be observed by taking into account the addition of low-energy cosmic rays to the kinetic temperature of the neutral IGM. This temperature is standardly is computed by accounting for the adiabatic expansion of the Universe, the heat produced by ionizations and by the surrounding radiation. Upon availability of data, it would be most relevant to compare the projected signal with the experimentally obtained one. However, in order to compare both and acquire meaningful hints on the population of supernovae at the origin of cosmic ray and the intergalactic magnetic field at that time, several other phenomena need to be taken into account. The contributions to the IGM temperature at high-redshifts from X-rays, dark matter and other possible sources must be well understood in order to isolate the effect of cosmic rays.

A different situation that clearly relies on the link between cosmic magnetic fields and high energy particle physics was analysed next. The magnetic field of the high velocity Smith Cloud allows synchrotron radiation to be emitted and used as a method to constrain the annihilation cross-section of dark matter. Based on the spherical symmetrical properties of the system, an analytical procedure for the solution of the diffusion-loss equation was obtained. That could then be described through the Syrovatskii variable. The flux that would result from dark matter annihilations in the Smith Cloud would lie in the radio band and be most appropriate to be applied to low-frequency observations or to heavier DM candidate searches. The total radio flux predicted turns out to be rather independent from the diffusion details and would have a sufficiently high intensity to be detected by upcoming radiotelescope experiments. With the available data, the limits on the annihilation cross-section that were found show how powerful this method is in constraining dark matter by indirect detection in comparison to other techniques. Likewise, a prediction of what will be achievable with LOFAR data was given. An understanding of the radio background and astrophysical foreground, necessary to perform data reduction, will be essential for the full potential of this method to be realized. Since these results were obtained for WIMPs, in the future a DM candidate-independent approach would be preferable. As an alternative, it would yield complementary results to further investigate the radio flux expected for the low-mass regime by overcoming, possibly through different methods, the limitation of the frequency cut-off that forced our results to be more constraining for heavier ($m_\chi \gtrsim 5$ GeV) particles. The method developed can be applied to other sub-galactic structures, as long as they are approximately spherically symmetric. This could be of interest to, for example, dSph galaxies.

Apart from the unique contributions given to each of the problems that deserved attention in the previous chapters, there is also an equally important more general sense to it. Magnetohydrodynamics will be modified in the same way in the presence of a chiral asymmetry in astrophysics – in the interior of a neutron star – and in cosmology – at the electroweak phase transition. The evolution solutions of the MHD equations differ then in features and end results due to the specific dynamics of the systems under study. Plasma instabilities are triggered by disruptive hydrodynamic or kinetic conditions, i.e. by changes on the properties of the fluid that lead to turbulence. They appeared both related to a chiral asymmetry build up in the core of a protoneutron star and to primordial cosmic rays that traverse the high-redshift IGM. Synchrotron radiation and the synchrotron background is a classical example of the omnipresence and importance of magnetic fields at the galactic and cosmological scales. To study the synchrotron emission that WIMP annihilating dark matter could induce, a model of the propagation, energy losses and diffusion suffered by electrons and positrons until reaching us had to be employed. In clear analogy, a model was developed that encompassed the same components to study the cosmic ray energy deposition before reionization. This thesis serves to corroborate, through the connections just discussed, the Universality that lies at the foundation of Physics. At first glance, the diversity of different systems is hiding the likeness of common aspects. However, once uncovered, the underlying essential correspondences between them becomes immediately apparent. It does so specifically by revealing how magnetic fields are transversal to multiple topics and a crucial entity responsible for the regulation of several phenomena in the cosmos. Far from closed, the topics presented ask for their exploration to be continued – both through the craft of complementary models and through analyses of upcoming observations – and have the potential to contribute to the progress that pushes the boundaries of our current knowledge further.

Bibliography

[1] Günter Sigl and Natacha Leite. Chiral Magnetic Effect in Protoneutron Stars and Magnetic Field Spectral Evolution. *JCAP*, 1601(01):025, 2016.

[2] Petar Pavlović, Natacha Leite, and Günter Sigl. Modified Magnetohydrodynamics Around the Electroweak Transition. *JCAP*, 1606(06):044, 2016.

[3] Natacha Leite, Robin Reuben, Guenter Sigl, Michel H. G. Tytgat, and Martin Vollmann. Synchrotron Emission from Dark Matter in Galactic Subhalos. A Look into the Smith Cloud. *JCAP*, 1611(11):021, 2016.

[4] Natacha Leite, Carmelo Evoli, Marta D'Angelo, Benedetta Ciardi, Günter Sigl, and Andrea Ferrara. Do Cosmic Rays Heat the Early Intergalactic Medium? *Mon. Not. Roy. Astron. Soc.*, 469:416–424, 2017.

[5] V. Cirkel-Bartelt. History of Astroparticle Physics and its Components. *Living Reviews in Relativity*, 11:2, December 2008.

[6] G. Sigl. *Astroparticle Physics: Theory and Phenomenology*. Atlantis Studies in Astroparticle Physics and Cosmology. Atlantis Press, 2016.

[7] Martin L. Bernet, Francesco Miniati, Simon J. Lilly, Philipp P. Kronberg, and Miroslava Dessauges-Zavadsky. Strong magnetic fields in normal galaxies at high redshifts. *Nature*, 454:302–304, 2008.

[8] J. P. Vallée. Cosmic magnetic fields - as observed in the Universe, in galactic dynamos, and in the Milky Way. *New Astronomy Reviews*, 48:763–841, September 2004.

[9] Rafael Alves Batista. *On the cosmological propagation of high energy particles in magnetic fields*. Dr., Universität Hamburg, 2015. Universität Hamburg, Diss., 2015.

[10] L. Davis, Jr. and J. L. Greenstein. The Polarization of Starlight by Aligned Dust Grains. *ApJ*, 114:206, September 1951.

[11] J. G. Bolton and J. P. Wild. On the Possibility of Measuring Interstellar Magnetic Fields by 21-CM Zeeman Splitting. *ApJ*, 125:296, January 1957.

[12] P. P. Kronberg and J. J. Perry. Absorption lines, Faraday rotation, and magnetic field estimates for QSO absorption-line clouds. *ApJ*, 263:518–532, December 1982.

[13] Rainer Beck. Galactic and extragalactic magnetic fields. *Space Science Reviews*, 99(1):243–260, 2001.

[14] Vogt, C. and Enßlin, T. A. A bayesian view on faraday rotation maps – seeing the magnetic power spectra in galaxy clusters. *A&A*, 434(1):67–76, 2005.

[15] A. Neronov and I. Vovk. Evidence for Strong Extragalactic Magnetic Fields from Fermi Observations of TeV Blazars. *Science*, 328:73, April 2010.

[16] S. A. Olausen and V. M. Kaspi. The McGill Magnetar Catalog. *Astrophys. J. Suppl.*, 212:6, 2014.

[17] E. N. Parker. *Cosmical magnetic fields: Their origin and their activity.* 1979.

[18] Andrey Saveliev. *Time Evolution of Primordial Magnetic Fields and Present Day Extragalactic Magnetism.* Dr., University of Hamburg, Hamburg, 2014. University of Hamburg, Diss., 2014.

[19] R. Durrer and A. Neronov. Cosmological magnetic fields: their generation, evolution and observation. *A&A Rev.*, 21:62, June 2013.

[20] Tina Kahniashvili, Alexander G. Tevzadze, and Bharat Ratra. Phase transition generated cosmological magnetic field at large scales. *The Astrophysical Journal*, 726(2):78, 2011.

[21] Michael S. Turner and Lawrence M. Widrow. Inflation Produced, Large Scale Magnetic Fields. *Phys. Rev.*, D37:2743, 1988.

[22] Kazuharu Bamba. Property of the spectrum of large-scale magnetic fields from inflation. *Phys. Rev.*, D75:083516, 2007.

[23] Massimo Giovannini and Mikhail E. Shaposhnikov. Primordial magnetic fields from inflation? *Phys. Rev.*, D62:103512, 2000.

[24] Kandaswamy Subramanian. Magnetizing the universe. *PoS*, MRU:071, 2007.

[25] G. 't Hooft and M. Veltman. Regularization and renormalization of gauge fields. *Nuclear Physics B*, 44(1):189 – 213, 1972.

[26] Stephen L. Adler. Axial vector vertex in spinor electrodynamics. *Phys. Rev.*, 177:2426–2438, 1969.

[27] J. S. Bell and R. Jackiw. A PCAC puzzle: $\pi^0 \to \gamma\gamma$ in the $\sigma-$ model. *Nuovo Cim.*, A60:47–61, 1969.

[28] Dmitri Kharzeev, Karl Landsteiner, Andreas Schmitt, and Ho-Ung Yee. Strongly Interacting Matter in Magnetic Fields. *Lect. Notes Phys.*, 871:pp.1–624, 2013.

[29] Dmitri E. Kharzeev. The Chiral Magnetic Effect and Anomaly-Induced Transport. *Prog. Part. Nucl. Phys.*, 75:133–151, 2014.

[30] Dam Thanh Son and Naoki Yamamoto. Kinetic theory with Berry curvature from quantum field theories. *Phys. Rev.*, D87(8):085016, 2013.

[31] Yukinao Akamatsu and Naoki Yamamoto. Chiral Plasma Instabilities. *Phys. Rev. Lett.*, 111:052002, 2013.

[32] D. T. Son and Ariel R. Zhitnitsky. Quantum anomalies in dense matter. *Phys. Rev.*, D70:074018, 2004.

[33] Max A. Metlitski and Ariel R. Zhitnitsky. Anomalous axion interactions and topological currents in dense matter. *Phys. Rev.*, D72:045011, 2005.

[34] D. E. Kharzeev, J. Liao, S. A. Voloshin, and G. Wang. Chiral magnetic and vortical effects in high-energy nuclear collisions—A status report. *Prog. Part. Nucl. Phys.*, 88:1–28, 2016.

[35] Gokce Basar, Dmitri E. Kharzeev, and Ho-Ung Yee. Triangle anomaly in Weyl semimetals. *Phys. Rev.*, B89(3):035142, 2014.

[36] Qiang Li and Dmitri E. Kharzeev. Chiral magnetic effect in condensed matter systems. *Nucl. Phys.*, A956:107–111, 2016.

[37] Alberto Cortijo, Dmitri Kharzeev, Karl Landsteiner, and María A. H. Vozmediano. Strain induced Chiral Magnetic Effect in Weyl semimetals. *Phys. Rev.*, B94(24):241405, 2016.

[38] V. A. Kuzmin, V. A. Rubakov, and M. E. Shaposhnikov. On the Anomalous Electroweak Baryon Number Nonconservation in the Early Universe. *Phys. Lett.*, B155:36, 1985.

[39] Edward W. Kolb and Michael S. Turner. Electroweak anomaly and lepton asymmetry. *Modern Physics Letters A*, 02(05):285–291, 1987.

[40] K. Enqvist and P. Olesen. On primordial magnetic fields of electroweak origin. *Phys. Lett.*, B319:178–185, 1993.

[41] Massimo Giovannini and M. E. Shaposhnikov. Primordial magnetic fields, anomalous isocurvature fluctuations and big bang nucleosynthesis. *Phys. Rev. Lett.*, 80:22–25, 1998.

[42] Alexey Boyarsky, Jurg Fröhlich, and Oleg Ruchayskiy. Self-consistent evolution of magnetic fields and chiral asymmetry in the early Universe. *Phys. Rev. Lett.*, 108:031301, 2012.

[43] Jitesh R. Bhatt and Arun Kumar Pandey. Primordial magnetic field and kinetic theory with Berry curvature. *Phys. Rev.*, D94(4):043536, 2016.

[44] Hiroyuki Tashiro, Tanmay Vachaspati, and Alexander Vilenkin. Chiral Effects and Cosmic Magnetic Fields. *Phys. Rev.*, D86:105033, 2012.

[45] M. Joyce and Mikhail E. Shaposhnikov. Primordial magnetic fields, right-handed electrons, and the Abelian anomaly. *Phys. Rev. Lett.*, 79:1193–1196, 1997.

[46] Kohei Kamada and Andrew J. Long. Evolution of the Baryon Asymmetry through the Electroweak Crossover in the Presence of a Helical Magnetic Field. *Phys. Rev.*, D94(12):123509, 2016.

[47] Kohei Kamada and Andrew J. Long. Baryogenesis from decaying magnetic helicity. *Phys. Rev.*, D94(6):063501, 2016.

[48] Alexander Vilenkin. Macroscopic parity-violating effects: Neutrino fluxes from rotating black holes and in rotating thermal radiation. *Phys. Rev. D*, 20:1807–1812, Oct 1979.

[49] James Charbonneau and Ariel Zhitnitsky. Topological Currents in Neutron Stars: Kicks, Precession, Toroidal Fields, and Magnetic Helicity. *JCAP*, 1008:010, 2010.

[50] Matthias Kaminski, Christoph F. Uhlemann, Marcus Bleicher, and Jürgen Schaffner-Bielich. Anomalous hydrodynamics kicks neutron stars. *Phys. Lett.*, B760:170–174, 2016.

[51] Kenji Fukushima. Views of the Chiral Magnetic Effect. *Lect. Notes Phys.*, 871:241–259, 2013.

[52] P.H. Frampton. *Gauge Field Theories.* Frontiers in Physics. The Benjamin-Cummings, 1987.

[53] S. L. Adler. Anomalies. *ArXiv High Energy Physics - Theory e-prints*, November 2004.

[54] E. Noether. Invariante Variationsprobleme. *Nachr. D. König. Gesellsch. D. Wiss. Zu Göttingen*, Math-phys. Klasse:235–257, 1918.

[55] J. C. Ward. An identity in quantum electrodynamics. *Phys. Rev.*, 78:182–182, Apr 1950.

[56] Y. Takahashi. On the generalized ward identity. *Il Nuovo Cimento (1955-1965)*, 6(2):371–375, 1957.

[57] C. Becchi, A. Rouet, and R. Stora. Renormalization of the abelian higgs-kibble model. *Comm. Math. Phys.*, 42(2):127–162, 1975.

[58] William A. Bardeen. Anomalous ward identities in spinor field theories. *Phys. Rev.*, 184:1848–1859, Aug 1969.

[59] Stephen L. Adler and William A. Bardeen. Absence of higher-order corrections in the anomalous axial-vector divergence equation. *Phys. Rev.*, 182:1517–1536, Jun 1969.

[60] J. Steinberger. On the use of subtraction fields and the lifetimes of some types of meson decay. *Phys. Rev.*, 76:1180–1186, Oct 1949.

[61] Julian Schwinger. On gauge invariance and vacuum polarization. *Phys. Rev.*, 82:664–679, Jun 1951.

[62] Edward Witten. Quantum field theory and the jones polynomial. *Communications in Mathematical Physics*, 121(3):351–399, 1989.

[63] Meindert van der Meulen, Denes Sexty, Jan Smit, and Anders Tranberg. Chern-Simons and winding number in a tachyonic electroweak transition. *JHEP*, 02:029, 2006.

[64] H. K. Moffatt. The degree of knottedness of tangled vortex lines. *J. Fluid Mech.*, 35:117–129, Jan 1969.

[65] M.A. Berger and G.B. Field. The topological properties of magnetic helicity. *J. Fluid Mech.*, 147:133–148, Oct 1984.

[66] Kenji Fukushima, Dmitri E. Kharzeev, and Harmen J. Warringa. The Chiral Magnetic Effect. *Phys. Rev.*, D78:074033, 2008.

[67] A. Vilenkin. Equilibrium Parity Violating Current in a Magnetic Field. *Phys. Rev.*, D22:3080–3084, 1980.

[68] Petar Pavlović, Natacha Leite, and Günter Sigl. Chiral Magnetohydrodynamic Turbulence. 2016.

[69] A. S. Monin and A. M. Yaglom. *Statistical Fluid Mechanics: Mechanics of Turbulence*. MIT Press, Cambridge, 1975.

[70] E. V. Gorbar, I. A. Shovkovy, S. Vilchinskii, I. Rudenok, A. Boyarsky, and O. Ruchayskiy. Anomalous Maxwell equations for inhomogeneous chiral plasma. *Phys. Rev.*, D93(10):105028, 2016.

[71] P. M. Woods. Observations of Magnetars. In C. Bassa, Z. Wang, A. Cumming, and V. M. Kaspi, editors, *40 Years of Pulsars: Millisecond Pulsars, Magnetars and More*, volume 983 of *American Institute of Physics Conference Series*, pages 227–233, February 2008.

[72] Lilia Ferrario, Andrew Melatos, and Jonathan Zrake. Magnetic Field Generation in Stars. *Space Sci. Rev.*, 191:77–109, 2015.

[73] C. Kouveliotou et al. An X-ray pulsar with a superstrong magnetic field in the soft gamma-ray repeater SGR 1806-20. *Nature*, 393:235–237, 1998.

[74] Andreas Reisenegger. Origin and evolution of neutron star magnetic fields. In *Proceedings, International Workshop on Strong Magnetic Fields and Neutron Star: Havanna, Cuba, April 6-13, 2003*, pages 33–49, 2003.

[75] D. Moss. On the magnetic flux distribution in magnetic CP stars. *MNRAS*, 226:297–307, May 1987.

[76] Robert C. Duncan and Christopher Thompson. Formation of very strongly magnetized neutron stars - implications for gamma-ray bursts. *Astrophys. J.*, 392:L9, 1992.

[77] C. Thompson and R. C. Duncan. Neutron star dynamos and the origins of pulsar magnetism. *ApJ*, 408:194–217, May 1993.

[78] H. C. Spruit. Differential rotation and magnetic fields in stellar interiors. *A&A*, 349:189–202, September 1999.

[79] J. Braithwaite and H. C. Spruit. Structure of the magnetic fields in A stars and white dwarfs. *Nature*, 431:819, 2004.

[80] H. C. Spruit. The source of magnetic fields in (neutron-) stars. In K. G. Strassmeier, A. G. Kosovichev, and J. E. Beckman, editors, *Cosmic Magnetic Fields: From Planets, to Stars and Galaxies*, volume 259 of *IAU Symposium*, pages 61–74, April 2009.

[81] Akira Ohnishi and Naoki Yamamoto. Magnetars and the Chiral Plasma Instabilities. 2014.

[82] Maxim Dvornikov. Impossibility of the strong magnetic fields generation in an electron-positron plasma. *Phys. Rev.*, D90(4):041702, 2014.

[83] Maxim Dvornikov and Victor B. Semikoz. Instability of magnetic fields in electroweak plasma driven by neutrino asymmetries. *JCAP*, 1405:002, 2014.

[84] Dorota Grabowska, David B. Kaplan, and Sanjay Reddy. Role of the electron mass in damping chiral plasma instability in Supernovae and neutron stars. *Phys. Rev.*, D91(8):085035, 2015.

[85] Maxim Dvornikov and Victor B. Semikoz. Magnetic field instability in a neutron star driven by the electroweak electron-nucleon interaction versus the chiral magnetic effect. *Phys. Rev.*, D91(6):061301, 2015.

[86] Maxim Dvornikov and Victor B. Semikoz. Generation of the magnetic helicity in a neutron star driven by the electroweak electron-nucleon interaction. *JCAP*, 1505:032, 2015.

[87] Maxim Dvornikov and Victor B. Semikoz. Energy source for the magnetic field growth in magnetars driven by the electron-nucleon interaction. *Phys. Rev.*, D92(8):083007, 2015.

[88] David B. Kaplan, Sanjay Reddy, and Srimoyee Sen. Energy Conservation and the Chiral Magnetic Effect. 2016.

[89] Maxim Dvornikov. Generation of strong magnetic fields in dense quark matter driven by the electroweak interaction of quarks. *Nucl. Phys.*, B913:79–92, 2016.

[90] Maxim Dvornikov. Magnetic fields in turbulent quark matter and magnetar bursts. 2016.

[91] G. G. Raffelt. *Stars as laboratories for fundamental physics.* 1996.

[92] Adam Burrows and James M. Lattimer. The birth of neutron stars. *Astrophys. J.*, 307:178–196, 1986.

[93] Naoki Iwamoto. Neutrino emissivities and mean free paths of degenerate quark matter. *Annals Phys.*, 141:1–49, 1982.

[94] D. C. Kelly. Electrical and Thermal Conductivities of a Relativistic - Erate Plasma. *Astrophys. J.*, 179:599–606, January 1973.

[95] G. Baym, C. J. Pethick, and D. Pikes. Electrical conductivity of neutron star matter. *Nature*, 224:674–675, 1969.

[96] Jarkko Ahonen and Kari Enqvist. Electrical conductivity in the early universe. *Phys. Lett.*, B382:40–44, 1996.

[97] J. M. Lattimer, M. Prakash, C. J. Pethick, and P. Haensel. Direct URCA process in neutron stars. *Phys. Rev. Lett.*, 66:2701–2704, 1991.

[98] B. L. Friman and O. V. Maxwell. Neutron Star Neutrino Emissivities. *Astrophys. J.*, 232:541–557, 1979.

[99] J. Mao, M. Ono, S. Nagataki, M. Hashimoto, H. Ito, J. Matsumoto, M. G. Dainotti, and S. H. Lee. Matter Mixing in Core-collapse Supernova Ejecta: Large Density Perturbations in the Progenitor Star? *Astrophys. J.*, 808(2):164, 2015.

[100] Maxim Dvornikov. Relaxation of the chiral imbalance and the generation of magnetic fields in magnetars. *J. Exp. Theor. Phys.*, 123(6):967–978, 2016.

[101] H.-T. Janka and W. Hillebrandt. Monte Carlo simulations of neutrino transport in type II supernovae. *Astron. Astrophys. Suppl. Series*, 78:375–397, June 1989.

[102] A. Sulaksono and L. Satiawati. Effects of density-dependent lepton fraction on the properties of protoneutron stars. *Phys. Rev.*, C87(6):065802, 2013.

[103] A. Vilenkin. Cancellation of Equilibrium Parity Violating Currents. *Phys. Rev.*, D22:3067–3079, 1980.

[104] Alexey Boyarsky, Jurg Fröhlich, and Oleg Ruchayskiy. Magnetohydrodynamics of Chiral Relativistic Fluids. *Phys. Rev.*, D92:043004, 2015.

[105] Maxim Dvornikov. Role of particle masses in the magnetic field generation driven by the parity violating interaction. *Phys. Lett.*, B760:406–410, 2016.

[106] Alejandra Kandus, Kerstin E. Kunze, and Christos G. Tsagas. Primordial magnetogenesis. *Phys. Rept.*, 505:1–58, 2011.

[107] Bharat Ratra. Cosmological 'seed' magnetic field from inflation. *Astrophys. J.*, 391:L1–L4, 1992.

[108] A. Dolgov. Breaking of conformal invariance and electromagnetic field generation in the universe. *Phys. Rev.*, D48:2499–2501, 1993.

[109] George B. Field and Sean M. Carroll. Cosmological magnetic fields from primordial helicity. *Phys. Rev.*, D62:103008, 2000.

[110] Andres Diaz-Gil, Juan Garcia-Bellido, Margarita Garcia Perez, and Antonio Gonzalez-Arroyo. Primordial magnetic fields from preheating at the electroweak scale. *JHEP*, 07:043, 2008.

[111] Jean M. Quashnock, Abraham Loeb, and David N. Spergel. Magnetic Field Generation During the Cosmological QCD Phase Transition. *Astrophys. J.*, 344:L49–L51, 1989.

[112] T. Vachaspati. Magnetic fields from cosmological phase transitions. *Phys. Lett.*, B265:258–261, 1991.

[113] A. G. Tevzadze, L. Kisslinger, A. Brandenburg, and T. Kahniashvili. Magnetic Fields from QCD Phase Transitions. *Astrophys. J. Suppl.*, 759:54, November 2012.

[114] Craig J. Hogan. Magnetohydrodynamic Effects of a First-Order Cosmological Phase Transition. *Phys. Rev. Lett.*, 51:1488–1491, 1983.

[115] Guenter Sigl, Angela V. Olinto, and Karsten Jedamzik. Primordial magnetic fields from cosmological first order phase transitions. *Phys. Rev.*, D55:4582–4590, 1997.

[116] M. Gasperini, Massimo Giovannini, and G. Veneziano. Primordial magnetic fields from string cosmology. *Phys. Rev. Lett.*, 75:3796–3799, 1995.

[117] D. Lemoine and M. Lemoine. Primordial magnetic fields in string cosmology. *Phys. Rev.*, D52:1955–1962, 1995.

[118] Massimo Giovannini and M. E. Shaposhnikov. Primordial hypermagnetic fields and triangle anomaly. *Phys. Rev.*, D57:2186–2206, 1998.

[119] Kandaswamy Subramanian. Magnetic fields in the early universe. *Astron. Nachr.*, 331:110–120, 2010.

[120] Robi Banerjee and Karsten Jedamzik. The Evolution of cosmic magnetic fields: From the very early universe, to recombination, to the present. *Phys. Rev.*, D70:123003, 2004.

[121] V. B. Semikoz, D. D. Sokoloff, and J. W. F. Valle. Is the baryon asymmetry of the Universe related to galactic magnetic fields? *Phys. Rev.*, D80:083510, 2009.

[122] V. B. Semikoz and J. W. F. Valle. Chern-Simons anomaly as polarization effect. *JCAP*, 1111:048, 2011.

[123] Maxim Dvornikov and Victor B. Semikoz. Lepton asymmetry growth in the symmetric phase of an electroweak plasma with hypermagnetic fields versus its washing out by sphalerons. *Phys. Rev.*, D87(2):025023, 2013.

[124] Massimo Giovannini. The Magnetized universe. *Int. J. Mod. Phys.*, D13:391–502, 2004.

[125] James M. Cline, Kimmo Kainulainen, and Keith A. Olive. On the erasure and regeneration of the primordial baryon asymmetry by sphalerons. *Phys. Rev. Lett.*, 71:2372–2375, 1993.

[126] Bruce A. Campbell, Sacha Davidson, John R. Ellis, and Keith A. Olive. On the baryon, lepton flavor and right-handed electron asymmetries of the universe. *Phys. Lett.*, B297:118–124, 1992.

[127] K. Kajantie, M. Laine, K. Rummukainen, and Mikhail E. Shaposhnikov. The Electroweak phase transition: A Nonperturbative analysis. *Nucl. Phys.*, B466:189–258, 1996.

[128] Michela D'Onofrio, Kari Rummukainen, and Anders Tranberg. Sphaleron Rate in the Minimal Standard Model. *Phys. Rev. Lett.*, 113(14):141602, 2014.

[129] Michael Dine, Robert G. Leigh, Patrick Y. Huet, Andrei D. Linde, and Dmitri A. Linde. Towards the theory of the electroweak phase transition. *Phys. Rev.*, D46:550–571, 1992.

[130] Steven Weinberg. Gauge and Global Symmetries at High Temperature. *Phys. Rev.*, D9:3357–3378, 1974.

[131] James M. Cline, Kimmo Kainulainen, and Keith A. Olive. Protecting the primordial baryon asymmetry from erasure by sphalerons. *Phys. Rev.*, D49:6394–6409, 1994.

[132] Gordon Baym and Henning Heiselberg. The Electrical conductivity in the early universe. *Phys. Rev.*, D56:5254–5259, 1997.

[133] Chiara Caprini, Ruth Durrer, and Elisa Fenu. Can the observed large scale magnetic fields be seeded by helical primordial fields? *JCAP*, 0911:001, 2009.

[134] Tomohiro Fujita and Kohei Kamada. Large-scale magnetic fields can explain the baryon asymmetry of the Universe. *Phys. Rev.*, D93(8):083520, 2016.

[135] B. Link. Instability of superfluid flow in the neutron star inner crust. *MNRAS*, 422:1640–1647, May 2012.

[136] Jacques M. Wagstaff, Robi Banerjee, Dominik Schleicher, and Günter Sigl. Magnetic field amplification by the small-scale dynamo in the early universe. *Phys. Rev. D*, 89:103001, May 2014.

[137] Maxim Dvornikov and Victor B. Semikoz. Influence of the turbulent motion on the chiral magnetic effect in the early Universe. 2016.

[138] Mattias Christensson, Mark Hindmarsh, and Axel Brandenburg. Inverse cascade in decaying 3-D magnetohydrodynamic turbulence. *Phys. Rev.*, E64:056405, 2001.

[139] Dieter Biskamp and Wolf-Christian Müller. Decay laws for three-dimensional magnetohydrodynamic turbulence. *Phys. Rev. Lett.*, 83:2195–2198, Sep 1999.

[140] Hess V. F. Über beobachtungen der durchdringenden strahlung bei sieben freiballonfahrten. *Physikalische Zeitschrift*, 13:1084, 1912.

[141] Pierre Auger. Nature of cosmic rays. *Nature*, 135:820–821, 1935.

[142] The Pierre Auger Project Design Report. 1996.

[143] D. J. Bird et al. Detection of a cosmic ray with measured energy well beyond the expected spectral cutoff due to cosmic microwave radiation. *Astrophys. J.*, 441:144–150, 1995.

[144] Pijushpani Bhattacharjee and Günter Sigl. Origin and propagation of extremely high-energy cosmic rays. *Physics Reports*, 327(3–4):109 – 247, 2000.

[145] R. Barkana and A. Loeb. In the beginning: the first sources of light and the reionization of the universe. *Physics Reports*, 349:125–238, July 2001.

[146] S. Zaroubi. The Epoch of Reionization. In T. Wiklind, B. Mobasher, and V. Bromm, editors, *The First Galaxies*, volume 396 of *Astrophysics and Space Science Library*, page 45, 2013.

[147] A. Ferrara and S. Pandolfi. Reionization of the Intergalactic Medium. *ArXiv e-prints*, September 2014.

[148] A. Mesinger, editor. *Understanding the Epoch of Cosmic Reionization*, volume 423 of *Astrophysics and Space Science Library*. 2016.

[149] B. Ciardi and A. Ferrara. The First Cosmic Structures and Their Effects. *Space Sci. Rev.*, 116:625–705, February 2005.

[150] B. B. Nath and P. L. Biermann. Did cosmic rays reionize the intergalactic medium? *Monthly Notes of the RAS*, 265, November 1993.

[151] S. Sazonov and R. Sunyaev. Preheating of the Universe by cosmic rays from primordial supernovae at the beginning of cosmic reionization. *Monthly Notes of the RAS*, 454:3464–3471, December 2015.

[152] Andrei Mesinger and Steven Furlanetto. Efficient Simulations of Early Structure Formation and Reionization. *Astrophys. J.*, 669:663, 2007.

[153] E. Rollinde, E. Vangioni, and K. A. Olive. Population III Generated Cosmic Rays and the Production of ^{6}Li. *ApJ*, 651:658–666, November 2006.

[154] X. Fan, M. A. Strauss, G. T. Richards, J. F. Hennawi, R. H. Becker, R. L. White, A. M. Diamond-Stanic, J. L. Donley, L. Jiang, J. S. Kim, M. Vestergaard, J. E. Young, J. E. Gunn, R. H. Lupton, G. R. Knapp, D. P. Schneider, W. N. Brandt, and N. A. Bahcall. A Survey of z¿5.7 Quasars in the Sloan Digital Sky Survey. IV. Discovery of Seven Additional Quasars. *AJ*, 131:1203–1209, March 2006.

[155] Planck Collaboration, P. A. R. Ade, N. Aghanim, M. Arnaud, M. Ashdown, J. Aumont, C. Baccigalupi, A. J. Banday, R. B. Barreiro, J. G. Bartlett, and et al. Planck 2015 results. XIII. Cosmological parameters. *A&A*, 594:A13, September 2016.

[156] Piero Madau and Francesco Haardt. Cosmic Reionization after Planck: Could Quasars Do It All? *Astrophys. J.*, 813(1):L8, 2015.

[157] B. Ciardi and P. Madau. Probing beyond the Epoch of Hydrogen Reionization with 21 Centimeter Radiation. *ApJ*, 596:1–8, October 2003.

[158] S. R. Furlanetto, S. P. Oh, and F. H. Briggs. Cosmology at low frequencies: The 21 cm transition and the high-redshift Universe. *Phys. Rep.*, 433:181–301, October 2006.

[159] M. F. Morales and J. S. B. Wyithe. Reionization and Cosmology with 21-cm Fluctuations. *ARA&A*, 48:127–171, September 2010.

[160] J. R. Pritchard and A. Loeb. 21 cm cosmology in the 21st century. *Reports on Progress in Physics*, 75(8):086901, August 2012.

[161] B. E. Robertson, R. S. Ellis, J. S. Dunlop, R. J. McLure, and D. P. Stark. Early star-forming galaxies and the reionization of the Universe. *Nature*, 468:49–55, November 2010.

[162] I. T. Iliev, G. Mellema, P. R. Shapiro, and U.-L. Pen. Self-regulated reionization. *MNRAS*, 376:534–548, April 2007.

[163] B. Ciardi, J. S. Bolton, A. Maselli, and L. Graziani. The effect of intergalactic helium on hydrogen reionization: implications for the sources of ionizing photons at $z > 6$. *MNRAS*, 423:558–574, June 2012.

[164] N. Y. Gnedin. Cosmic Reionization on Computers: Numerical and Physical Convergence. *ApJ*, 821:50, April 2016.

[165] G. L. Bryan and M. L. Norman. Statistical Properties of X-Ray Clusters: Analytic and Numerical Comparisons. *ApJ*, 495:80–99, March 1998.

[166] R. Barkana and A. Loeb. Identifying the Reionization Redshift from the Cosmic Star Formation Rate. *ApJ*, 539:20–25, August 2000.

[167] P. Madau, A. Ferrara, and M. J. Rees. Early Metal Enrichment of the Intergalactic Medium by Pregalactic Outflows. *ApJ*, 555:92–105, July 2001.

[168] B. J. Carr, J. R. Bond, and W. D. Arnett. Cosmological consequences of Population III stars. *ApJ*, 277:445–469, February 1984.

[169] Volker Bromm and Richard B. Larson. The First stars. *Ann. Rev. Astron. Astrophys.*, 42:79–118, 2004.

[170] L. Tornatore, A. Ferrara, and R. Schneider. Population III stars: hidden or disappeared? *MNRAS*, 382:945–950, December 2007.

[171] U. Maio, B. Ciardi, K. Dolag, L. Tornatore, and S. Khochfar. The transition from population III to population II-I star formation. *MNRAS*, 407:1003–1015, September 2010.

[172] A. Pallottini, A. Ferrara, S. Gallerani, S. Salvadori, and V. D'Odorico. Simulating cosmic metal enrichment by the first galaxies. *MNRAS*, 440:2498–2518, May 2014.

[173] R. Schneider, A. Ferrara, P. Natarajan, and K. Omukai. First Stars, Very Massive Black Holes, and Metals. *ApJ*, 571:30–39, May 2002.

[174] R. Schneider, K. Omukai, A. K. Inoue, and A. Ferrara. Fragmentation of star-forming clouds enriched with the first dust. *Monthly Notes of the RAS*, 369:1437–1444, July 2006.

[175] T. C. Beers and N. Christlieb. The Discovery and Analysis of Very Metal-Poor Stars in the Galaxy. *ARA&A*, 43:531–580, September 2005.

[176] R. K. Sheth, H. J. Mo, and G. Tormen. Ellipsoidal collapse and an improved model for the number and spatial distribution of dark matter haloes. *Monthly Notes of the RAS*, 323:1–12, May 2001.

[177] P. Madau and M. Dickinson. Cosmic Star-Formation History. *ARA&A*, 52:415–486, August 2014.

[178] T. R. Choudhury and A. Ferrara. Experimental constraints on self-consistent reionization models. *Monthly Notes of the RAS*, 361:577–594, August 2005.

[179] P. Madau. The Intergalactic Medium. *A review for the Encyclopedia of Astronomy and Astrophysics (Institute of Physics Publishing)*, May 2000.

[180] P. Petitjean, J. K. Webb, M. Rauch, R. F. Carswell, and K. Lanzetta. Evidence for structure in the H I column density distribution of QSO absorbers. *Monthly Notes of the RAS*, 262:499–505, May 1993.

[181] M. Schirber and J. S. Bullock. Faint Active Galactic Nuclei and the Ionizing Background. *ApJ*, 584:110–128, February 2003.

[182] J. Miralda-Escudé. On the Evolution of the Ionizing Emissivity of Galaxies and Quasars Required by the Hydrogen Reionization. *ApJ*, 597:66–73, November 2003.

[183] P. Madau, F. Haardt, and M. J. Rees. Radiative Transfer in a Clumpy Universe. III. The Nature of Cosmological Ionizing Sources. *ApJ*, 514:648–659, April 1999.

[184] C.-A. Faucher-Giguère, A. Lidz, L. Hernquist, and M. Zaldarriaga. Evolution of the Intergalactic Opacity: Implications for the Ionizing Background, Cosmic Star Formation, and Quasar Activity. *ApJ*, 688:85–107, November 2008.

[185] A. Mesinger, S. Furlanetto, and R. Cen. 21CMFAST: a fast, seminumerical simulation of the high-redshift 21-cm signal. *Monthly Notes of the RAS*, 411:955–972, February 2011.

[186] K. Finlator, S. P. Oh, F. Özel, and R. Davé. Gas clumping in self-consistent reionization models. *MNRAS*, 427:2464–2479, December 2012.

[187] B. B. Nath and J. Silk. Heating of the intergalactic medium as a result of structure formation. *MNRAS*, 327:L5–L9, October 2001.

[188] J. E. Gunn and B. A. Peterson. On the Density of Neutral Hydrogen in Intergalactic Space. *ApJ*, 142:1633–1641, November 1965.

[189] Robert H. Becker et al. Evidence for reionization at Z 6: Detection of a Gunn-Peterson trough in a Z = 6.28 quasar. *Astron. J.*, 122:2850, 2001.

[190] J. S. Bolton, G. D. Becker, M. G. Haehnelt, and M. Viel. A consistent determination of the temperature of the intergalactic medium at redshift z = 2.4. *Monthly Notes of the RAS*, 438:2499–2507, March 2014.

[191] George D. Becker, James S. Bolton, Martin G. Haehnelt, and Wallace L. W. Sargent. Detection of Extended He II Reionization in the Temperature Evolution of the Intergalactic Medium. *Mon. Not. Roy. Astron. Soc.*, 410:1096, 2011.

[192] Patrick McDonald, Jordi Miralda-Escude, Michael Rauch, Wallace L. W. Sargent, Tom A. Barlow, and Renyue Cen. A measurement of the temperature-density relation in the intergalactic medium using a new Lyman-alpha absorption line fitting method. *Astrophys. J.*, 562:52–75, 2001. [Erratum: Astrophys. J.598,712(2003)].

[193] Massimo Ricotti, Nickolay Y. Gnedin, and J. Michael Shull. The evolution of the effective equation of state of the igm. *Astrophys. J.*, 534:41–56, 2000.

[194] P. Blasi. The origin of galactic cosmic rays. *A&Ar*, 21:70, November 2013.

[195] A. W. Strong, I. V. Moskalenko, and V. S. Ptuskin. Cosmic-Ray Propagation and Interactions in the Galaxy. *Annual Review of Nuclear and Particle Science*, 57:285–327, November 2007.

[196] B. C. Lacki. The ultimate fate of cosmic rays from galaxies and their role in the intergalactic medium. *Monthly Notes of the RAS*, 448:L20–L24, March 2015.

[197] T. Montmerle. On the possible existence of cosmological cosmic rays. I - The framework for light-element and gamma-ray production. *ApJ*, 216:177–191, August 1977.

[198] E. E. Salpeter. The Luminosity Function and Stellar Evolution. *ApJ*, 121:161, January 1955.

[199] R. B. Larson. Early star formation and the evolution of the stellar initial mass function in galaxies. *Monthly Notes of the RAS*, 301:569–581, December 1998.

[200] P. O. Lagage and C. J. Cesarsky. The maximum energy of cosmic rays accelerated by supernova shocks. *A&A*, 125:249–257, September 1983.

[201] M. Jubelgas, V. Springel, T. Enßlin, and C. Pfrommer. Cosmic ray feedback in hydrodynamical simulations of galaxy formation. *A&A*, 481:33–63, April 2008.

[202] E. Rollinde, D. Maurin, E. Vangioni, K. A. Olive, and S. Inoue. Cosmic Ray Production of Beryllium and Boron at High Redshift. *ApJ*, 673:676–685, February 2008.

[203] H. Alfvén. Existence of Electromagnetic-Hydrodynamic Waves. *Nature*, 150:405–406, October 1942.

[204] T. A. Enßlin, C. Pfrommer, V. Springel, and M. Jubelgas. Cosmic ray physics in calculations of cosmological structure formation. *A&A*, 473:41–57, October 2007.

[205] R. J. Gould. The stopping power of atomic matter for relativistic ions, mesons, electrons and positrons. *Physica*, 62:555–564, December 1972.

[206] C. Evoli, M. Valdés, A. Ferrara, and N. Yoshida. Energy deposition by weakly interacting massive particles: a comprehensive study. *Monthly Notes of the RAS*, 422:420–433, May 2012.

[207] C. Evoli, S. Salvadori, and A. Ferrara. The puzzling origin of the ^{6}Li plateau. *MNRAS*, 390:L14–L18, October 2008.

[208] S. Gabici, F. A. Aharonian, and P. Blasi. Gamma rays from molecular clouds. *Ap&SS*, 309:365–371, June 2007.

[209] W. H. Press, S. A. Teukolsky, W. T. Vetterling, and B. P. Flannery. *Numerical recipes in FORTRAN. The art of scientific computing.* 1992.

[210] J. Jasche, B. Ciardi, and T. A. Enßlin. Cosmic rays and the primordial gas. *MNRAS*, 380:417–429, September 2007.

[211] L. Spitzer, Jr. and E. H. Scott. Heating of H i Regions by Energetic Particles. II. Interaction Between Secondaries and Thermal Electrons. *ApJ*, 158:161, October 1969.

[212] X. Fan, C. L. Carilli, and B. Keating. Observational Constraints on Cosmic Reionization. *ARA&A*, 44:415–462, September 2006.

[213] A. Mesinger, A. Ferrara, and D. S. Spiegel. Signatures of X-rays in the early Universe. *Monthly Notes of the RAS*, 431:621–637, May 2013.

[214] M. Ricotti and J. P. Ostriker. X-ray pre-ionization powered by accretion on the first black holes - I. A model for the WMAP polarization measurement. *Monthly Notes of the RAS*, 352:547–562, August 2004.

[215] M. McQuinn. Constraints on X-ray emissions from the reionization era. *MNRAS*, 426:1349–1360, October 2012.

[216] J. R. Pritchard and S. R. Furlanetto. 21-cm fluctuations from inhomogeneous X-ray heating before reionization. *Monthly Notes of the RAS*, 376:1680–1694, April 2007.

[217] P. Chang, A. E. Broderick, and C. Pfrommer. The Cosmological Impact of Luminous TeV Blazars. II. Rewriting the Thermal History of the Intergalactic Medium. *ApJ*, 752:23, June 2012.

[218] D Bohm. The characteristics of electrical discharges in magnetic fields a. guthrie, rk wakerling, 77–86, 1949.

[219] Lyman Spitzer Jr. Particle diffusion across a magnetic field. *The Physics of Fluids*, 3(4):659–661, 1960.

[220] Peter Schneider. *Extragalactic astronomy and cosmology: an introduction.* Springer, 2014.

[221] Pasquale Blasi, Elena Amato, and Marta D'Angelo. High-Energy Cosmic Ray Self-Confinement Close to Extra-Galactic Sources. *Phys. Rev. Lett.*, 115(12):121101, 2015.

[222] C. Evoli, A. Mesinger, and A. Ferrara. Unveiling the nature of dark matter with high redshift 21 cm line experiments. *JCAP*, 11:024, November 2014.

[223] J. H. Oort. The force exerted by the stellar system in the direction perpendicular to the galactic plane and some related problems. *Bulletin of the Astronomical Institutes of the Netherlands*, 6:249, August 1932.

[224] F. Zwicky. Die Rotverschiebung von extragalaktischen Nebeln. *Helvetica Physica Acta*, 6:110–127, 1933.

[225] V. C. Rubin, W. K. Ford, Jr., and N. Thonnard. Rotational properties of 21 SC galaxies with a large range of luminosities and radii, from NGC 4605 /R = 4kpc/ to UGC 2885 /R = 122 kpc/. *Ap. J.*, 238:471–487, June 1980.

[226] Maxim Markevitch. Chandra observation of the most interesting cluster in the universe. 2005. [ESA Spec. Publ.604,723(2006)].

[227] G. Hinshaw, D. Larson, E. Komatsu, D. N. Spergel, C. L. Bennett, J. Dunkley, M. R. Nolta, M. Halpern, R. S. Hill, N. Odegard, L. Page, K. M. Smith, J. L. Weiland, B. Gold, N. Jarosik, A. Kogut, M. Limon, S. S. Meyer, G. S. Tucker, E. Wollack, and E. L. Wright. Nine-year Wilkinson Microwave Anisotropy Probe (WMAP) Observations: Cosmological Parameter Results. *Ap. J. Suppl.*, 208:19, October 2013.

[228] Gerard Jungman, Marc Kamionkowski, and Kim Griest. Supersymmetric dark matter. *Phys. Rept.*, 267:195–373, 1996.

[229] Michael Klasen, Martin Pohl, and Günter Sigl. Indirect and direct search for dark matter. *Prog. Part. Nucl. Phys.*, 85:1–32, 2015.

[230] Joerg Jaeckel and Andreas Ringwald. The Low-Energy Frontier of Particle Physics. *Ann. Rev. Nucl. Part. Sci.*, 60:405–437, 2010.

[231] R. D. Peccei and Helen R. Quinn. CP. *Phys. Rev. Lett.*, 38:1440–1443, Jun 1977.

[232] Andreas Ringwald. Exploring the Role of Axions and Other WISPs in the Dark Universe. *Phys. Dark Univ.*, 1:116–135, 2012.

[233] Rouven Essig et al. Working Group Report: New Light Weakly Coupled Particles. In *Proceedings, Community Summer Study 2013: Snowmass on the Mississippi (CSS2013): Minneapolis, MN, USA, July 29-August 6, 2013*, 2013.

[234] J. L. Feng, H. Tu, and H.-B. Yu. Thermal relics in hidden sectors. *JCAP*, 10:043, October 2008.

[235] L. Ackerman, M. R. Buckley, S. M. Carroll, and M. Kamionkowski. Dark matter and dark radiation. *Phys. Rev. D*, 79(2):023519, January 2009.

[236] R. Adhikari et al. A White Paper on keV Sterile Neutrino Dark Matter. *JCAP*, 1701(01):025, 2017.

[237] E. Armengaud et al. Final results of the EDELWEISS-II WIMP search using a 4-kg array of cryogenic germanium detectors with interleaved electrodes. *Phys. Lett.*, B702:329–335, 2011.

[238] E. Armengaud et al. Axion searches with the EDELWEISS-II experiment. *JCAP*, 1311:067, 2013.

[239] G. *et al* Angloher. Results from 730 kg days of the CRESST-II Dark Matter search. *European Physical Journal C*, 72:1971, April 2012.

[240] C. E. Aalseth, P. S. Barbeau, N. S. Bowden, B. Cabrera-Palmer, J. Colaresi, J. I. Collar, S. Dazeley, P. de Lurgio, J. E. Fast, N. Fields, C. H. Greenberg, T. W. Hossbach, M. E. Keillor, J. D. Kephart, M. G. Marino, H. S. Miley, M. L. Miller, J. L. Orrell, D. C. Radford, D. Reyna, O. Tench, T. D. Van Wechel, J. F. Wilkerson, and K. M. Yocum. Results from a search for light-mass dark matter with a p-type point contact germanium detector. *Phys. Rev. Lett.*, 106:131301, Mar 2011.

[241] E. *et al* Aprile. Dark matter results from 225 live days of xenon100 data. *Phys. Rev. Lett.*, 109:181301, Nov 2012.

[242] R. *et al* (CDMS Collaboration) Agnese. Silicon detector dark matter results from the final exposure of cdms ii. *Phys. Rev. Lett.*, 111:251301, Dec 2013.

[243] R. Bernabei, P. Belli, F. Cappella, V. Caracciolo, S. Castellano, R. Cerulli, C. J. Dai, A. d'Angelo, S. d'Angelo, A. Di Marco, H. L. He, A. Incicchitti, H. H. Kuang, X. H. Ma, F. Montecchia, D. Prosperi, X. D. Sheng, R. G. Wang, and Z. P. Ye. Final model independent result of dama/libra–phase1. *The European Physical Journal C*, 73(12):2648, 2013.

[244] J. Redondo and A. Ringwald. Light shining through walls. *Contemporary Physics*, 52:211–236, May 2011.

[245] Robin Bähre et al. Any light particle search II —Technical Design Report. *JINST*, 8:T09001, 2013.

[246] Alessandro Mirizzi, Javier Redondo, and Gunter Sigl. Microwave Background Constraints on Mixing of Photons with Hidden Photons. *JCAP*, 0903:026, 2009.

[247] Dieter Horns, Luca Maccione, Alessandro Mirizzi, and Marco Roncadelli. Probing axionlike particles with the ultraviolet photon polarization from active galactic nuclei in radio galaxies. *Phys. Rev. D*, 85:085021, Apr 2012.

[248] Manuel Meyer, Daniele Montanino, and Jan Conrad. On detecting oscillations of gamma rays into axion-like particles in turbulent and coherent magnetic fields. *JCAP*, 1409:003, 2014.

[249] Dieter Horns, Axel Lindner, Andrei Lobanov, and Andreas Ringwald. WISP Dark Matter eXperiment and Prospects for Broadband Dark Matter Searches in the $1\,\mu$eV–10 meV Mass Range. In *Proceedings, 10th Patras Workshop on Axions, WIMPs and WISPs (AXION-WIMP 2014): Geneva, Switzerland, June 29-July 4, 2014*, pages 94–101, 2014.

[250] Jhilik Majumdar, Francesca Calore, and Dieter Horns. Searches for modulation of gamma-ray spectra in the galactic magnetic field as a signature of photon-ALPs mixing. *AIP Conf. Proc.*, 1792(1):060009, 2017.

[251] Tesla E. Jeltema and Stefano Profumo. Searching for Dark Matter with X-ray Observations of Local Dwarf Galaxies. *Astrophys. J.*, 686:1045, 2008.

[252] Shunsaku Horiuchi, Philip J. Humphrey, Jose Onorbe, Kevork N. Abazajian, Manoj Kaplinghat, and Shea Garrison-Kimmel. Sterile neutrino dark matter bounds from galaxies of the Local Group. *Phys. Rev.*, D89(2):025017, 2014.

[253] Carlos A. Arguelles and Joachim Kopp. Sterile neutrinos and indirect dark matter searches in IceCube. *JCAP*, 1207:016, 2012.

[254] S. Adrián-Martínez *et al.* Limits on dark matter annihilation in the sun using the {ANTARES} neutrino telescope. *Physics Letters B*, 759:69 – 74, 2016.

[255] M.G. Aartsen *et al.* (IceCube Collaboration). Improved limits on dark matter annihilation in the sun with the 79-string icecube detector and implications for supersymmetry. *Journal of Cosmology and Astroparticle Physics*, 2016(04):022, 2016.

[256] V. S. Berezinsky, A. V. Gurevich, and K. P. Zybin. Distribution of dark matter in the galaxy and the lower limits for the masses of supersymmetric particles. *Physics Letters B*, 294:221–228, November 1992.

[257] C. Boehm, T. A. Ensslin, and J. Silk. Can Annihilating dark matter be lighter than a few GeVs? *J. Phys.*, G30:279–286, 2004.

[258] Kevork N. Abazajian and Manoj Kaplinghat. Detection of a Gamma-Ray Source in the Galactic Center Consistent with Extended Emission from Dark Matter Annihilation and Concentrated Astrophysical Emission. *Phys. Rev.*, D86:083511, 2012. [Erratum: Phys. Rev.D87,129902(2013)].

[259] Dan Hooper and Tim Linden. On The Origin Of The Gamma Rays From The Galactic Center. *Phys. Rev.*, D84:123005, 2011.

[260] Christoph Weniger. A Tentative Gamma-Ray Line from Dark Matter Annihilation at the Fermi Large Area Telescope. *JCAP*, 1208:007, 2012.

[261] Torsten Bringmann and Christoph Weniger. Gamma Ray Signals from Dark Matter: Concepts, Status and Prospects. *Phys. Dark Univ.*, 1:194–217, 2012.

[262] A. Hektor, M. Raidal, and E. Tempel. Evidence for indirect detection of dark matter from galaxy clusters in fermi γ-ray data. *The Astrophysical Journal Letters*, 762(2):L22, 2013.

[263] Alex Drlica-Wagner, German A. Gomez-Vargas, John W. Hewitt, Tim Linden, and Luigi Tibaldo. Searching for Dark Matter Annihilation in the Smith High-Velocity Cloud. *Astrophys. J.*, 790:24, 2014.

[264] A. *et al.* (H.E.S.S. Collaboration) Abramowski. Constraints on an Annihilation Signal from a Core of Constant Dark Matter Density around the Milky Way Center with H.E.S.S. *Phys. Rev. Lett.*, 114(8):081301, 2015.

[265] Shunsaku Horiuchi, Manoj Kaplinghat, and Anna Kwa. Investigating the Uniformity of the Excess Gamma rays towards the Galactic Center Region. *JCAP*, 1611(11):053, 2016.

[266] Shunsaku Horiuchi, Oscar Macias, Diego Restrepo, Andres Rivera, Oscar Zapata, and Hamish Silverwood. The Fermi-LAT gamma-ray excess at the Galactic Center in the singlet-doublet fermion dark matter model. *JCAP*, 1603(03):048, 2016.

[267] Bridget Bertoni, Dan Hooper, and Tim Linden. Is The Gamma-Ray Source 3FGL J2212.5+0703 A Dark Matter Subhalo? *JCAP*, 1605(05):049, 2016.

[268] M. Ackermann et al. Searching for Dark Matter Annihilation from Milky Way Dwarf Spheroidal Galaxies with Six Years of Fermi Large Area Telescope Data. *Phys. Rev. Lett.*, 115(23):231301, 2015.

[269] M. L. Ahnen et al. Limits to dark matter annihilation cross-section from a combined analysis of MAGIC and Fermi-LAT observations of dwarf satellite galaxies. *JCAP*, 1602(02):039, 2016.

[270] A. Albert, others (DES, and Fermi-LAT Collaboration). Searching for Dark Matter Annihilation in Recently Discovered Milky Way Satellites with Fermi-LAT. *Astrophys. J.*, 834(2):110, 2017.

[271] Marco Regis and Piero Ullio. Multi-wavelength signals of dark matter annihilations at the Galactic center. *Phys. Rev.*, D78:043505, 2008.

[272] Lars Bergstrom, Gianfranco Bertone, Torsten Bringmann, Joakim Edsjo, and Marco Taoso. Gamma-ray and Radio Constraints of High Positron Rate Dark Matter Models Annihilating into New Light Particles. *Phys. Rev.*, D79:081303, 2009.

[273] R. M. Crocker, N. F. Bell, C. Balazs, and D. I. Jones. Radio and gamma-ray constraints on dark matter annihilation in the Galactic center. *Phys. Rev.*, D81:063516, 2010.

[274] Masaki Asano, Torsten Bringmann, Günter Sigl, and Martin Vollmann. 130 GeV gamma-ray line and generic dark matter model building constraints from continuum gamma rays, radio, and antiproton data. *Phys. Rev.*, D87(10):103509, 2013.

[275] Torsten Bringmann, Martin Vollmann, and Christoph Weniger. Updated cosmic-ray and radio constraints on light dark matter: Implications for the GeV gamma-ray excess at the Galactic center. *Phys. Rev.*, D90(12):123001, 2014.

[276] Ilias Cholis, Dan Hooper, and Tim Linden. A Critical Reevaluation of Radio Constraints on Annihilating Dark Matter. *Phys. Rev.*, D91(8):083507, 2015. [Phys. Rev.D91,083507(2015)].

[277] V. Berezinsky, A. Bottino, and G. Mignola. High-energy gamma radiation from the galactic center due to neutralino annihilation. *Phys. Lett.*, B325:136–142, 1994.

[278] Paolo Gondolo. Either neutralino dark matter or cuspy dark halos. *Phys. Lett.*, B494:181–186, 2000.

[279] G. Bertone, G. Sigl, and J. Silk. Astrophysical limits on massive dark matter. *Mon. Not. Roy. Astron. Soc.*, 326:799–804, 2001.

[280] Roberto Aloisio, Pasquale Blasi, and Angela V. Olinto. Neutralino annihilation at the Galactic Center revisited. *JCAP*, 0405:007, 2004.

[281] Dan Hooper. Constraining Supersymmetric Dark Matter With Synchrotron Measurements. *Phys. Rev.*, D77:123523, 2008.

[282] Gianfranco Bertone, Guenter Sigl, and Joseph Silk. Annihilation radiation from a dark matter spike at the galactic center. *Mon. Not. Roy. Astron. Soc.*, 337:98, 2002.

[283] Tim Linden, Dan Hooper, and Farhad Yusef-Zadeh. Dark Matter and Synchrotron Emission from Galactic Center Radio Filaments. *Astrophys. J.*, 741:95, 2011.

[284] Ranjan Laha, Kenny Chun Yu Ng, Basudeb Dasgupta, and Shunsaku Horiuchi. Galactic center radio constraints on gamma-ray lines from dark matter annihilation. *Phys. Rev.*, D87(4):043516, 2013.

[285] Gianfranco Bertone, Marco Cirelli, Alessandro Strumia, and Marco Taoso. Gamma-ray and radio tests of the e+e- excess from DM annihilations. *JCAP*, 0903:009, 2009.

[286] Craig Tyler. Particle dark matter constraints from the Draco Dwarf galaxy. *Phys. Rev.*, D66:023509, 2002.

[287] Aravind Natarajan, Jeffrey B. Peterson, Tabitha C. Voytek, Kristine Spekkens, Brian Mason, James Aguirre, and Beth Willman. Bounds on Dark Matter Properties from Radio Observations of Ursa Major II using the Green Bank Telescope. *Phys. Rev.*, D88:083535, 2013.

[288] Marco Regis, Sergio Colafrancesco, Stefano Profumo, W. J. G. de Blok, M. Massardi, and Laura Richter. Local Group dSph radio survey with ATCA (III): Constraints on Particle Dark Matter. *JCAP*, 1410(10):016, 2014.

[289] Aravind Natarajan, James E. Aguirre, Kristine Spekkens, and Brian S. Mason. Green Bank Telescope Constraints on Dark Matter Annihilation in Segue I. 2015.

[290] Le Zhang and Gunther Sigl. Dark Matter Signatures in the Anisotropic Radio Sky. *JCAP*, 0809:027, 2008.

[291] Enrico Borriello, Alessandro Cuoco, and Gennaro Miele. Radio constraints on dark matter annihilation in the galactic halo and its substructures. *Phys. Rev.*, D79:023518, 2009.

[292] G. P. Smith. A peculiar feature at $l^{II} = 40^\circ.5$, $b^{II} = - 15^\circ.0$. *Bulletin of the Astronomical Institutes of the Netherlands*, 17:203, March 1963.

[293] F. R. Elder, R. V. Langmuir, and H. C. Pollock. Radiation from electrons accelerated in a synchrotron. *Phys. Rev.*, 74:52–56, Jul 1948.

[294] C. G. T. Haslam, C. J. Salter, H. Stoffel, and W. E. Wilson. A 408 MHz all-sky continuum survey. II - The atlas of contour maps. *A&A Supp.*, 47:1, January 1982.

[295] M. S. Longair. *High energy astrophysics. Vol.1: Particles, photons and their detection.* March 1992.

[296] G. Ghisellini, P. W. Guilbert, and R. Svensson. The synchrotron boiler. *Astrophys. J.*, 334:L5–L8, November 1988.

[297] Sergio Colafrancesco, S. Profumo, and P. Ullio. Multi-frequency analysis of neutralino dark matter annihilations in the Coma cluster. *Astron. Astrophys.*, 455:21, 2006.

[298] F. J. Lockman, R. A. Benjamin, A. J. Heroux, and G. I. Langston. The Smith Cloud: A High-Velocity Cloud Colliding with the Milky Way. *ApJ*, 679:L21, May 2008.

[299] B. P. Wakker and H. v. Woerden. *High-Velocity Clouds*, page 587. 2013.

[300] Katie M. Chynoweth, Glen I. Langston, and Kelly Holley-Bockelmann. HI Clouds in the M81 Filament as Dark Matter Minihalos–A Phase-Space Mismatch. *Astron. J.*, 141:9, 2011.

[301] David A. Thilker, Robert Braun, Rene A. M. Walterbos, Edvige Corbelli, Felix J. Lockman, Edward M. Murphy, and Ronald Maddalena. On the continuing formation of the andromeda galaxy: detection of hi clouds in the m31 halo. *Astrophys. J.*, 601:L39–L42, 2004.

[302] L. Blitz, D. N. Spergel, P. J. Teuben, D. Hartmann, and W. B. Burton. High-Velocity Clouds: Building Blocks of the Local Group. *ApJ*, 514:818–843, April 1999.

[303] V. Quilis and B. Moore. Where Are the High-Velocity Clouds? *ApJ*, 555:L95–L98, July 2001.

[304] Tobias Westmeier, Christian Bruns, and Jurgen Kerp. Relics of structure formation: extra-planar gas and high-velocity clouds around the Andromeda Galaxy. *Mon. Not. Roy. Astron. Soc.*, 390:1691, 2008.

[305] A. J. Fox, N. Lehner, F. J. Lockman, B. P. Wakker, A. S. Hill, F. Heitsch, D. V. Stark, K. A. Barger, K. R. Sembach, and M. Rahman. On the Metallicity and Origin of the Smith High-velocity Cloud. *ApJL*, 816:L11, January 2016.

[306] Matthew Nichols, Nestor Mirabal, Oscar Agertz, Felix J. Lockman, and Joss Bland-Hawthorn. The Smith Cloud and its dark matter halo: Survival of a Galactic disc passage. *Mon. Not. Roy. Astron. Soc.*, 442(4):2883–2891, 2014.

[307] J. Galyardt and R. L. Shelton. Collisions between Dark Matter Confined High Velocity Clouds and Magnetized Galactic Disks: The Smith Cloud. *ApJ*, 816:L18, January 2016.

[308] A. S. Hill, S. A. Mao, R. A. Benjamin, F. J. Lockman, and N. M. McClure-Griffiths. Magnetized Gas in the Smith High Velocity Cloud. *ApJ*, 777:55, November 2013.

[309] N. M. McClure-Griffiths, G. J. Madsen, B. M. Gaensler, D. McConnell, and D. H. F. M. Schnitzeler. Measurement of a Magnetic Field in a Leading Arm High Velocity Cloud. *Astrophys. J.*, 725:275–281, 2010.

[310] P. Gondolo, J. Edsjo, P. Ullio, L. Bergstrom, Mia Schelke, and E. A. Baltz. DarkSUSY: Computing supersymmetric dark matter properties numerically. *JCAP*, 0407:008, 2004.

[311] G. Bélanger, F. Boudjema, A. Pukhov, and A. Semenov. micrOMEGAs4.1: two dark matter candidates. *Comput. Phys. Commun.*, 192:322–329, 2015.

[312] Marco Cirelli, Gennaro Corcella, Andi Hektor, Gert Hutsi, Mario Kadastik, Paolo Panci, Martti Raidal, Filippo Sala, and Alessandro Strumia. PPPC 4 DM ID: A Poor Particle Physicist Cookbook for Dark Matter Indirect Detection. *JCAP*, 1103:051, 2011. [Erratum: JCAP1210,E01(2012)].

[313] Julio F. Navarro, Carlos S. Frenk, and Simon D. M. White. The Structure of cold dark matter halos. *Astrophys. J.*, 462:563–575, 1996.

[314] J. Einasto. On the Construction of a Composite Model for the Galaxy and on the Determination of the System of Galactic Parameters. *Trudy Astrofizicheskogo Instituta Alma-Ata*, 5:87–100, 1965.

[315] M. Nichols and J. Bland-Hawthorn. The Smith Cloud: High-Velocity Accretion and Dark Matter Confinement. *ApJ*, 707:1642–1649, December 2009.

[316] G. R. Blumenthal and R. J. Gould. Bremsstrahlung, synchrotron radiation, and compton scattering of high-energy electrons traversing dilute gases. *Rev. Mod. Phys.*, 42:237–270, 1970.

[317] Y. Rephaeli. Relativistic electrons in the intracluster space of clusters of galaxies - The hard X-ray spectra and heating of the gas. *Astrophys. J.*, 227:364–369, January 1979.

[318] Craig L. Sarazin. The Energy spectrum of primary cosmic ray electrons in clusters of galaxies and inverse Compton emission. *Astrophys. J.*, 520:529–547, 1999.

[319] S. I. Syrovatskii. The Distribution of Relativistic Electrons in the Galaxy and the Spectrum of Synchrotron Radio Emission. *Soviet Astronomy*, 3:22, February 1959.

[320] Martin Vollmann. *Phenomenology of Dark Matter from Radio to Gamma Ray Frequencies.* PhD thesis, U. Hamburg, Dept. Phys., Hamburg, 2015.

[321] D. Maurin, F. Donato, R. Taillet, and P. Salati. Cosmic rays below z=30 in a diffusion model: new constraints on propagation parameters. *Astrophys. J.*, 555:585–596, 2001.

[322] Marco Cirelli and Marco Taoso. Updated galactic radio constraints on Dark Matter. *JCAP*, 1607(07):041, 2016.

[323] W. Reich. A radio continuum survey of the northern sky at 1420 MHz. I. *A& A*, 48:219–297, May 1982.

[324] R. S. Roger, C. H. Costain, T. L. Landecker, and C. M. Swerdlyk. The radio emission from the Galaxy at 22 MHz. *A& A*, 137:7–19, May 1999.

[325] J. Lavalle, D. Maurin, and A. Putze. Direct constraints on diffusion models from cosmic-ray positron data: Excluding the minimal model for dark matter searches. *Phys. Rev. D*, 90(8):081301, October 2014.

[326] C. Evoli, D. Gaggero, and D. Grasso. Secondary antiprotons as a Galactic Dark Matter probe. *JCAP*, 12:039, December 2015.

[327] M. P. van Haarlem et al. LOFAR: The LOw-Frequency ARray. *Astron. & Astrophys.*, 556:A2, August 2013.

[328] T. L. Wilson, K. Rohlfs, and S. Huttemeister. *Tools of Radio Astronomy, 5th edition.* December 2012.

[329] G. B. Taylor, C. L. Carilli, and R. A. Perley, editors. *Synthesis Imaging in Radio Astronomy II*, volume 180 of *Astronomical Society of the Pacific Conference Series*, 1999.

[330] Alejandro Ibarra, Anna S. Lamperstorfer, and Joseph Silk. Dark matter annihilations and decays after the AMS-02 positron measurements. *Phys. Rev.*, D89(6):063539, 2014.

[331] M. Ackermann et al. Dark matter constraints from observations of 25 Milky Way satellite galaxies with the Fermi Large Area Telescope. *Phys. Rev.*, D89:042001, 2014.

[332] Masahiro Kawasaki, Kazunori Nakayama, and Toyokazu Sekiguchi. CMB Constraint on Dark Matter Annihilation after Planck 2015. *Phys. Lett.*, B756:212–215, 2016.

Eidesstattliche Versicherung

Hiermit erkläre ich an Eides statt, dass ich die vorliegende Dissertationsschrift selbst verfasst und keine anderen als die angegebenen Quellen und Hilfsmittel benutzt habe.

Declaration on oath

I hereby declare, on oath, that I have written the present dissertation by my own and have not used other than the acknowledged resources and aids.

Natacha Leite

Acknowledgements

I want to begin by acknowledging my supervisor, Prof. Günter Sigl, who determined the course of my graduate studies and without whom this work would not be possible. I am thankful for his willingness to take me as a Ph.D. student.

I would like to thank Prof. Robi Banerjee for agreeing to be my co-supervisor.

I wish to thank my collaborators Andrea Ferrara, Benedetta Ciardi, Carmelo Evoli, Claudia Schöneberg, Günter Sigl, Marta d'Angelo, Martin Vollmann, Michel Tytgat, Petar Pavlović and Robin Reuben for their assistance in common projects, for numerous discussions and for their contribution in bringing my understanding of Physics to a different level over these years.

I would also like to acknowledge all the members, including former, of the theoretical Astroparticle group of the II. Institute for Theoretical Physics that I had the chance to meet and learn from during my stay at the University of Hamburg. I want to especially thank Andrey Saveliev for his advices, assistance regarding the bureaucratical sides of being a graduate student and for his valuable help with the translation of the abstract of this work into German.

I have been financially supported by the ”Helmholtz Alliance for Astroparticle Physics (HAP)”, funded by the Initiative and Networking Fund of the Helmholtz Association, and by the Deutsche Forschungsgemeinschaft (DFG) through the Collaborative Research Centre SFB 676 ”Particles, Strings and the Early Universe”.

Carmelo Evoli deserves all my gratitude for the continued dedication, patience and support shown during our work. Additionally, for kindly sharing with me the best plot template ever. I am thankful to the warm hospitality and financial support of the Gran Sasso Science Institute in L'Aquila that provided me with such a great working environment in June 2016.

I am grateful to Mary Violante for having enthusiastically and earnestly proof-read parts of this thesis and to José Francisco Violante for his help in the task.

I am indebted to Prof. Alex Blin for all that he has cheerfully taught me, for believing in me and for constant motivation.

I am grateful to Petar Pavlović, Andrej Dundović, Tanita Jasieniecka and Michi Voth for their friendship and for rescuing me in this journey. I thank my collaborator for a

blossoming comradship and for providing me with the deepest expositions of Physics and Nature that I have had the pleasure to hear. I thank my officemate for patiently bearing even my technical requests and for lighting up the days in the corridor. For lighting up the nights, I thank Chat.

I wish to thank my parents for their very welcomed and unconditional support, understanding and best intentions. My sisters and brothers at the ALP were never closer nor more inspiring than in these three years of physical distance. I thank Coimbra, for I only now begin to realize what you and yours taught me. A thank you to my grandfather who has made me curious to enquire on the nature of the worlds that surround me, without suspecting that I would once attempt to make it my full-time occupation. To Luís I am grateful for what lies beyond phrasing, but that, caring not for words' incompleteness, I express as delighted gratitute towards his existence and unwavering presence.